Tadeusz Kościuszko
Cracow University of Technology
Faculty of Mechanical Engineering
Institute of Applied Mechanics

European Organization
for Nuclear Research
Engineering Department
Mechanical & Materials Engineering

PhD Thesis

Model of discontinuous plastic flow at temperature close to absolute zero

Model nieciągłego płynięcia plastycznego w temperaturze bliskiej zera bezwzględnego

mgr inż. Dawid Jarosław Marcinek

Promoter: prof. dr hab. inż. Błażej Skoczeń

CERN supervisor: dr ès sc. tech. Stefano Sgobba

Cracow 2016

To my wife Barbara and my children
Beniamin, Nikodem, Iga & Tymoteusz

"When we think of failure; Failure will be ours. If we remain undecided; Nothing will ever change. All we need to do is want to achieve something great and then simply to do it. Never think of failure For what we think, will come about."

Maharishi Mahesh Yogi (1918 - 2008)

Preface

I was working on this PhD thesis from 2009 to 2016 associated with the Cracow University of Technology, Poland. Essential experimental part of this work was carried out during my doctoral student contract from February 2011 to January 2014 at the European Organization for Nuclear Research (CERN) in Geneva, Switzerland. My position at CERN was related to materials research for the ITER project, thanks to cooperation with ITER Organization located in Cadarache, France.

I would like to thank the promoter of my thesis, Professor Błażej Skoczeń, for inviting me to this long scientific journey and serve with a possible support for all these years to the very end of it. I am grateful to my CERN supervisor, Stefano Sgobba, for leading me during three years of an intense laboratory work, and later involvement in elaborating the final dissertation. My thanks go to Paul Libeyre of the ITER Organization for creating this great research opportunity, and for friendly cooperation in the course of my contract.

My special gratitude goes to late Arman Nyilas, who influenced in a significant way the experimental part of this work, and who hosted me while my visit to the Karlsruhe Institute of Technology (KIT, Germany) sharing his wide knowledge on material testing in cryogenic environment.

I am grateful to Alexandre Gerardin and Markus Aicheler for everyday support, not only in deeper understanding of many technical and scientifical aspects of my work, but furthermore being there for me in challenge of finding myself in a foreign country. My thanks go to Ana Teresa Perez Fontenla, Ignacio Aviles Santillana, Aline-Marie Piguiet, Jean-Michel Dalin, Michael Guinchard, Jakub Tabin and Rafał Ortwein for many fruitful discussions, on work and life, which made this period of my life much more interesting than expected. I thank Lucia Lain Amador, Valérie Samain and Mateusz Zięba for commitment during their internships, showing me great value of cooperation and a fresh point of view.

Out of work relations, I thank my wife Barbara for support, forbearance and self-sacrifice throughout all these years of ... let's say ... the PhD adventure. I am also grateful to my children for reminding me what is really important in life and showing it in broad range of colors. My thanks go likewise to my mother Jolanta and my father Michał for unceasing efforts of guiding my steps in various paths which I am taking even if seems being out of reach. All my family I thank for miscellaneous aid which, in more or less obvious way, influenced the achievement of the final goal.

Last but not least, I thank my friend Paweł Mazur for keeping me sane when I felt trapped and overwhelmed, who against all odds always helped me to look on the bright side. And to all friends and colleagues, across these years, who helped me in the large frame of the whole picture - Thank You!

Contents

Summary in Polish

Eksploatacja podzespołów i urządzeń pracujących w środowisku kriogenicznym wymaga materiałów, które zachowują wysoką wytrzymałość i plastyczność, a także są odporne na szkodliwe zjawiska zachodzące w niskich temperaturach. Z tego względu konieczne jest prowadzenie badań nad materiałami schłodzonymi niemal do zera bezwzględnego. Przewidywanie zachowania się materiału w tak trudnych warunkach jest istotnym elementem w projektowaniu oraz bezpiecznym konstruowaniu przyrządów i maszyn pracujących w środowisku kriogenicznym.

Do istotnych i najczęściej niepożądanych zjawisk (Rozdział 1), które można zaobserwować w bardzo niskiej temperaturze, zaliczyć należy: nieciągłe płynięcie plastyczne (NPP), przemianę martenzytyczną w stalach austenitycznych oraz ewolucję mikro-uszkodzeń. Te trzy zjawiska dotyczą również austenitycznej stali nierdzewnej 316LN, która jest jednym z powszechnie stosowanych materiałów w kriogenice. Jej użyteczność wiąże się z zachowywaniem wysokiej wydajności w niskich temperaturach dzięki regularnej ściennie centrowanej (RSC) strukturze krystalicznej. Metale i stopy o strukturze RSC są często stosowane w temperaturach bliskich zera bezwzględnego ze względu na unikalne właściwości dotyczące m.in. odkształcenia plastycznego. Szeroka grupa tych materiałów charakteryzuje się niską energią błędu ułożenia co oznacza, że podlegają one zjawisku dynamicznego starzenia odkształceniowego (DSO). Termodynamiczne tło DSO jest silnie związane z zanikaniem ciepła właściwego w przypadku temperatury zmierzającej do zera bezwzględnego. Efekt DSO jest zauważalny jako niestabilność materiałowa w makro-skali poprzez zjawisko NPP. Omawiana niestabilność zaniknie kiedy materiał osiągnie temperaturę T1 (stała materiałowa) charakteryzującą zmianę dominującego ruchu dyslokacji krawędziowych na dominujący ruch dyslokacji śrubowych. Badania eksperymentalne poniżej temperatury T1 są raczej rzadkie ze względu na wysokie koszty i ograniczoną użyteczność najczęściej związaną z fizyką wysokich energii.

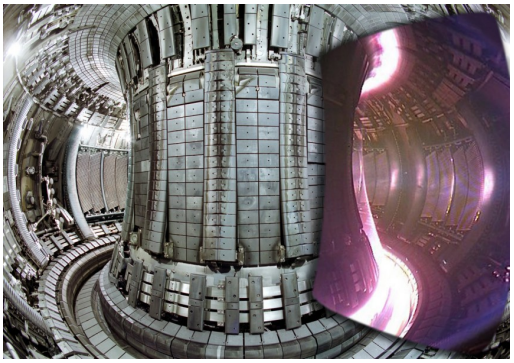

Rysunek 2.2.: Przekrój komory tokamaka JET ze zdjęciem plasmy zrobionym przemysłową kamerą w widzialnym spektrum.

Niniejsza praca rozpoczyna się przedstawieniem obecnego stanu wiedzy (Rozdział 2), na której opierają się przeprowadzone badania. Opis nowoczesnych zastosowań kriogeniki prowadzi do obszaru badań nad fuzją jądrową, gdzie nadprzewodzące magnesy są stosowane w celu wytworzenia pola magnetycznego zdolnego utrzymać gorącą plazmę (Rys. 2.2). Szczególna uwaga jest poświęcona systemowi magnesów i wyznacza zakres bieżących badań. Następnie, przedstawiona jest ogólna definicja zjawiska NPP oraz szczegółowe poglądy na temat jego kinematyki i termodynamiki. Przegląd literatury pozwala zarysować obecny stan wiedzy z naciskiem na analityczne i eksperymentalne badania wspomnianego zjawiska w różnych materiałach: miedzi oraz austenitycznych stalach nierdzewnych 316LN (o niskiej zawartości azotu) i JK2LB (o podwyższonej zawartości manganu).

Głównymi tematami podjętymi w tej pracy są (Rozdział 3):

- Obszerne badania metalurgiczne przeprowadzone na różnych etapach przetwarzania materiału. Oceniany jest wpływ procesów obróbki materiału na mikrostrukturę i własności mechaniczne w temperaturze pokojowej i temperaturze kriogenicznej. Przedstawione są wyniki testów na reprezentatywnych próbkach materiału pobranych z kolejnych kroków procesu wytwarzania płaszcza przewodu zawierającego nadprzewodniki, stosowanego w magnesach Centralnego Solenoidu (CS) w ramach projektu Międzynarodowego Eksperymentalnego Reaktora Termonuklearnego (ang. ITER).

- Wykonanie i interpretacja kriogenicznych testów rozciągania stali stosowanych do elementów magnesów CS. W szczególności, analizowane jest zachowanie materiału w stanie naprężenia z uwzględnieniem zjawiska NPP, a także prędkość propagacji szczeliny zmęczeniowej (ang. FCGR) zbadana na próbkach stali 316LN i JK2LB stosowanych jako płaszcze przewodów systemu CS. Omówiony jest wpływ mikrostruktury na zachowanie tych sto-

pów oraz reakcja na obciążenia quasi-statyczne i cykliczne w temperaturze kriogenicznej, z ukierunkowaniem na model konstytutywny. Wspomniany model jest zorientowany na występowanie efektu DSO (w nierdzewnych stalach austenitycznych) odzwierciedlonego zjawiskiem NPP. Bierze on pod uwagę podłoże termodynamiczne dotyczące mechanizmu transportu ciepła w słabo aktywowanej sieci krystalicznej w niskiej temperaturze. Eksperymentalna część niniejszej pracy została rozszerzona o kriogeniczne testy rozciągania wykonane na stali 316LN dla innych magnesów tokamaka ITER. Dane doświadczalne są usystematyzowane celem głębszego zrozumienia mechanizmu NPP i rozwóju teorii tego zjawiska.

- Stworzenie modelu konstytutywnego NPP i identyfikacja parametrów modelu w temperaturze kriogenicznej. Ponadto, dostarczone są także użyteczne informacje o zjawiskach nisko-temperaturowych, które mogą wspierać wybór materiałów do zastosowań kriogenicznych.

Tematyka niniejszej pracy ma na celu wskazać istotę badań nad niepożądanymi zjawiskami występującymi w niskich temperaturach. Badania te mają służyć przewidywaniu zachowania materiałów i ich wpływu na projektowanie systemów mechanicznych pracujących w środowisku kriogenicznym.

Rozdział 4 zawiera szczegółowe informacje na temat materiałów i zaplecza eksperymentalnego użytego do badań na potrzeby niniejszego opracowania. Zaczyna się opisem badanych materiałów. Skład chemiczny i podstawowe cechy dwóch austenitycznych stali nierdzewnych, 316LN i JK2LB, są podane i porównane. Proces produkcji płaszcza przewodu/nadprzewodnika (typu CICC) dla magnesów ITER CS jest opisany łącznie

Rysunek 4.8.: Zestaw eksperymentalny zamontowany na maszynie wytrzymałościowej UTS.

z cyklem obróbki cieplnej koniecznej dla reakcji wiążącej nadprzewodnik Nb3Sn. Druga część rozdziału daje wgląd do sposobu prowadzenia analiz metalurgicznych wykonanych na próbkach wymienionych materiałów. Opisano narzędzia i techniki stosowane do oceny struktury wewnętrznej. Kolejna część poświęcona jest szczegółowym opisom i ilustracjom zestawu do testów rozciągania w niskiej temperaturze (Rys. 4.8). Kriostat, użyty do badań wytrzymałościowych próbek zanurzonych w ciekłym helu (4,2 K), został pokazany wraz z urządzeniami peryferyjnymi niezbędnymi do precyzyjnego zapisu danych eksperymentalnych. Czujniki umożliwiające pomiar siły, odkształcenia i temperatury wewnątrz kriostatu w czasie trwania testu są również przedstawione. Rozdział zamyka opis badań uzupełniających, testów FCGR, wykonanych na obu omawianych materiałach. Pomiary FCGR i J-test w temperaturze 7 K wnoszą dodatkowe informacje ważne dla zrozumienia zachowania materiałów w niskich temperaturach.

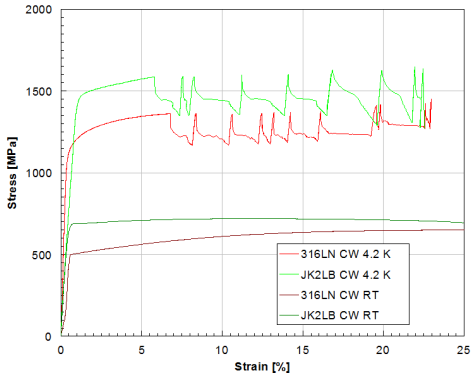

Rysunek 5.14.: Wykres naprężenia względem odkształcenia dla stali 316LN i JK2LB po obróbce na zimno, wyniki dla temperatury pokojowej i kriogenicznej.

Rozdział 5 przedstawia wyniki doświadczalne uzyskane podczas obserwacji metalurgicznych, testów wytrzymałościowych oraz pomiarów FCGR i J-test dla stali 316LN i JK2LB na kolejnych etapach procesu produkcyjnego. Wyniki metalurgiczne zostały przedstawone z podziałem na cztery grupy: pomiar zawartości wtrąceń niemetalicznych, walidacja struktury austenitycznej, porównanie wielkości ziaren krystalograficznych oraz zweryfikowanie potencjalnego pojawienia się wytrąceń węglików na granicach ziaren (na skutek obróbki cieplnej). Następnie, przedstawiono wyniki prób rozciągania prowadzonych w temperaturze pokojowej i ciekłego helu (Rys. 5.14). Nacisk położono na obserwację szczegółów zjawiska NPP i porównania trendu pomiędzy stopami 316LN i JK2LB. Na koniec podano rezultaty testów FCGR wykonanych na obu gatunkach stali, zestawiając je w formie pewnego trendu widniejącego na wykresie łączącym te wyniki z wielkością ziaren i granicami plastyczności badanych materiałów.

Rozdział 6 opisuje model zjawiska NPP wraz z bazującym na nim algorytmem numerycznym. Zawiera on również szczegółowe informacje na temat parametrów służących do ewaluacji krzywych naprężenia w funkcji odkształcenia dla stali 316LN i JK2LB. W pierwszej kolejności przedstawiono kinetykę zjawiska, pokazując związek z efektem DSO. Zaprezentowano mechanizm powstawania spiętrzeń dyslokacji na przeszkodach typu bariera Lomera-Cottrella (LC). Następnie, pokazano algorytm numeryczny podzielony na kolejne kroki: stan początkowy, odkształcenie sprężyste, odkształcenie plastyczne, skokowy spadek naprężenia i przyrost odkształcenia oraz relaksacja. Ostatecznie, podano parametry stosowane w opisanym algorytmie (dla stopów 316LN i JK2LB), na podstawie literatury i danych doświadczalnych.

Rozdział 7 przedstawia wyniki numeryczne uzyskane dzięki implementacji modelu konstytutywnego w oprogramowaniu Maple[1]. Symulacje zostały przygotowane dla stali 316LN i JK2LB badanych w temperaturze 4,2 K, na etapie produkcji po obróbce na zimno (przed obróbką cieplną). Jako pierwsze zademonstrowano krzywe symulacji prób rozciągania z uwzględnieniem szczegółów zjawiska NPP (Rys. 7.5). Ponadto, przedstawiono oddzielne wykresy dla naprężeń stycznych, gęstości dyslokacji i liczby barier LC w sieci krystalicznej materiału. Pokazano również rzuty szczegółowe części wykresów, reprezentujące przebiegi dla pojedynczego wystąpienia analizowanego zjawiska. Wyniki przedstawiono w dwóch grupach, według typu stali: 316LN i JK2LB. Podsumowując, porównanie wyników między badaniami laboratoryjnymi a odpowiednimi symulacjami numerycznymi jest wprowadzeniem do ogólnej dyskusji na końcu Rozprawy.

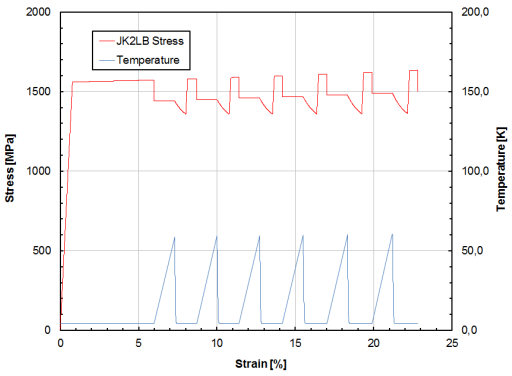

Rysunek 7.5.: Symulacja naprężenia względem odkształcenia w temperaturze kriogenicznej dla stali JK2LB po obróbce na zimno.

[1]Maple to oprogramowanie do obliczeń algebraicznych wydane i sprzedawane przez firmę Maplesoft z siedzibą w Waterloo, Ontario, Canada

W rozdziale 8 omówiono wyniki badań eksperymentalnych i numerycznych ze szczególnym uwzględnieniem zjawiska NPP. Dyskusję podzielono na trzy kolejne podrozdziały. Na wstępie, zarysowano aspekt termo-mechaniczny zjawiska NPP z różnych punktów widzenia, począwszy od czasu jego odkrycia aż do czasu badań prowadzonych dla celów niniejszej pracy. Następnie, opisano wgląd w naturę ewolucji mikrostruktury dla zjawiska NPP. Ostatecznie, zakończono omówieniem koncepcji modelu numerycznego.

Podsumowując niniejszą pracę, trzy podstawowe pytania zostały podniesione:

- Czy - biorąc pod uwagę wykonane badania metalurgiczne - wpływ właściwości mechanicznych i mikrostruktury na zjawisko NPP został wystarczająco rozpoznany?

- Czy - podążając tropem testów wytrzymałościowych w temperaturach kriogenicznych - można usystematyzować wszystkie dostępne dane eksperymentalne dla lepszego zrozumienia mechanizmu NPP i jego tła termodynamicznego dotyczącego transportu ciepła w niskich temperaturach?

- Czy - w odniesieniu do modelu konstytutywnego oraz identyfikacji parametrów - przedstawione rozwiązanie jest reprezentatywne i uniwersalne dla stali nierdzewnych w temperaturach kriogenicznych?

Odpowiedź na wszystkie powyższe pytania brzmi "tak". Wnioski te mają istotne znaczenie dla cienkościennych konstrukcji pracujących w ekstremalnie niskich temperaturach, takich jak wymienniki ciepła czy komory próżniowe. Oznacza to, że deformacja materiału w okolicy zera bezwzględnego może prowadzić do silnego obniżenia spójności sieci krystalicznej ze względu na nieciągły charakter płynięcia plastycznego. Często powtarzające się poślizgi makroskopowe mogą prowadzić do rozwoju pól mikro-uszkodzeń i inicjowania makro-pęknięć, psując integralność struktury. Ponadto, oscylacje temperatury mogą istotnie wpływać na warunki wymiany ciepła oraz - w przypadku nadprzewodników - prowadzić do nieoczekiwanego przejścia ze stanu nadprzewodzenia do normalnego oporu elektrycznego.

Nomenclature

Acronyms

ASTM	American Society for Testing and Materials
BCC	Bottom Correction Coil
CC	Correctional Coils
CCFE	Culham Centre for Fusion Energy
CERN	European Organization for Nuclear Research
CICC	Cable-In-Conduit Conductor
CO	Compaction
COIL	Chemical Oxygen Iodine Lasers
CS	Central Solenoid
CT	Computer Tomography
CW	Cold Work
DEMO	DEMOnstration Power Plant
DPF	Discontinuous Plastic Flow
DSA	Dynamic Strain Aging
ESR	Electroslag Remelting
FCC	Face-Centered-Cubic
FCGR	Fatigue Crack Growth Rate

FEM	Finite Element Method
HEP	High Energy Physics
HSFE	High Stacking Fault Energy
HT	Heat Treatment (Aging)
ICF	Inertial Confinement Fusion
IFMIF	International Fusion Materials Irradiation Facility
IO	ITER Organization
IR	InfraRed
ITER	International Thermonuclear Experimental Reactor
JAEA	Japan Atomic Energy Agency
JET	Joint European Torus
KIT	Karlsruhe Institute of Technology
LC	Lomer-Cottrell
LD	Longitudinal Direction
LHC	Large Hadron Collider
LHD	Large Helical Device
LSFE	Low Stacking Fault Energy
LTSD	Low-Temperature Serrated Deformation
LVDT	Linear Variable Differential Transducer
MRI	Magnetic Resonance Imaging
NIF	National Ignition Facility
NIFS	National Institute for Fusion Science

NSRS	Negative Strain-Rate Sensitivity	
PAUT	Phased Array Ultrasonic Testing	
PF	Poloidal Field	
PLC	Portevin-Le Chatelier	
R&D	Research and Development	
RT	Room Temperature	
RVE	Representative Volume Element	
SA	Solution Annealing	
SCC	Side Correction Coil	
ST	Stretching	
TCC	Top Correction Coil	
TD	Transverse Direction	
TF	Toroidal Field	

Tensorial Notation

β	Scalar	
$\dot{\beta}$	Time derivative	
$\underline{\beta}$	Vector	
$\underline{\underline{\beta}}$	Tensor of 2nd order	

Greek Symbols

α	Coefficient of dislocations stress interaction	$-$
ϵ	Strain	m/m
ϵ^p	Plastic strain	$-$

ϵ^p_{LC}	Plastic strain threshold of massive LC barriers development	$-$
ϵ^s	Strain related to material softening	$-$
η	Conversion factor (in a heat quantity function)	$-$
γ	Amount of crystallographic slip	$-$
Λ	Plastic multiplier	$-$
λ	Mean free path of dislocation	m
λ_i	Mean free path related to a specific type of obstacle	m
μ	Shear modulus	Pa
ν	Poisson ratio	$-$
ρ	Dislocation density	$\frac{1}{m^2}$
ρ_m	Material density	$\frac{kg}{m^3}$
σ	Stress	Pa
σ_p	Stress yield point	Pa
σ_r	Stress level after the catastrophic slip	Pa
σ_T	Characteristic stress in relaxation equation	Pa
σ_∞	Stress level after the transients have died out	Pa
τ	Shear stress	Pa
τ_0	Inner friction shear stress	Pa
τ_e	Shear stress at the dislocation pile-up head	Pa
τ_f	Shear stress due to internal friction	Pa

Latin Symbols

A	Ductility	%

a	Notch (Crack) length	m
B	Dislocation pile-ups density	–
b	Burgers vector length	m
C_1, m_1	Material constants in Paris' law formula	–
C_R	Isotropic hardening moduli	–
C_V	Specific heat	$\frac{J}{kgK}$
C_X	Kinematic hardening moduli	–
d	Mean grain size	m
E	Young's modulus	Pa
E_p	Modulus of linear hardening	Pa
F	Load	N
F_{LC}^{-}	Function of dislocations density	–
f_y	Yield surface	–
F_{LC}^{+}	Function in equation for evolution of LC locks	–
g	Strain gauge factor	–
H	Heaviside function	–
h	Scaling factor	–
H_s	Modulus of linear softening	Pa
J_2	Second invariant of the stress tensor	–
K	Stress intensity factor	Pa
k_a	Dislocation annihilation constant	–
k_i	Coefficients in equation for dislocations evolution	–

L	Strain gauge length	m
l_0	Gauge length	m
M	Taylor factor	–
m	Mass	kg
N	Number of load cycles	–
p	Accumulated plastic strain	–
p_{LC}	Accumulated plastic strain LC limit	–
Q	Heat	J
R	Resistance	Ω
R_H	Isotropic hardening variable	–
Rm	Ultimate tensile strength	Pa
$Rp_{0.2}$	Yield strength	Pa
s	Deviatoric stress	–
T	Temperature	K
t	Time	s
t_T	Characteristic time in relaxation equation	s
t_ϕ	Dimensionless time constant	–
w	Specimen width	m
W^f	Internal friction in the lattice	J
W^p	Plastic work	J
X	Back stress	–
x_{vc}	Coefficient in numerical model	$\frac{1}{m^2}$

1. Introduction

On July 10, 1908, Heike Kamerlingh Onnes for the first time in the history liquefied helium (first helium liquefier shown in Fig. 1.1) by lowering the temperature to 4.2 K [1, 2]. It was critical for discovery of the superconductivity in 1911 [3, 4] and further an open door for many other discoveries in low temperature. Cryogenics subsequently found its place not only in scientific laboratories but more often, towards the XXI century, in medical applications (diagnostic techniques) and industry.

In science, the extensive use of superconductivity phenomenon can be found in magnets of particles accelerators which are operating at temperatures down to 1.9 K. Up to date, the biggest ever built is the Large Hadron Collider (LHC) run by the European Organization for Nuclear Research (CERN) in Geneva [5]. Simultaneously, in the world of fusion research, the most recent assembly of superconducting helical device (stellarator) using this low temperature phenomenon is the Wendelstein 7-X at the Max Planck Institute for Plasma Physics in Greifswald, Germany [6]. At present, the engineering challenge is development and manufacture process of several components designed for construction of International Thermonuclear Experimental Reactor (ITER) - first plasma maintaining tokamak build on such a large scale [7].

The research and development (R&D) process around devices using cryogenics puts a good deal of work in the field of mechanical and materials engineering. Due to the unusual operational environment, materials have to be widely tested to ensure stability in these severe conditions. In the field of physics and mechanics of materials, other phenomena (than above mentioned effect of vanishing electrical conductivity) revealed themselves at cryogenic temperature, most importantly:
- discontinuous plastic flow (DPF),
- $\gamma - \alpha'$ martensitic transformation in stainless steels,
- micro-damage evolution.

Figure 1.1.: First helium liquefier currently stored in Museum Boerhaave.

Constant work in cryogenic environment requires materials which can sustain high strength and maintain ductility as well as resist above mentioned deleterious low temperature phenomena. For this reason it is necessary to study materials cooled to nearly absolute zero. Prediction of behavior in such harsh conditions becomes a vital element in design and safe construction of instruments working with cryogenics.

Three listed above phenomena can be observed in nitrogen strengthened austenitic stainless steel 316LN, which is one of commonly used due to high performance at low temperature related to Face-Centered-Cubic (FCC) structure. In general, metals and alloys of FCC structure are often used due to unique properties including high ductility and toughness down to operation temperatures close to absolute 0. Wide group of these materials (e.g. copper, AISI 304 and 316 families of stainless steels) is characterized by Low Stacking Fault Energy (LSFE) which means that they are subjected to the phenomenon of Dynamic Strain Ageing (DSA) . This phenomenon can be understood as a material instability related to DPF. Thermodynamic background of DSA is strongly related to vanishing specific heat in the case of temperature approaching absolute zero. The DSA effect is noticeable in a macro-scale due to DPF phenomenon. The above material instability disappears when the temperature reaches T_1 (material parameter), which characterizes change from the predominant motion of screw dislocations to the predominant motion of edge dislocations [8]. Research below T_1 is still rare due to high costs and limited applicability, most commonly related to the High Energy Physics (HEP).

2. State of the Art

This chapter introduces the present knowledge and understanding on which the current study is based.

First, the description of different modern cryogenic applications is given. Attention is brought to the area of fusion research where superconducting magnets are commonly used to confine hot plasma. A major project in this field deals with its magnet system and gives the framework of the current study.

Second, general definition of the phenomenon of DPF is depicted. Detailed views on kinematics and thermodynamics of this phenomenon are presented.

Finally, the facts and figures review is drawn across the literature with focus on analytical and experimental study of the phenomenon in different materials: copper, nitrogen strengthened austenitic stainless steel AISI 316LN and high manganese austenitic stainless steel JK2LB.

2.1. Materials for Large Cryogenic Projects

2.1.1. Technological Areas

In the area of cryogenic applications, one can observe continuing technology advances taking place in scientific, industrial, military and space applications. Many sensors and devices like photonic equipment, electro-optic components, high-resolution infrared (IR) sensors as well as microwave and millimeter-wave devices have found their place in space surveillance and reconnaissance, premises security, missile warning, and medical diagnosis and treatment [9]. Also in industrial applications, cryogenics plays a key role in cryogenically cooled turbo-molecular pumps, high-capacity mechanical refrigerators, and high pressure gas coolers.

Many applications in the field of medical diagnostics equipment, such as

magnetic resonance imaging (MRI) and computer tomography (CT) systems capable of providing ultrahigh resolution images, need cryogenics to make them work. In science, the effectiveness of superconducting magnet-based systems, such as accelerators for particle research, rely on cryogenics. Operating at temperatures down to 1.9 K, the biggest accelerator ever built, the Large Hadron Collider (Fig. 2.1), is run by CERN in Geneva at the Swiss-French border. Other emerging applications include high-speed levitation transportation systems, ultra high capacity sonar systems for underwater detection and a chemical oxygen iodine lasers (COIL).

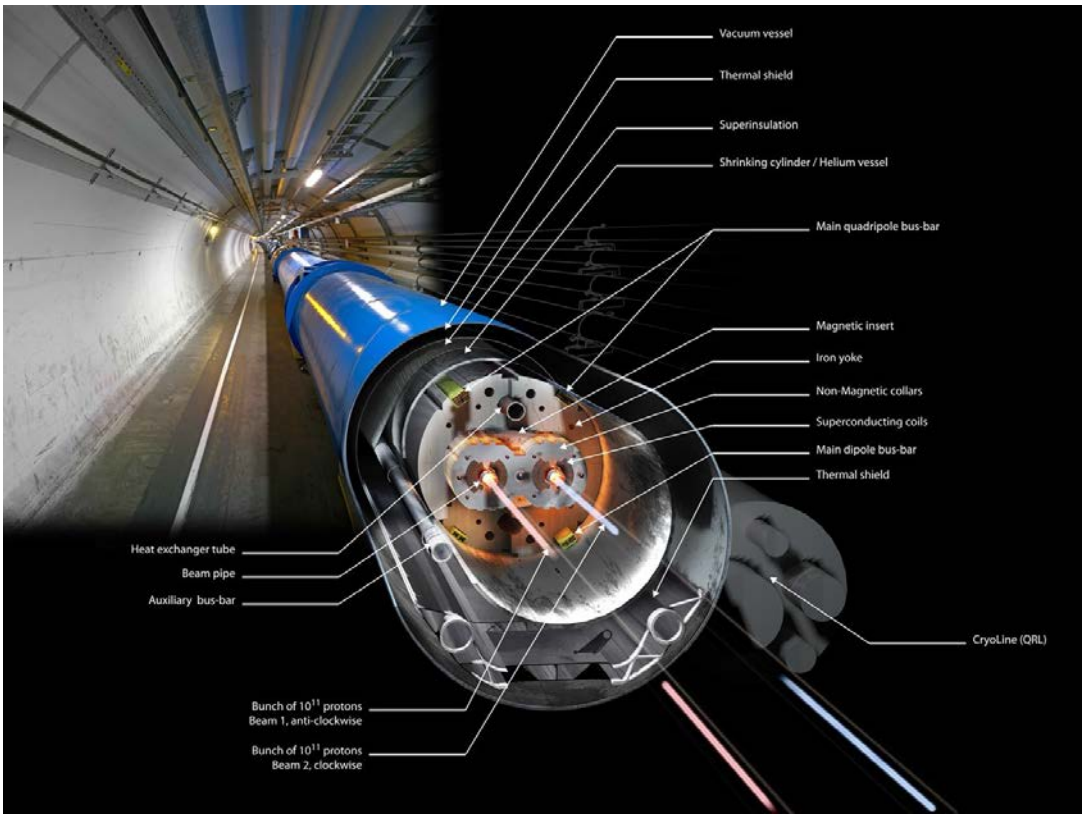

Figure 2.1.: Cross section of the LHC dipole in the tunnel [5].

Reaching high-profile scientific challenges of XXI century, the eyes of many are turned towards fusion energy which is claimed to become a new standard in high efficiency power sources with almost unlimited fuel resources for future

generations. Regardless of technology used, based on tokamak[1] or stellarator [2], these systems are strongly dependent on large scale superconducting magnets. Therefore, a lot of effort is put into R&D in the field of mechanical and materials science to understand and predict behavior of materials that are used in cryogenic systems of laboratory scale reactors or that will potentially be used in cryogenic systems of large scale commercial reactors in the future.

2.1.2. Fusion Reactors

Fusion is a process which powers the Sun by the nuclear processes of joining hydrogen atoms together to form helium [11]. In general, the fusion process - opposite to the fission process taking place in a conventional nuclear plant - is an exothermic reaction between two light atomic nuclei leading to formation of a heavier nucleus. Fusion is not easily achievable due to the repulsive electrostatic forces between the positively charged nuclei. In the proper conditions the electrostatic force between the nuclei is overcome allowing them to fuse together. These conditions take place at extremely high temperatures, when the ions move faster until reaching speed high enough to bring the ions close enough together. The binding energy is responsible for release of a large amount of energy manifested as an increase of temperature.

At present, the leading designs for controlled fusion reaction are based on magnetic or inertial confinement of plasma. The first method uses strong magnetic fields to confine the hot plasma inside a tokamak or a stellarator. The second involves compressing a small pellet containing fusion fuel to extremely high densities using strong lasers or particle beams. Heat from the fusion reactions transfers water into hot steam which powers steam turbines driving electrical generators, similar to the process used in fossil fuel and nuclear fission power stations.

[1] **to**roidal'naya **ka**mera s **ma**gnitnymi **k**atushkami - torus-shaped chamber with magnetic coils, invented in the 1950s by Soviet physicists I. Tamm and A. Sakharov, inspired by an original idea of O. Lavrentiev [10]

[2] **stellarator** - name refers to the possibility of harnessing the power source of the sun, a stellar object, distinct from tokamaks in that they are not azimuthally symmetric, invented by L. Spitzer in 1950 and built the next year in Princeton /USA

The world's largest experiments built up to date are:

- By means of magnetic confinement inside tokamak, the Joint European Torus (JET) at the Culham Centre for Fusion Energy (CCFE) (within EFDA) in Oxfordshire, United Kingdom [12]. In 1997, the JET (Cu-magnet based) produced a peak of 16.1 MW of fusion power, with fusion power of over 10 MW sustained for over 0.5 s (Fig. 2.2). Its successor, the International Thermonuclear Experimental Reactor (ITER), is being constructed in Cadarache, France. The ITER (superconducting-magnet based) is designed to produce ten times more fusion power than the power put into the plasma.

- By means of magnetic confinement inside stellarator, the Large Helical Device (LHD) at the National Institute for Fusion Science (NIFS) in Toki, Japan [13]. The LHD, operational since 1998, has achieved an ion temperature of 13.5 keV and plasma stored energy of 1.44 MJ. Moreover just recently assembled (first plasma produced on 10th December 2015), the Wendelstein 7-X at the Max Planck Institute for Plasma Physics in Greifswald, Germany [6]. With plasma discharges lasting up to 30 minutes, Wendelstein 7-X is to demonstrate the essential stellarator property, namely continuous operation.

- By means of laser-based Inertial Confinement Fusion (ICF), the National Ignition Facility (NIF) at the Lawrence Livermore National Laboratory in Livermore, CA, USA [14]. The NIF reached initial operational status in 2010, the 192-beam laser system fired 1 MJ of laser energy, and has been in the process of increasing the power and energy of its "shots" [15].

Initially, the fusion power was believed to be readily achievable, as fission power had been. However, it has been delayed by several decades due to the extreme requirements for achieving plasma confinement and continuous reactions. In the JET, resistive copper magnets (water cooled) are used to contain the plasma, but as the amount of power which can be obtained is limited, this is not an adequate solution for a large continuously operating reactor [17]. If superconductive magnetic confinement is used then liquid helium cooling of magnet system is required. The challenges related to it are expected to be solved for success of the

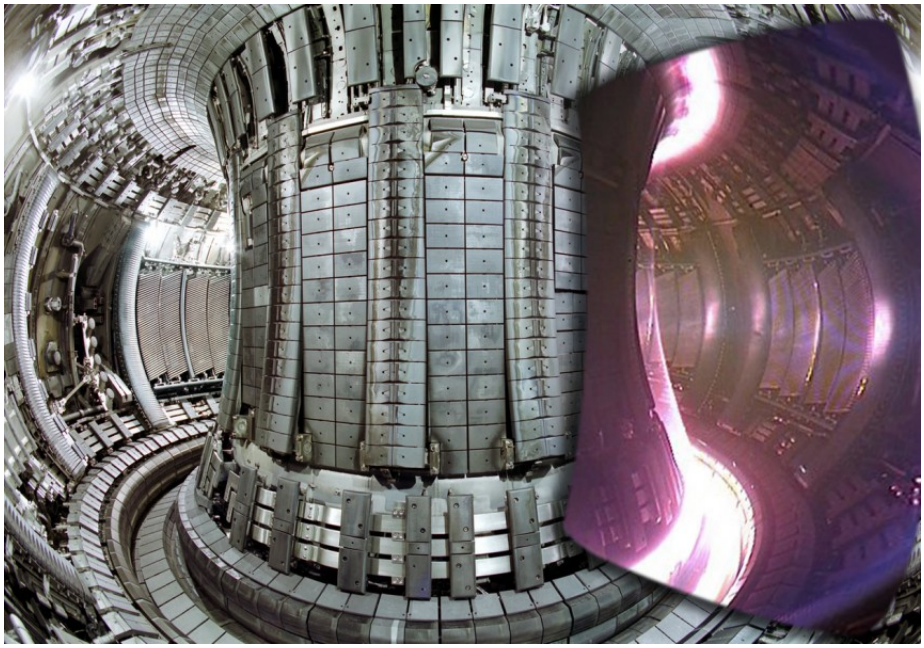

Figure 2.2.: Split image showing interior view of the JET vacuum vessel with a superimposed image of an actual JET plasma, taken with a simple industrial TV camera in the visible spectrum [16].

ITER reactor and, intended to be built upon, the DEMOnstration Power Plant (DEMO) being proposed nuclear fusion power plant. A conceptual design of a DEMO reactor for the first integrated demonstration of fusion power plant is made under the assumption that its design and construction would be started in 2020s and its operation in 2030s [18, 19, 20]. More than 6 decades after the first attempts, commercial fusion power production is still believed to be unlikely before 2050.

The development of materials for fusion reactors has received quite some attention considering the fact that it has been recognized as a problem nearly as important and difficult as that of plasma confinement. The expected flux of neutrons in a fusion reactor will be about 100 times higher then in commercial fission Pressurized Water Reactors. Before the material replacement in the blanket of a fusion reactor, each atom is expected to be displaced about a hundred times due to interactions with neutrons. Additionally, not less important is need for materials which will not result in long-lived radioactive wastes [21]. Finally, frequent cycling mechanical forces and temperature variations between cryogenic and hot plasma will be large.

Following described need of materials development, the International Fusion Materials Irradiation Facility (IFMIF) project has been started and now is in the Engineering Validation and Engineering Design Activities phase [22]. The IFMIF will be a facility to test materials for future fusion reactors by providing an intense source of fusion neutrons.

2.1.3. Large Scale Tokamak

ITER - the International Thermonuclear Experimental Reactor - is a large scale tokamak in which the plasma will be contained in a doughnut-shaped vacuum vessel [7]. Mixture of deuterium and tritium, two isotopes of hydrogen, is to be used as the fuel which is heated to temperature of about 150 million °C then forming a hot plasma. The plasma will be kept away from the walls by magnetic fields produced by superconducting coils. The magnet system comprises the Central Solenoid (CS), Toroidal Field (TF) coils, Poloidal Field (PF) coils and Correction Coils (CC) that magnetically confine, shape and control the plasma inside the torus chamber (Fig. 2.3). The ITER magnets will be cooled with supercritical He at 4 K (-269 °C) in order to operate at the high magnetic fields.

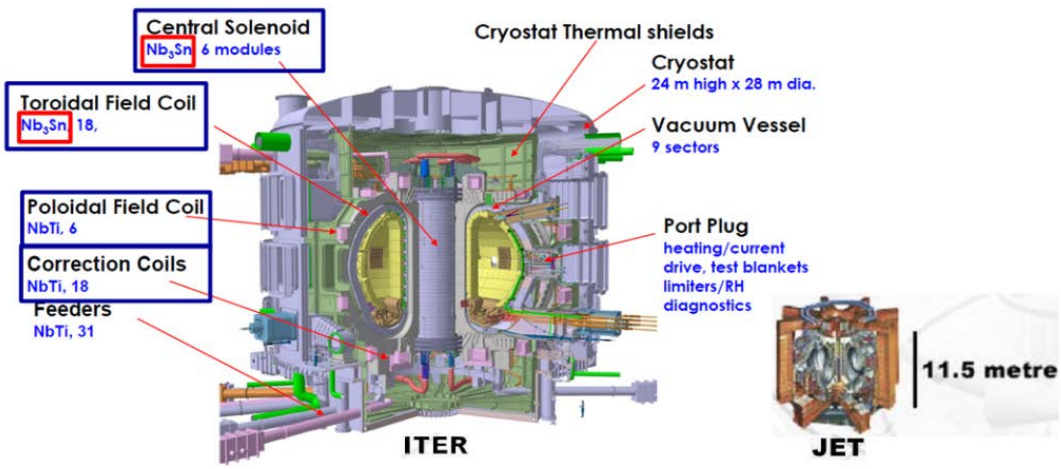

Figure 2.3.: Tokamak ITER (left) with described magnet system and, for comparison by the size, tokamak JET (right, the largest fusion reactor operating up-to-date).

In process of R&D, a lot of materials research and qualification is done within a cooperation agreement between CERN and ITER Organization (IO). Numerous

components of the ITER magnet system and its supporting structure require definition of materials, of production processes and examination techniques. The materials study is based on dedicated campaigns of tests including low temperature tensile tests performed in CERN laboratories. Austenitic stainless steels: very low-carbon 316LN ("ITER grade") and specific high-manganese alloy JK2LB (developed by the Japan Atomic Energy Agency (JAEA) for use as jacket material for the cable-in-conduit of the ITER CS) are extensively used. Participation in defining, conducting and interpreting the results of destructive and non-destructive testing provides a unique opportunity for detailed observation and characterization of the behavior of materials at low temperature, with particular emphasis on the phenomenon of the DPF.

Central Solenoid

The CS is basically a large transformer which drives the main plasma current. It is made of 6 independent coil packs, held together by a vertical precompression structure, that uses a superconducting Nb_3Sn (niobium-tin) Cable-In-Conduit Conductor (CICC). The conduit material has to prove good fatigue behavior and resist the large electromagnetic forces arising during operation. The conductor jacket consists of circle-in-square extruded and drawn austenitic stainless steel pipes [23] which are produced in unit lengths up to 910 m. In the CS a plasma current of 15 MA will be initiated and sustained by stored magnetic energy of 6.4 GJ. Maximum field of 13 T will be reached in the center of the stacked modules.

Toroidal Field

The TF produces a magnetic field, around the doughnut-shaped vessel, which confines the plasma particles. The 18 magnet coils will be able to reach a maximum magnetic field of 11.8 T with a total magnetic energy of 41 GJ. It will be the biggest component of the ITER magnet system (weight of 6540 t in total). The coils will be made of Nb_3Sn superconductors contained in a structural jacket in which a bundle of strands is cabled together and cooled by liquid helium [24]. The strands required for the TF coils have a total length of 80000 km.

Poloidal Field

The PF magnets contribute in maintaining the plasma shape and stability by pinching the plasma away from the walls. Its system consists of 6 horizontal coils (based on NbTi superconductors) positioned outside the TF magnet structure. Due to large size, the actual winding of 4 out of 6 PF coils will take place on the ITER site in a dedicated, 257-meter-long coil winding building. The PF coils are also made of CICC. According to operating requirements, 2 different types of strands will be used, each displaying differences in high-current and low-temperature behavior [25]. The PF coils are designed to produce a total magnetic energy of 4 GJ and a maximum magnetic field of 6 T.

Correction Coils

The CC are developed to reduce the range of magnetic field imperfections in the location and geometry of the other coils [26]. The system consists of 3 sets of 6 coils each, located at the top (TCC), side (SCC) and bottom (BCC) of the tokamak. The CC, much lighter and thinner than the TF and PF coils, are run by a smaller current of 10 kA. The conductor is using a NbTi (niobium-titanium) CICC. The winding-pack is enclosed inside a casing of 20 mm thick stainless steel wall. The CC structural design is driven by the acceptable fatigue stress levels in the conductor jacket, the electrical insulation system and the case material.

2.2. Discontinuous Plastic Flow (DPF)

2.2.1. DPF Description and Occurrence

The stainless steels, used in cryogenic systems are potentially subjected to three main phenomena related to plastic deformation at low temperature [27]: discontinuous plastic flow (serrated yielding), phase transformation and micro-damage evolution. The last two of listed phenomena were presented, with large basis of literature and description of constitutive model, in PhD Theses of Garion [28] and Sitko [29]. The present work is focused on presenting a proper description of an evolving constitutive model of DPF phenomenon.

The DPF represents oscillatory mode of plastic deformation (Fig. 2.4, right)

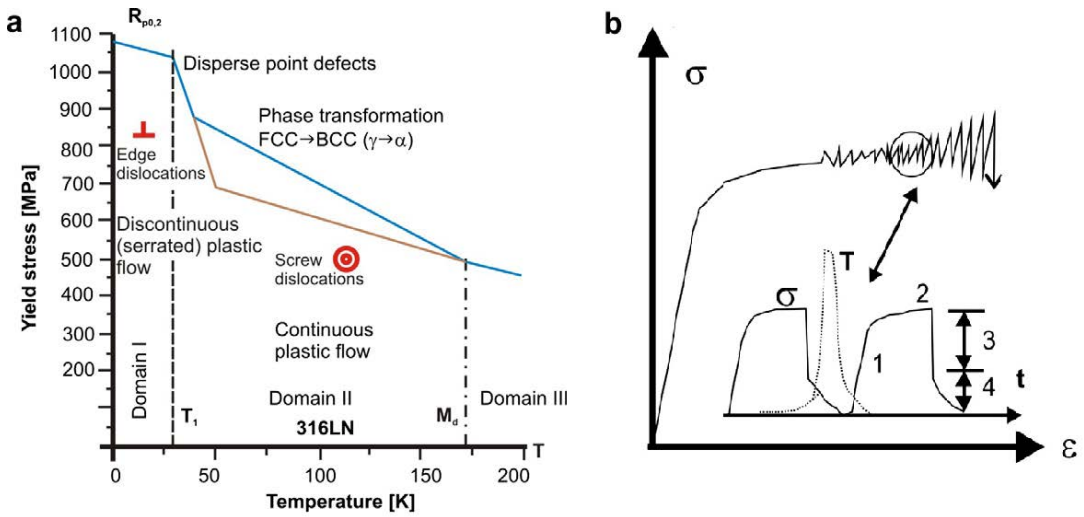

Figure 2.4.: (left) Yield strength (Rp_{02}) as a function of temperature (T), LSFE materials deformed at low temperature (here: 316LN); (right) drawing of the DPF phenomenon underlining 4 phases of the process: elastic (1), plastic flow (2), load drop (3) and relaxation (4). [8]

and shows discontinuous nature of plastic flow at low temperatures (discontinuous considering $d\sigma/d\epsilon$). Apart from strain rate dependance (discussed later), the DPF phenomenon occurs below a certain temperature: T_1 for materials with Low Stacking Fault Energy (LSFE) and T_0 for materials with High Stacking Fault Energy (HSFE). Each of above mentioned temperature thresholds represents change from predominant screw dislocations motion to predominant edge dislocations motion [30]. Seeger [31] pointed out that dislocations character can change due to lack of thermal energy (at very low temperature) necessary to generate and move screw dislocations. Therefore, as the lattice excitation is very low, the predominant motion of edge dislocations is explained by lower driving stress required over the screw dislocations motion. The threshold temperature (T_0 or T_1) is strongly dependent on material, and can reach values as high as 35 K (for austenitic stainless steels). Both these temperatures are identified in the graph of yield strength as a function of temperature (Fig. 2.4, right). Temperature T_1 is shown in Fig. 2.4 (left) for an alloy of LSFE (316LN).

The DPF phenomenon appears to be also strain rate sensitive and occurring only within certain critical values of deformation speed, dependent on examined material [32, 33, 34]. Which means that dislocation motion could be slow enough to avoid accumulation barriers, or so fast to change their predominant character.

The second case is related to generation of heat, due to plastic work within the lattice, which cannot be dissipated quickly enough during fast deformation process.

2.2.2. Kinetics of DPF Phenomenon

The main function reflecting behavior of the lattice related to the DPF phenomenon is the density of dislocation pile-ups B (localized at the Lomer-Cottrell (LC) locks). The Representative Volume Element (RVE) containing dislocation pile-ups is shown on the right side of Fig. 2.5. It is assumed that the dislocation pile-ups density rate $\dot{B}$ (Eq. 2.2) is closely related to accumulated plastic strain rate $\dot{p}$ (the Odqvist parameter):

$$\dot{p} = \sqrt{\frac{2}{3}\underline{\underline{\dot{\epsilon}}}^p : \underline{\underline{\dot{\epsilon}}}^p} \tag{2.1}$$

where $\underline{\underline{\dot{\epsilon}}}^p$ is the plastic strain rate tensor. More barriers in the path of dislocation motion are generated by increasing intensity of plastic flow. Therefore, the following kinetic law of LC locks evolution was postulated [8]:

$$\dot{B} = F^+_{LC}(\rho, T, \underline{\underline{\sigma}})\dot{p}H(p - p_{LC}) \tag{2.2}$$

where: F^+_{LC} is function of dislocations density ρ, temperature T and stress tensor $\underline{\underline{\sigma}}$; then p is accumulated plastic strain and p_{LC} represents a limit above which massive development of the LC locks begins; finally, H stands for the Heaviside function:

$$H(x) = 0 \quad for \quad x < 0 \tag{2.3}$$

$$H(x) = 1 \quad for \quad x \geq 0 \tag{2.4}$$

Assuming small variations of flow stress and isothermal process the following linear representation of LC locks density rate is given:

$$\dot{B} = F^+_{LC}\dot{p} \quad ; \quad p \geq p_{LC} \tag{2.5}$$

The mean shear stress in the lattice τ is composed of inner friction τ_0 and mutual interactions between dislocations [35, 36]:

$$\tau = \tau_0 + \alpha \mu b \sqrt{\rho} \tag{2.6}$$

where: μ is the shear modulus; α stands for a coefficient of dislocations stress interaction; and b represents the length of the Burgers vector. The average shear stress at the head of dislocation pile-ups τ_e (stress concentration point) is equal to:

$$\tau_e = \frac{\pi(1-\nu)}{\mu b} \lambda \tau^2 \tag{2.7}$$

and it is a square function of the mean shear stress in the lattice. Here, ν is the Poisson ratio and λ stands for the mean free path of dislocation which can be interpreted as a distance between a source and a barrier with three different types of obstacles: grain boundaries, dislocations and LC locks:

$$\lambda = \frac{1}{\frac{1}{d} + k_1\sqrt{\rho} + k_2\sqrt{B}} \tag{2.8}$$

where: d denotes mean grain size, and k_1 and k_2 are coefficients. The following criterion of avalanche-like crossing the LC locks was postulated by Skoczen et al. [8]:

$$\begin{cases} \tau \leq \tau_{min} & \Rightarrow \quad B = B_{cr} \\ B \leq B_{min} & \Rightarrow \quad \tau_e = \tau_{cr} \\ \tau > \tau_{min} \wedge B > B_{min} & \Rightarrow \quad \begin{array}{l} (1 - \frac{B_{min}}{B_{cr}})\frac{\tau_e}{\tau_{cr}} + (1 - \frac{\tau_{min}}{\tau_{cr}})\frac{B}{B_{cr}} - \\ -(1 - \frac{B_{min}}{B_{cr}}) - (1 - \frac{\tau_{min}}{\tau_{cr}})\frac{B_{min}}{B_{cr}} = 0 \end{array} \end{cases} \tag{2.9}$$

It is assumed here that there exist maximum (critical) values of B and τ_e above which the DPF phenomenon occurs regardless of the other. In general, the combination of B and τ_e plays a role of DPF trigger, nevertheless, for sufficiently high value of just one, the other becomes negligible for appearance of the phenomenon (Fig. 2.5, left).

It was also assumed that for each loading-unloading cycle (single tooth visible in the stress-strain curve), the parameter B is accumulated starting from 0 up to the point of fulfilling the above-described criterion which triggers the plastic flow instability (drop of load). Finally, making reference to Eq. (2.2), the evolution of parameter B can be described in the following form:

$$dB = F^{+}_{LC}(\rho, T, \underline{\underline{\sigma}})dp \tag{2.10}$$

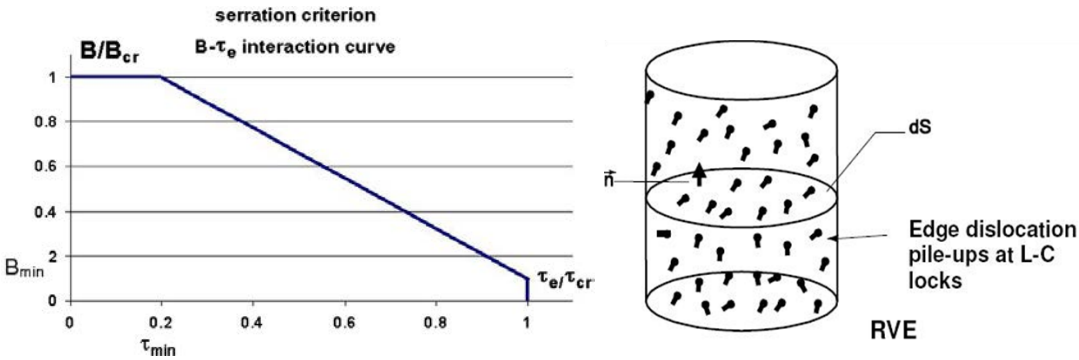

Figure 2.5.: (left) Criterion of massive release of dislocation pile-ups (LC locks) dependent on relation between B and τ_e; (right) RVE containing dislocation groups [8].

2.2.3. Thermodynamic Background

When reaching temperature close to absolute zero, some parameters like thermal conductivity or coefficient of thermal expansion as well as state functions like specific heat (at constant strain) or entropy also tend to zero. This phenomenon causes thermodynamic instability at the temperatures near absolute zero [37] and it has fundamental meaning for the occurrence and triggering of mechanisms of inelastic deformation such as the slip bands.

The heat increment dQ is related to temperature by the following equation:

$$dQ = mC_V dT \tag{2.11}$$

where: m is the mass, C_V represents the specific heat (at constant volume), and T stands for temperature. This equation can be transformed to the following form:

$$\frac{dT}{dQ} = \frac{1}{mC_V} \tag{2.12}$$

Realizing the fact that $C_V \to 0$ when $T \to 0$ (Fig. 2.6), one obtains:

$$\frac{dT}{dQ} \to \infty \tag{2.13}$$

which means that near absolute zero, an arbitrarily small energy dissipation in the lattice will cause significant increase of temperature. Such a dissipation of energy can arise from plastic deformation (dislocations motion in the lattice), which is accompanied by plastic work partially transformed to heat. Thermodynamic instability plays important role for the instability of plastic flow (DPF).

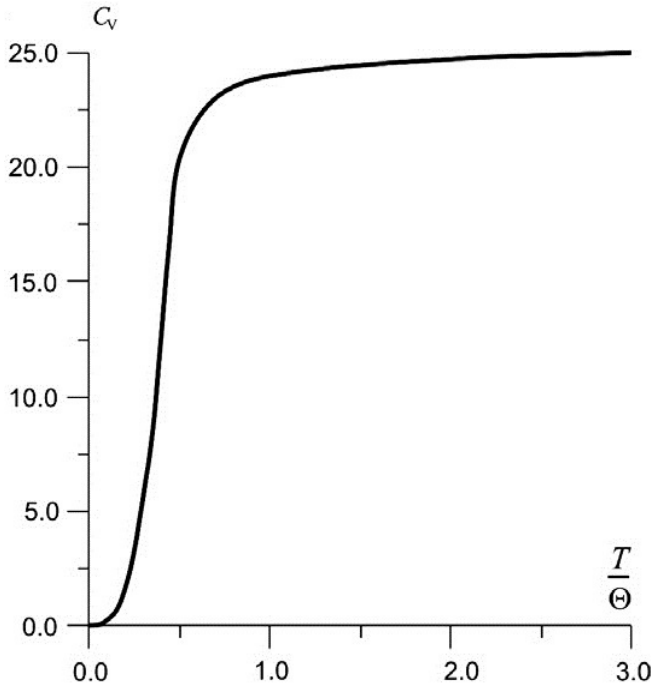

Figure 2.6.: The specific heat (at constant volume) C_V as a function of normalized temperature Θ (Debye reference temperature) [8].

2.3. DPF: Facts and Figures

Plastic deformation of materials and alloys characterized by LSFE (e.g. copper, austenitic stainless steels) at low temperatures (below 20 K - 30 K) occurs in the form of oscillations observed in the stress-strain curve, described as DPF. The DPF appears under special circumstances where deformation is driven by the specific conditions of dislocation dynamics (predominant edge-dislocation motion) with important influence of special thermodynamic conditions (very low thermal conductivity and specific heat) as well as heat exchange rate with the cooling medium. Since the discovery of DPF in the 1950s [31, 38], a large

number of experimental and theoretical works have been performed. Pustovalov [39] attempted to collect as much experimental data as possible, systematize them, determine the main characteristics of DPF (also called Low-Temperature Serrated Deformation, LTSD), examine theoretical hypotheses, compare theory with experiment, and suggest possible mechanisms of DPF in his review.

The phenomenon of DPF was investigated - mainly experimentally, by many authors [40, 41, 42]. Interpretation related to the dislocation motion theory was described by Obst and Nyilas [30, 43]. Wessel [44] as well as Tabachnikova et al. [45] had suggested already before that high stresses at low temperature can result in an avalanche-like propagation of mobile dislocations, but they did not present any model explaining the nature of this instability. Attempting to explain DPF, the authors were referring to the work of Seeger [31], emphasizing that cumulation of dislocations at the inner lattice barriers (like LC locks) results in rise of stress concentration up to the theoretical strength limit. Load drops in the stress-strain graph are related to the catastrophic process taking place during spontaneous generation of dislocations when inner barriers are ruptured. Therefore, plastic flow instability has a mechanical nature. Different point of view was presented by Basiński [38], who attributed load drops to the thermodynamic conditions of the material at low temperature. Another approach to explain DPF was made by Zaiser and Hähner [42] in their work dedicated to oscillatory modes of plastic deformation. The authors were showing similarity between low temperature DPF and Portevin-Le Chatelier (PLC) phenomenon occurring at higher temperatures.

The PLC phenomenon is associated with Dynamic Strain Aging (DSA) [46]. Its occurrence in steel is known to be resulting from diffusion of C and N in the temperature range 150 ^{o}C to 300 ^{o}C [47, 48]. Similar behavior has been observed in Al and Zn alloys related to the diffusion of other elements at higher temperatures. Studies to understand driving mechanisms of the PLC were performed and the constitutive equations for materials with Negative Strain-Rate Sensitivity (NSRS) were suggested [49]. Experimental, theoretical and numerical aspects were furthermore investigated and discussed [50].

The variety of approaches to understand the plastic flow instability, that occurs at low temperatures, underlines complexity of this phenomenon. Many studies and experimental investigations were carried out for different materials,

mainly copper alloys and steels, to compare the results and to find a resemblance between them. Schematic comparison of DPF appearance in different materials is shown in Fig. 2.7

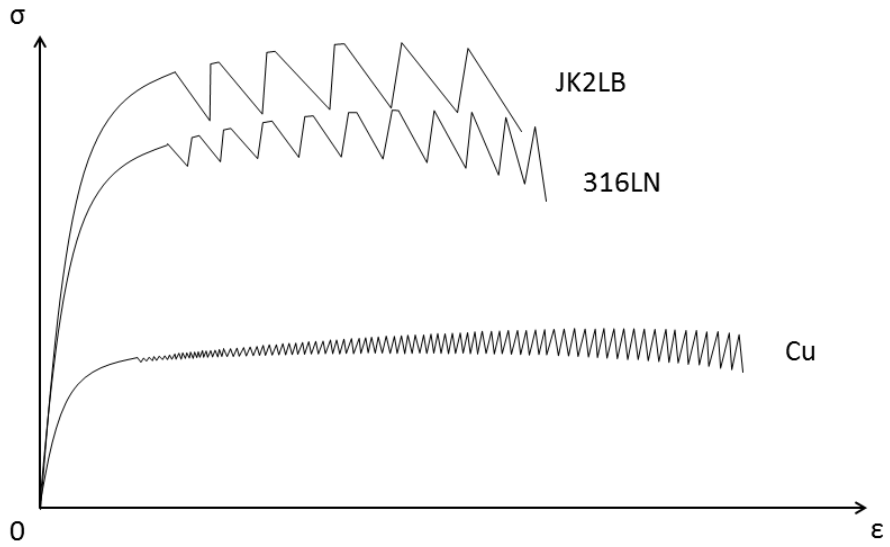

Figure 2.7.: Schematic stress-strain curves, typical of tensile tests at low temperature, showing comparison of DPF appearance in different materials: copper, low carbon austenitic stainless steel 316LN and high manganese austenitic stainless steel JK2LB.

Copper and Copper Alloys

Copper and its alloys belong to the most popular materials for low temperature applications. Contrary to materials which become fragile when cooled down, pure copper immersed in liquid helium proves better mechanical properties including higher ductility as well as higher electrical and thermal conductivity when compared to RT. It was already extensively tested, widely described and reviewed in the past [51]. Due to its broad use in the LHC and former accelerators, copper and its alloys were also investigated at CERN (also examined and described by the author [27]) paying attention among others to DPF phenomenon. Effort spent on detailed experimental assessment and further exploration of obtained data resulted in a description of detailed constitutive model of serrated plastic

flow for copper [8].

Low Carbon Austenitic Stainless Steel 316LN

Low carbon austenitic stainless steel 316LN, in a similar way to copper, became one of the most popular materials for low temperature applications. Despite the fact that it might show lower ductility at cold for grades issued by limited processing and purity, it has this obvious advantage of being a high strength paramagnetic material. The large use of this grade for superconducting magnet structures was accompanied by the collection of extensive data on its mechanical and physical properties [52]. Reviews of 316-type stainless steels contain wide information on behavior of these steels in wrought, cast and welded forms at cryogenic temperature, including inter alia fracture mechanics data, magnetic and elastic properties as well as design-related information [39, 53].

High Manganese Austenitic Stainless Steel JK2LB

High manganese austenitic stainless steel JK2LB was developed by the JAEA for use as the conduit material for the superconducting CICC of the ITER magnets [54, 55]. It is designed to meet the ITER requirements for mechanical properties at cryogenic temperatures: high yield strength, good fracture toughness, good fatigue characteristics. Moreover, it has to avoid sensitization (to keep fulfilling these high demands) after the heat treatment for Nb_3Sn reaction which requires about 650 ^{o}C for about 200 hours. JK2LB mechanical properties at low temperature have been quite extensively assessed [56] but detailed interpretation of appearance of DPF phenomenon in this alloy when subjected to deformation at liquid helium temperature is not yet available.

3. Motivation and Objectives

The ITER CS magnet system will provide the inductive flux variation necessary to drive the plasma as well as it will contribute to the shaping of the field lines and vertical stability control [57]. When energized, the CS coils will experience large pulsed electromagnetic forces which for a 15 MA plasma baseline scenario reaches 479 MPa. It has to be withstood by the conductor jacket including circle-in-square extruded and drawn austenitic stainless steel tubes. This gives a minimum value of $Rp_{0.2}$ equal to 719 MPa for the jacket material at liquid helium temperature [58]. Two austenitic stainless steels were selected as candidates for this jacket: high Manganese grade JK2LB with $Rp_{0.2}$ above 1000 MPa at 4.2 K [59, 60] and fracture toughness K_{IC}(J) above 130 MPa$\sqrt{m}$ following an aging treatment for Nb_3Sn superconductor reaction (650°C during 200 h); and an extra-low carbon ($\leq$ 0.015%) grade 316LN with limited nitrogen content (0.12% - 0.16%) and an additional limit on C + 0.1 N that must be $<$ 0.030%. The stainless steel material was qualified on jackets manufactured from both grades [23, 61].

The main topics handled by the current work are:

- Extensive metallurgical examinations performed at different steps of the material processing, starting from the forged billets, through the extrusion process, to finish with the solution annealed jackets in their final shape. The effect on mechanical and microstructure properties at room temperature (RT) and cryogenic temperatures of processes representative of the manufacturing steps applicable to the jackets (compaction, tensile stretch forming, aging) are also assessed.

- Performing and interpreting cryogenic tensile tests of materials applied for components of ITER CS magnets. In particular, behavior of materials during tension with appearance of DPF phenomenon is analyzed as well as

the Fatigue Crack Growth Rate (FCGR) examined on specimens of 316LN and JK2LB steels machined from CICC conduits of CS system. Microstructure influence on behavior of such alloys at low temperatures is discussed. The materials response due to quasi-static and cyclic loading at cryogenic temperatures is described in the form of dedicated constitutive model. This model is concentrated on the occurrence of the DSA (in austenitic stainless steels), reflected by the DPF phenomenon. The constitutive model takes into account the appropriate thermodynamic background related to heat transport mechanism in the lattice at low temperatures.

The experimental part of the present study is expanded by considerable number of cryogenic tensile tests performed on 316LN austenitic stainless steel for other magnet systems of ITER tokamak. Systematization of all the experimental data was required for advancement in understanding the mechanism of DPF and the development of a theoretical background of this phenomenon.

- Creation of the DPF constitutive model and identification of model parameters at cryogenic temperatures. Moreover, the aim is to deliver useful information concerning low temperature phenomena which could support selection of materials for cryogenic applications.

The present study aims also at assessing the tolerance of undesirable effects at low temperatures and prediction of their influence on design of mechanical systems working at cryogenic temperatures.

4. Experimental

This chapter provides details of material and experimental background necessary for the purpose of the present study.

It starts with description of examined materials. The chemical composition and basic characteristics of two austenitic stainless steels, 316LN and JK2LB, are given and compared. The production process of circle-in-square pipes for ITER CS CICC is described including the superconductor Nb_3Sn reaction cycle with attention paid to the prevention of thermally induced damage of the final produced conductor.

Second section gives insight into metallurgical analyses performed on polished samples of above mentioned materials. Tools and techniques used to assess the inner structures are described.

Following part is dedicated to detailed description and illustration of low temperature tensile test set-up. The cryostat used for tests with specimens immersed in liquid helium are shown together with peripheral equipment necessary for precise data recording during experiment at 4.2 K. The sensors allowing measurement of force, deformation and temperature, inside the cryostat during test, are also presented.

Last section describes supplementary tests, the FCGR and the Fracture Toughness (so called J-test), performed on both candidate materials. The FCGR and the J-test measurements, at the temperatures lower than 7 K, bring additional important information for understanding of the materials behaviour at low temperatures.

4.1. Materials and Characterization

The constitutive model, described in section 2.2, which applies kinetics of the DPF phenomenon, was initially based on results of cryogenic tensile tests per-

formed on copper specimens [27]. Next step towards validation of the postulated model is to confront it with results of tests carried out on other materials. To reach this aim, two austenitic stainless steels, candidate materials for application to ITER CS, were selected: a very low carbon version of alloy AISI 316LN (max. 0.015 % of C) and high-manganese alloy JK2LB (20.5 % ÷ 22.5 % of Mn).

4.1.1. Chemical Composition

Two above mentioned grades were selected for the ITER CS conductor conduit. The 316LN grade with low carbon (L designation) and high nitrogen (N designation) content had main advantage in formation of strong austenite (with respect to ferrite) with increased stability (against martensitic transformation) as well as capability of maintaining high strength and ductility down to cryogenic temperatures [53]. Carbon is limited to avoid, or at least limit, sensitization due to the reaction treatment at 650 ^oC - 200 h. This limitation also enhances corrosion resistance after welding. As far as N is concerned, there are different classes of 316 (L+) N as a function of the minimum yield strength that has to be guaranteed at cold for the different components. The idea of limiting N within the strictly necessary range is to avoid excessive yield strength, hence avoiding that K_{IC} is reduced if this is not strictly necessary [62].

The JK2LB grade on the other hand features high manganese content and addition of a small amount of boron (decreased with respect to previous versions, hence "LB" - Low Boron). It was developed by the JAEA, at the beginning just as JK2, for use in nuclear fusion applications and meet the ITER requirements of high yield strength, favorable fracture behavior and fatigue characteristics at cryogenic temperatures [56, 59].

Specified composition limits of two candidate steels, as well as measured composition of the analyzed materials are given in Table 4.1. Among alloy elements listed in this table some have important influence on steel properties and require particular attention [63]:

- Carbon - gammagenic element, stabilizes austenite during cold deformation; causes formation of the intergranular chromium carbide which decreases resistance to intergranular corrosion.

	Material		Chemical composition (% of mass)									
			C	Cr	Ni	Mo	Mn	Si	P	S	N	Co
Limits	316LN	min		16.0	11.0	2.0					0.12	
		max	<0.015	18.0	14.0	3.0	<2.0	<0.5	<0.035	<0.03	0.16	<0.1
		target	<0.010						<0.015	<0.01		
	JK2LB	min		12.0	8.0	0.5	20.5				0.09	
		max	≤0.030	14.0	10.0	1.5	22.5	≤0.50	≤0.015	≤0.015	0.15	<0.1
		target	<0.025					<0.28	<0.008	<0.008		
Analyzed materials	316LN		0.014	16.60	11.25	2.07	0.96	0.21	0.009	0.002	0.137	0.010
	JK2LB		0.023	12.78	9.19	1.18	21.02	0.25	0.008	0.002	0.150	0.010

Table 4.1.: ITER requirements and chemical composition of analyzed 316LN and JK2LB austenitic stainless steels.

- Chromium - increases the corrosion resistance by creating thin oxide layer which prevents from other types of oxidation; alphagenic element (stabilizes ferrite thus promotes brittle behavior at low temperature).
- Nickel - gammagenic element, extends the area of austenitic ductile behavior, also at low temperature.
- Molybdenum - alphagenic element, increases the corrosion resistance.
- Manganese - contributes to the stabilization of the austenite when its content is below 7 %wt [64].
- Silicon - alphagenic element, improves the cracking resistance of steel at high temperature.
- Nitrogen - gammagenic element, raises the elastic limit without reducing the resistance to intergranular corrosion.

4.1.2. Steelmaking and Processing

The qualification of the stainless steel jackets candidate materials was carried out starting from production process of jackets manufactured in both grades. Steelmaking shown in the left-hand side of Fig. 4.1, included an Electroslag Remelting (ESR) step, where ESR allowed to obtain a limited amount of non-metallic inclusions and an absence of exogenous macro-inclusions [23].

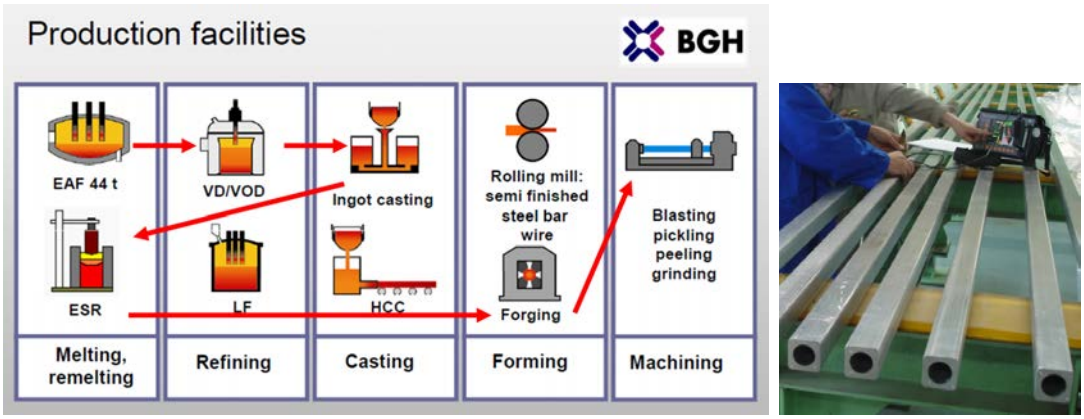

Figure 4.1.: Production process of forged stock for 316LN jackets, applied also to JK2LB (left image, courtesy of BGH [65]). The 316LN extruded circle-in-square CS jacket during ultrasonic testing (right picture).

The steelmaking production process, completed with forging and machining, is followed by extrusion of forged stock. Subsequently, the drawing process of the extruded shape is carried out towards attainment of accurate tolerances, favourable grain structure, improved material properties and good surface finish. Finally, the inspection by Phased Array Ultrasonic Testing (PAUT) of the jacket is performed as for product qualification (Fig. 4.1, right).

4.1.3. Cold Working and Heat Treatment

Further manufacturing steps applicable to the jackets are related to the processing of Nb_3Sn superconducting cable, and have been performed without cable itself but just to simulate the operation, namely:

- Compaction which follows insertion of the cable into the jacket;
- Tensile stretch straining which represents spooling of full length CICC;
- Heat treatment which is necessary for reaction of inserted strands to form Nb_3Sn superconductor.

Influence of compaction and stretching, as mechanical deformation, is not difficult to assess and predict, but limited experience is available w.r.t. the effect of the jacket reaction treatment on a stainless steel. Hence, these effects, combined with the ones of cold deformation, have to be carefully checked experimentally. The precipitation of carbides at grain boundaries in steels causes the intergranular stress corrosion cracking. Austenitic stainless steels, when exposed to the temperature range of about 520 ^{o}C to 800 ^{o}C (sensitizing temperature), become particularly susceptible to depletion of chromium in the grain boundary region. Therefore, considerable efforts were paid in developing stainless steel to withstand this reaction cycle, or at least mitigate its effects: 316LN with extremely low C and controlled N; JK2LB specially designed to avoid sensitization. Nevertheless, one can expect that during the jacket heat treatment cycle, lasting 200 hours in 650 ^{o}C, more or less severe sensitization might occur.

The heat treatment, necessary for investigation of studied grades, was performed using the vacuum furnace located in the CERN laboratory (Fig. 4.2).

The furnace had a cylindrical inner working space of 300 mm in diameter and 590 mm of height, with a pumping unit allowing achievement of vacuum of $7 \cdot 10^{-4}$ Pa.

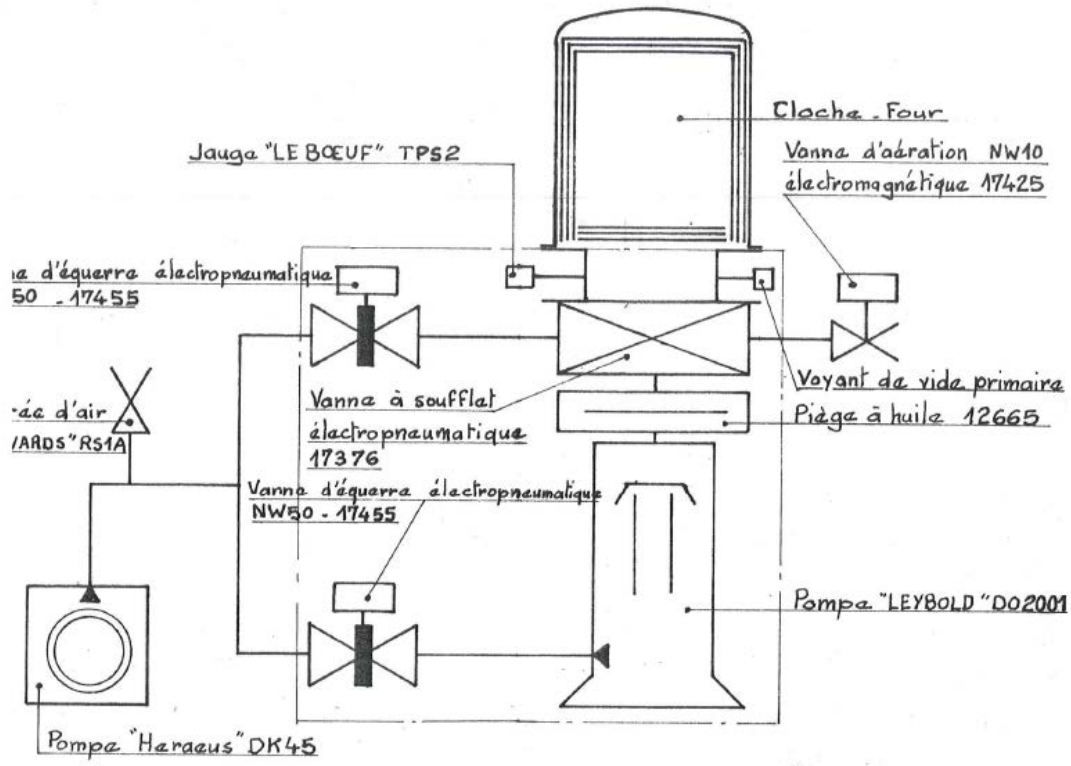

Figure 4.2.: Schematic illustration of the vacuum furnace assembly with a pumping unit circuit [66](historical drawing).

4.2. Metallography

4.2.1. Sample Preparation

The selected materials have been widely analyzed, in terms of metallography, at different intermediate steps of the production process, starting with forged billets before extrusion until the final state after the heat treatment (Fig. 4.3). Samples of 316LN and JK2LB grades have been removed from the processed materials and submitted to destructive metallographical examination. Preparation of such samples was simply based on surface polishing by means of progressive grinding papers and cloths with diamond abrasive compounds.

Figure 4.3.: Piece of JK2LB extruded, compacted and longitudinally strained (2.5%), circle-in-square conduit for superconductive cable with typical samples cut for metallography.

4.2.2. Microscopy

All micro-optical observations were carried out with the use of LEICA DM RME (Quantimet - Q600) reflected light microscope (Fig. 4.4), equipped with multi-lens system allowing fast swap in magnification range from 16x to 1500x. Live image of observed surface was accessible for processing and analyses on the PC though high definition Sony 3-CCD RGB color camera.

Figure 4.4.: LEICA DM RME (Quantimet-Q600) reflected light microscope, equipped with multi-lens system allowing fast swap in magnification range from 16x to 1500x (CERN).

4.2.3. Observation Methods

Observations started with non-metallic inclusion count on as polished surface, following ASTM standard E45-11 [67] method D intended for application to

steel with low inclusion content, giving information on severity level numbers of each inclusion type (A - Sulfide, B - Alumina, C - Silicate and D - Globular Oxide; Fig. 4.5).

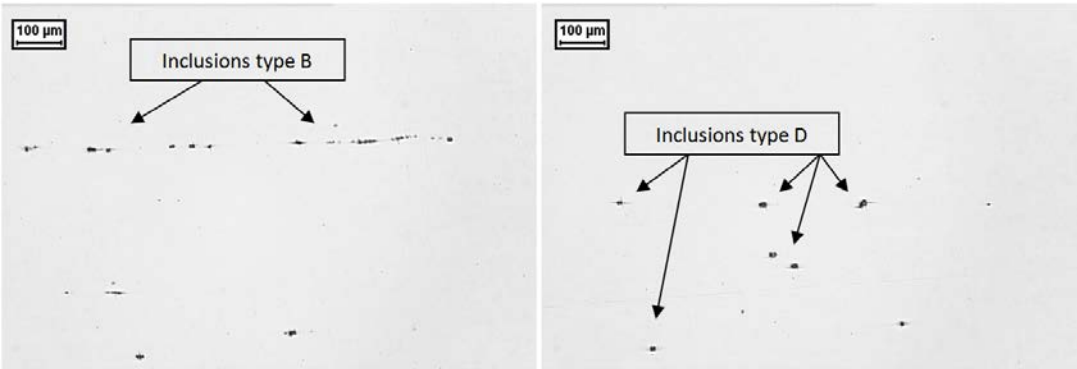

Figure 4.5.: Microscopic images taken during inclusion content measurement showing examples of inclusions B-type (left) and D-type (right).

Next examination step was ferrite content measurement performed after the so-called Murakami etching (ASTM standard E407-07, etchant 98, procedure (b) [68]). After immersion in fresh, hot solution for 5 min, samples surface was examined in search for any yellowish colored points which would indicate the presence of ferrite, thus resulting in rejection of material. Due to ferromagnetic behavior and fragility at low temperature, it was checked for the appearance of even traces of ferrite in the materials applied for the jackets.

Finally, the oxalic acid electrolytic-etching (ASTM standard E407-07, etchant

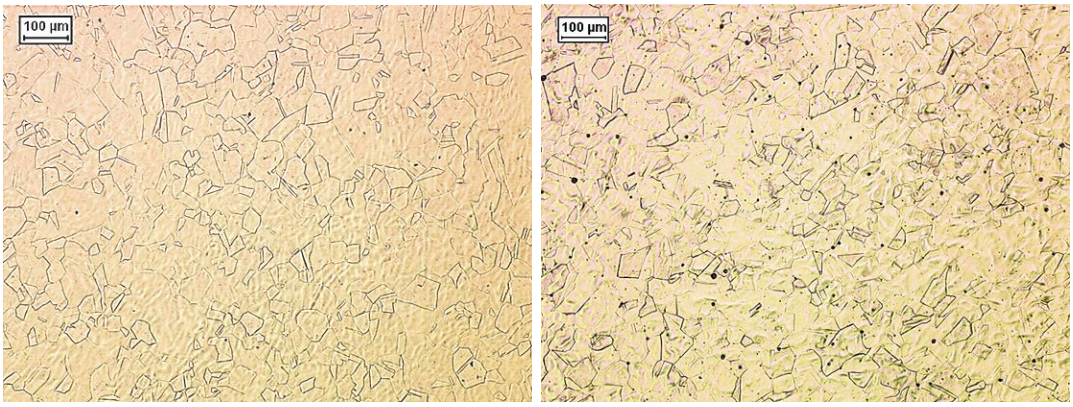

Figure 4.6.: Microstructure of 316LN (left) and JK2LB (right), obtained on samples without heat treatment, by oxalic acid electrolytic-etching used for grain size measurements.

13, procedure (b) [68]) was applied to reveal grain boundaries. Average grain size measurements were carried out (Fig. 4.6), in accordance with ASTM standard E112-12 [69], by linear intercept procedure. Profiting from the fact that the oxalic acid electrolytic-etching is used for classification of etch structure on carbide precipitations within grain boundaries (Fig. 4.7), based on ASTM standard A262-02a(2008) [70], the observation helped to determine level of sensitization arising from heat treatment cycle.

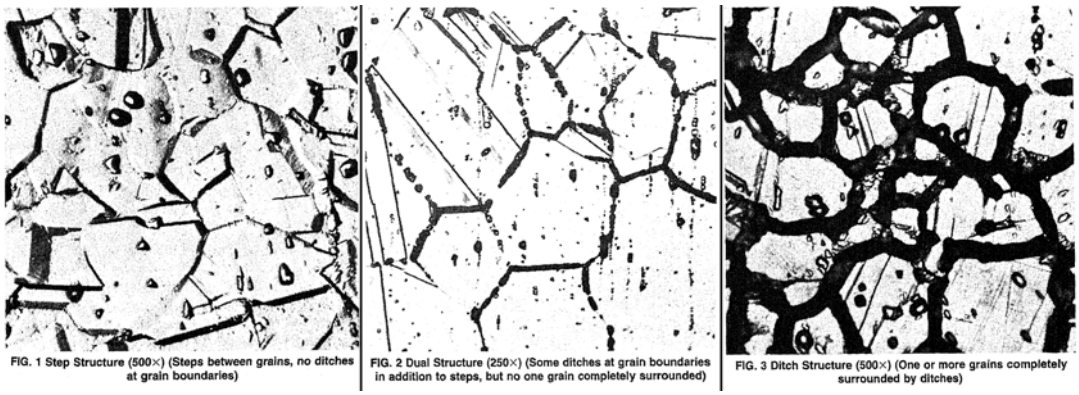

Figure 4.7.: The etch structures classified in Practice A of ASTM standard A262-02a(2008) into the following types: Step Structure (left), Dual Structure (middle) and Ditch Structure (right).

4.3. Tensile Tests

All tensile tests as well as metallurgical observations, described in the present work, have been performed at CERN. Tensile tests have been performed by means of a cryostat which was designed and manufactured at CERN. Experimental setup was placed on the electro-mechanical screw-driven 200 kN UTS tensile machine, equipped with force and displacement sensors (Fig. 4.8). The machine, with precision of 1 μm stroke displacement, was controlled by the connected PC with DIONpro software. The test method was based on ASTM standard E8M-04 [71] for room temperature, and ASTM standard E1450-03 [72] for tests in liquid helium. The scope of both standards is similar, but the content of the second one includes modifications for cryogenic testing, which requires a cryostat and smaller specimens. The standard also addresses concerns for serrated yielding phenomenon, adiabatic heating, and strain-rate effects. Therefore, strain rate

for the low temperature tests was adapted in the range of 10^{-4} s^{-1} and 10^{-3} s^{-1} (compared to the strain rates ranging from 10^{-5} s^{-1} to 10^{-3} s^{-1} generally recommended for tensile tests at 4 K by the above mentioned standard).

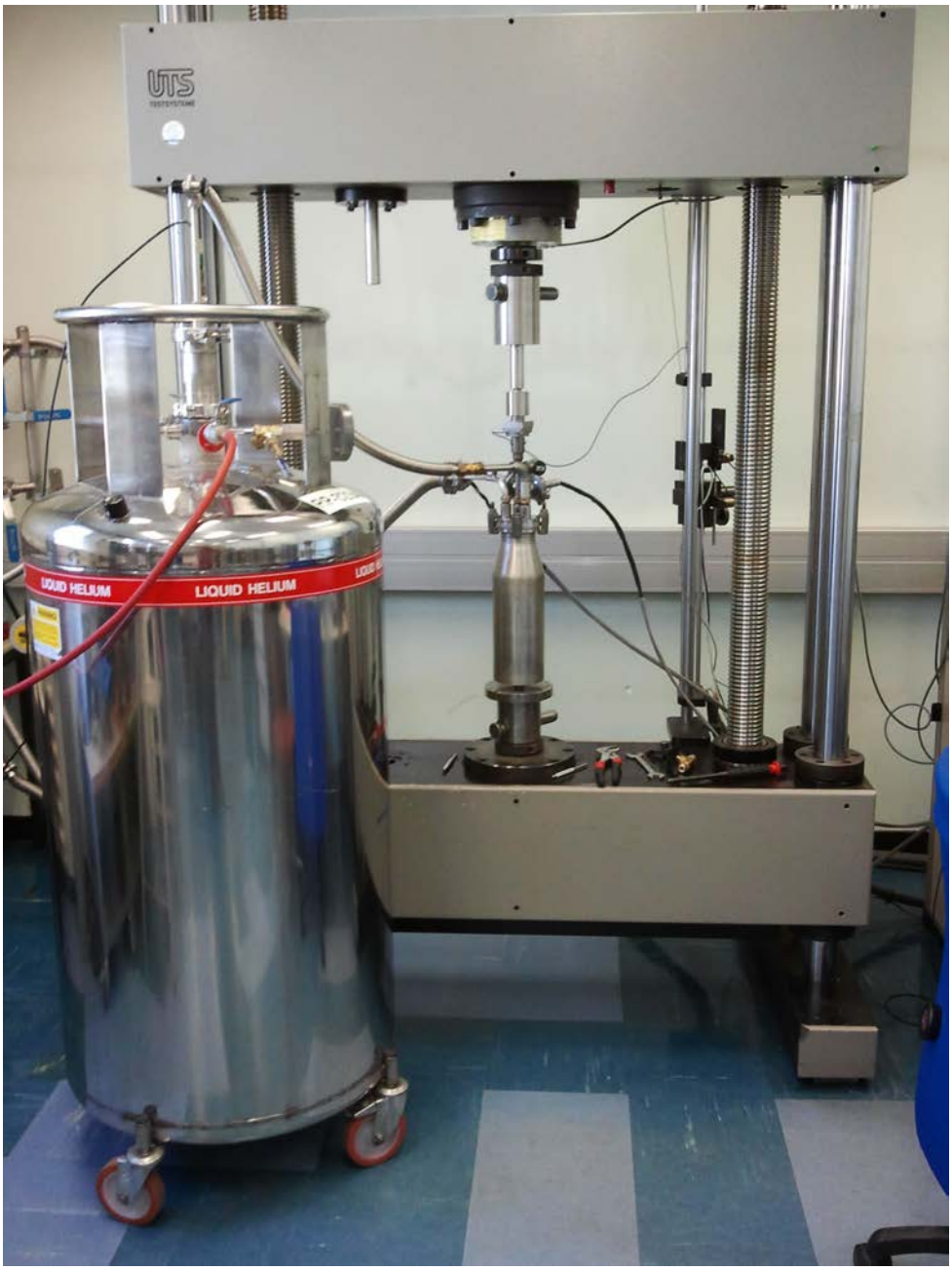

Figure 4.8.: Experimental setup placed on the UTS tensile machine.

The cryostat of 15 kN maximum force, which hosted the tensile specimen of tested material, was externally equipped with helium inlet and outlet as well

as signal connectors with sufficient number of channels for all internal sensors placed on the specimen itself or in close proximity (Fig. 4.9).

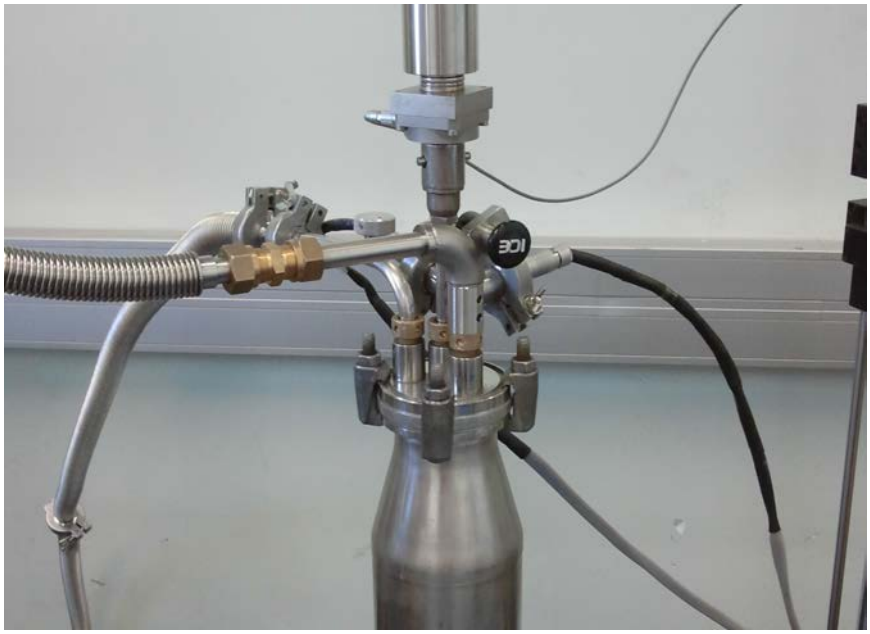

Figure 4.9.: Helium inlet and outlet as well as signal connectors.

4.3.1. Cryostat Structure

The cryostat played an important role to perform tests and obtain the results. The development and experimental validation of this setup have been carried out at CERN [73, 74, 75, 76, 77], before beginning of the present work. The overall view of the cryostat, as used for the test campaign of this PhD work, is presented in Fig. 4.10 and can be described in two parts:

- Dewar, comprising a double partition and a super insulator, responsible for holding and heat insulating liquid helium immersion bath. It has to withstand the loading force of the test due to the fact, that the only fixation to the bottom part of traction machine is at the bottom of the Dewar, which holds the cryostat insert part with a specimen by fixation on top of the Dewar. As the weakest element of supporting structure, it imposes limitation of 15 kN maximum loading force;
- Insert which supports the specimen. It consists of the following main parts: stem of traction, glass fiber columns, element fixing the specimen, mobile

copper screens and the cryostat head. With an aim of reducing the risk of buckling of the glass fiber columns, a stabilizer was fixed on the three columns which reduces the effective length by half. Three mobile copper screens ensure good heat transfer between evaporated gas, the stem of traction and the wall of the tank. They make it possible to decrease the losses by conduction. Electric connections of the sensors and three accesses (the helium supply, the stem of traction and the helium recovery) were combined in the head of the cryostat.

During tensile test, the force on the specimen is transmitted via the needle stem of traction. Described cryostat was designed to work in tension only, therefore, compression tests with its use are not possible. With the capacity of 1.2 l, taking into account losses due to cooling time necessary to reach stable temperature condition inside sealed dewar, the helium consumption for a typical

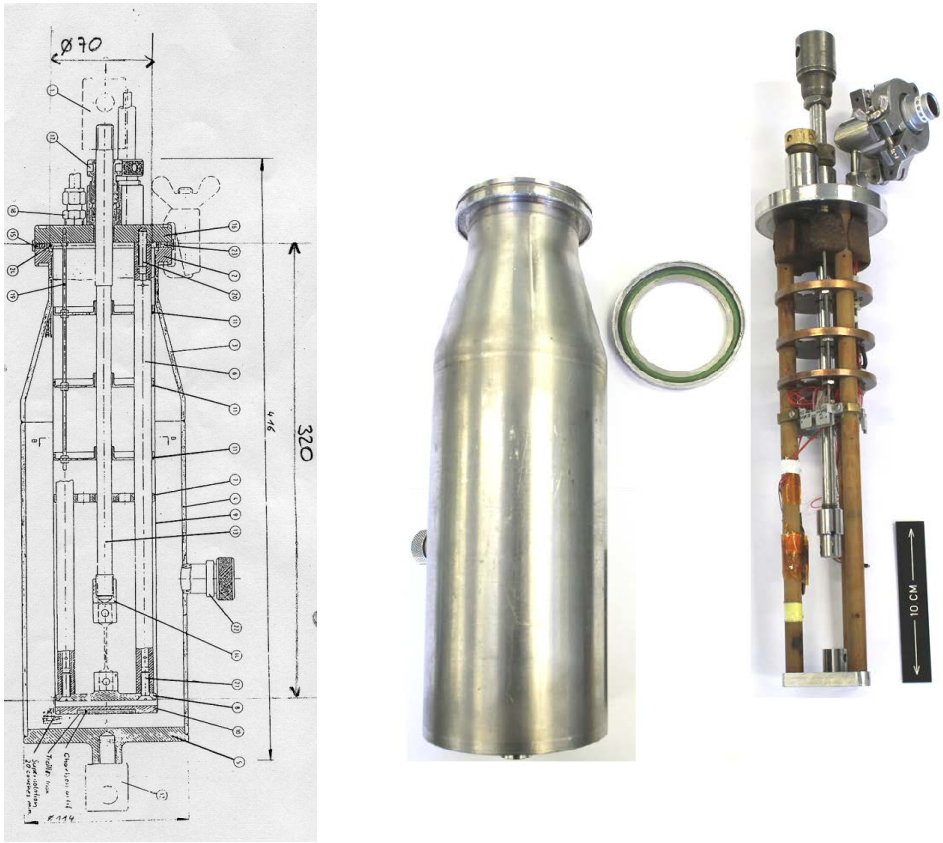

Figure 4.10.: Cryostat assembly (left) with Dewar envelope (middle) and specimen holding insert (right).

half an hour test is approximately 10 l.

4.3.2. Specimen Design

The space inside the cryostat imposes considerable limitations concerning dimensions of test specimen, especially when internal load cell is to be placed inside the cryostat just next to the specimen. Available internal gripping system allows fixation of flat specimens up to 3 mm thickness. The specimen cross-section had to be low enough for reaching the ultimate tensile stress without overtaking the cryostat maximum load limitation. Considering all restrictions, the subsized specimen was designed together with the cryostat, and it was used for tensile tests since then (Fig. 4.11, top). Following studies of standard requirements on dimensions ratio carried out for present work, additional specimen design was suggested optimizing shape in accordance to ASTM standard E8M [71] (Fig. 4.11, bottom). The drawback of new design is that the internal load cell (described in Section 4.3.3 including differences between the internal and external load cell) cannot be used during the test due to specimen's length taking most of limited vertical space inside the cryostat. Therefore, the load measurement

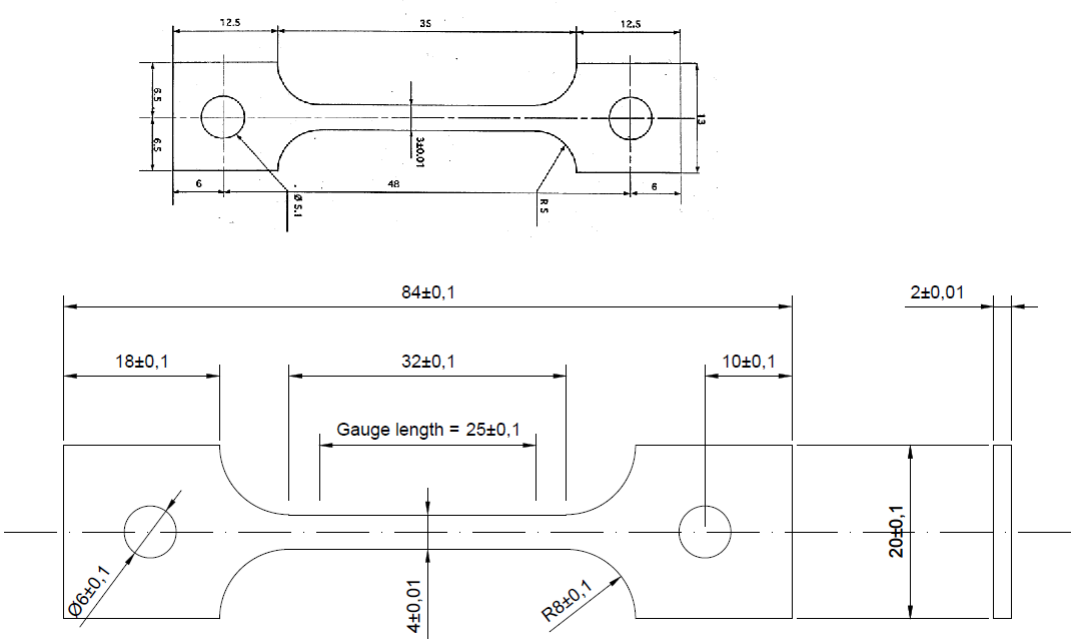

Figure 4.11.: Design of tensile test specimens of "old" first design (top) and "new" standardized design (bottom).

relays entirely on the external load cell. Finally, both specimen designs were kept and used depending on application.

Geometrical dimensions and shape of the tensile test specimens were subjected to careful analysis by Finite Element Method (FEM) to obtain information about optimal gauge length for extensometer placement between the heads of each specimen (Fig. 4.12 and Fig. 4.13). In both cases, one can easily identify concentration of stress (within the analyzed area) which causes higher deformation in this region. Therefore, the maximum gauge length l_0 was set in safe distance from the heads, namely: 2,5 mm from each side of old design specimen ($l_{0_{old-max}} = 20$ mm), and 3,5 mm from each side of new design specimen ($l_{0_{new-max}} = 25$ mm).

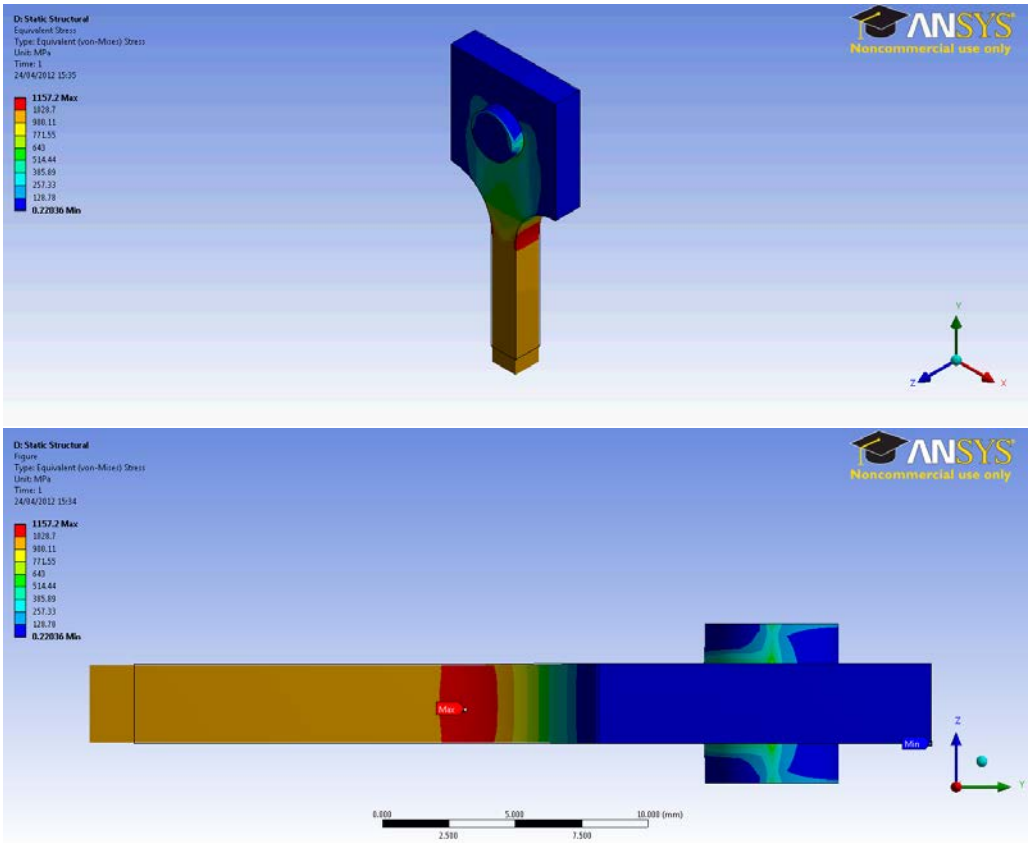

Figure 4.12.: Deformation analysis performed with FEM for subsized tensile test specimens of “old” first design.

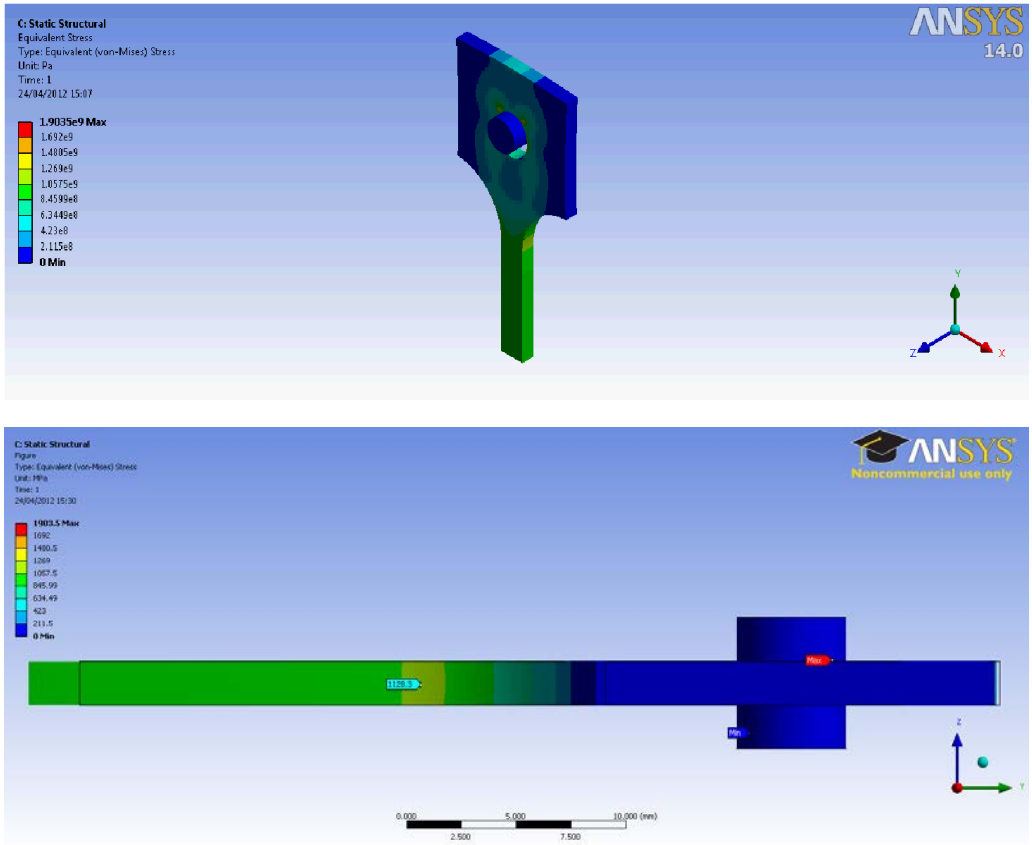

Figure 4.13.: Deformation analysis performed by using FEM for subsized tensile test specimens of "new" standardized design. Maximum stress concentration point has moved to the head of specimen (with respect to "old" design).

4.3.3. Measurement Sensors

The limited available volume inside the cryostat has not only to host the tensile test specimen, but also all necessary measurement sensors [27]. Three main components of measuring system are: the internal load cell placed between the specimen (directly attached to it) and the traction rod, the extensometer fixed at the specimen gauge length, and the temperature sensor stitched to the specimen surface in the middle of gauge length. Mounting the sensor setup with old design specimen within three columns of cryostat insert is presented with two available types of extensometers (described below in Extensometry paragraph): based on LVDT sensors (Fig. 4.14, left), and based on springs with strain gauges (Fig. 4.14, right). The spring type extensometer can be also successfully used with longer gauge length, therefore, it is the one to be used with new design

specimen.

Besides these sensors placed inside the cryostat in direct touch with the specimen, there are additional sensors outside the cryostat providing supplementary information. First, the external force sensor which is connected as a joint between the traction rod of the cryostat and the fixing grip of the tensile test machine. Second, the UTS machine stroke displacement sensor which offers control over displacement speed (applied strain) and boundary limits (ensures safety boundaries against mechanical damage of the cryostat).

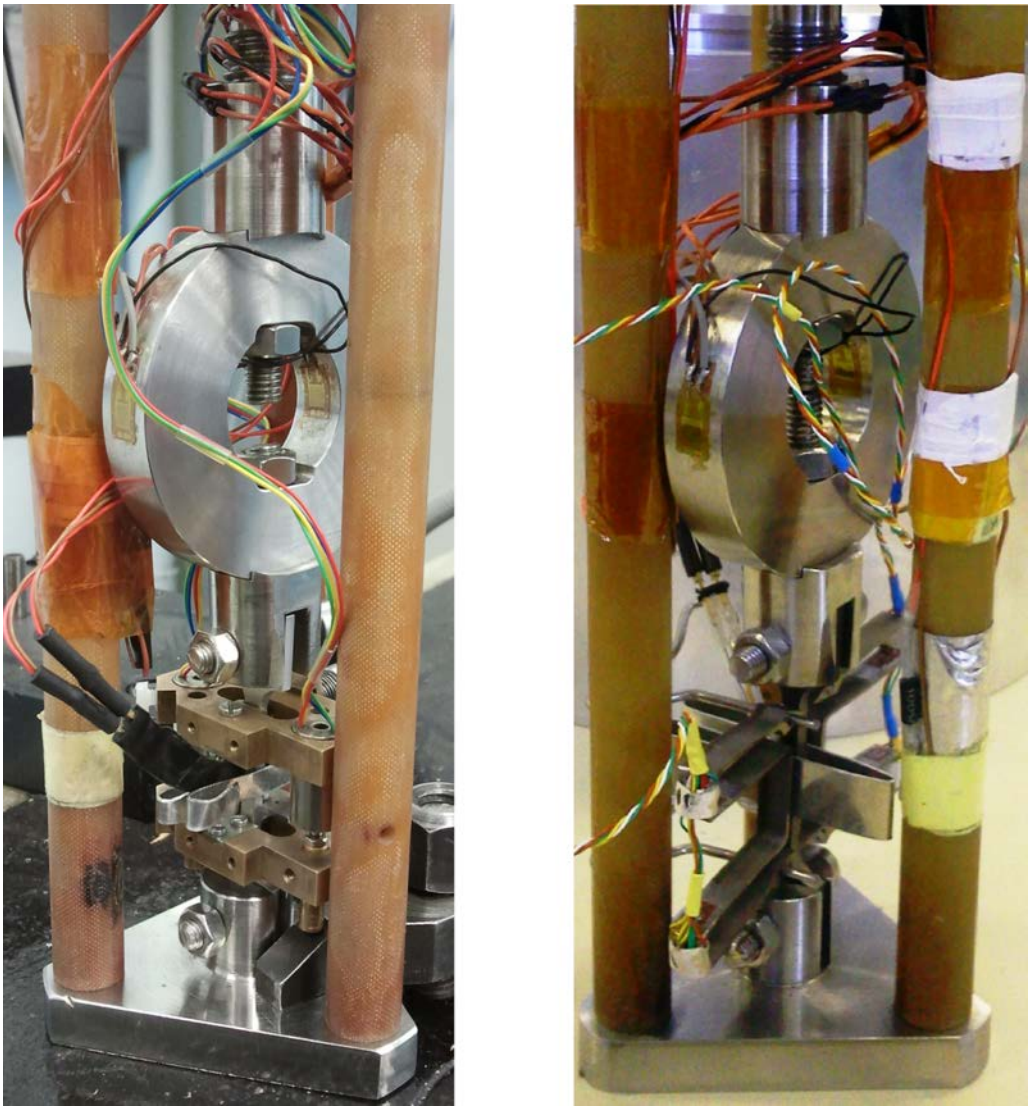

Figure 4.14.: Bottom part of cryostat insert showing mounting of specimen ("old" design) with different sensor setups: with LVDT extensometer (left), and strain gauges extensometer (right).

Load cells

Two types of load cells were used during tensile tests with the above described setup. First, the internal load cell tailor made at CERN, and second, the external load cell supplied from Thames Side Sensors Limited.

The the internal load cell was designed simply as a steel ring equipped with strain gauges (Fig. 4.15, left). The aim was to fall within the following constraints [75]:

- application at very low temperatures (down to absolute zero);
- geometry allowing to place the strain gauges in order to obtain a linear signal;
- limited space inside the cryostat;
- fixings adapted to the stem of traction and the geometry of the specimen.

The dimensions of the sensor steel ring were set to: 53 mm in diameter, 15 mm of thickness and 10 mm of width. The resistances fixed on this annular part of the sensor were the strain gauges 3/350LC11 VISHAY. The force applied along the traction axis induced corresponding deformation of the annular ring and, consequently, deformation of the strain gauges. Therefore, the resistance of

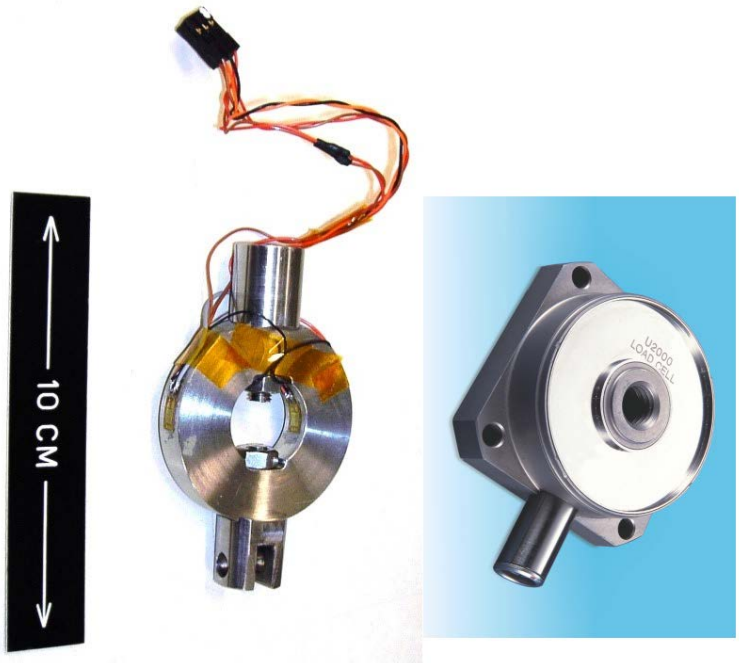

Figure 4.15.: Internal load cell tailor made at CERN (left) and the external load cell supplied from Thames Side Sensors Limited [78] (right).

the gauges R varied according to the formula:

$$\frac{dR}{R} = g\frac{dL}{L} \tag{4.1}$$

where: g is the factor depending on the type of the gauge, and L represents length of the gauge. The gauges were integrated in the Wheatstone bridge and the imbalance voltage measured. Relation between this voltage and the force was obtained by suitable calibration made separately at RT and in liquid helium (4.2 K). The maximum force supported by this load cell at RT was estimated to 4.2 kN, and at cryogenic temperatures (when sensor is fully covered with liquid helium) to the limit of 15 kN (cryostat maximum loading force).

The external load cell Maywood U2000 (Fig. 4.15, right) was mounted between the tensile machine and the cryostat stem of traction (always operating at RT). It could measure force up to 25 kN with the resolution of 0.27 N. The robust shear web design used four strain gauges connected to Wheatstone bridge, was strategically placed to counteract and minimize errors due to unwanted side or non-axial forces [78]. Low deflection and high frequency response were beneficial in high speed measurements, especially where peak loads were being monitored.

Extensometry

Two types of extensometers have been taken into consideration while performing tensile tests. First extensometer was constructed with special support (tailor made at CERN; Fig. 4.16, right) fixed to the specimen through sharp knives holding two Linear Variable Differential Transducers (LVDT) sensors placed on opposite arms of the support. Calculation of the average of two LVDT signals made it possible to compensate for asymmetry in the motion of the frame of the extensometer. Measurement (linear) range of this extensometer covered 3 mm of displacement (specimen's deformation on gauge length) recorded with resolution of 1 μm and response time of 2.5 ms. Second extensometer, the type Nyilas extensometer (supplied by CEME[1]), was made of two spring-like symmetric arms with strain gauges. The extremities of these arms were sharp so they could hold

[1] **C**ryogenic **E**ngineering & **M**aterials **E**xpertise - company founded by retiried dr Arman Nyilas, who developed expertise in cryogenic materials testing and development of test devices during 27 years in KIT [79]

on the specimen surface bind together by the fixation springs. Measurement range of this extensometer covers 15 mm of displacement.

Comparison between two types of extensometers was performed on the basis of maximum acquisition frequency with the minimum measurement noise [80]. One could easily observe on the graphs presenting stress as a function of time and strain as a function of time recorded for DPF phenomenon, large differences between tests carried out with LVDT sensors (Fig. 4.17, top) and tests carried out with strain gauges based sensors (Fig. 4.17, bottom). In the second case, extensometer arms meet their resonance frequency during dynamic phase of PDF phenomenon. In consequence, since the vibrations of extensometer arms disrupt a precise measurement of the test, this extensometer cannot be used to record DPF phenomena.

The inductive LVDT sensors (Fig. 4.16, left) used for the tests are Sensorex SX 9W3 [81] intended for the applications in severe industrial environment: extreme temperatures or pressures, high accelerations and multiple cycles. The LVDT produces an electrical output proportional to the displacement of a free moving core. The body consists of a primary coil powered by an AC signal and two secondary coils. When the core moves inside the coils, voltages in secondary coils are induced, and remain proportional to the displacement. Both secondary coils are connected in series and keep opposite polarities, so that the output

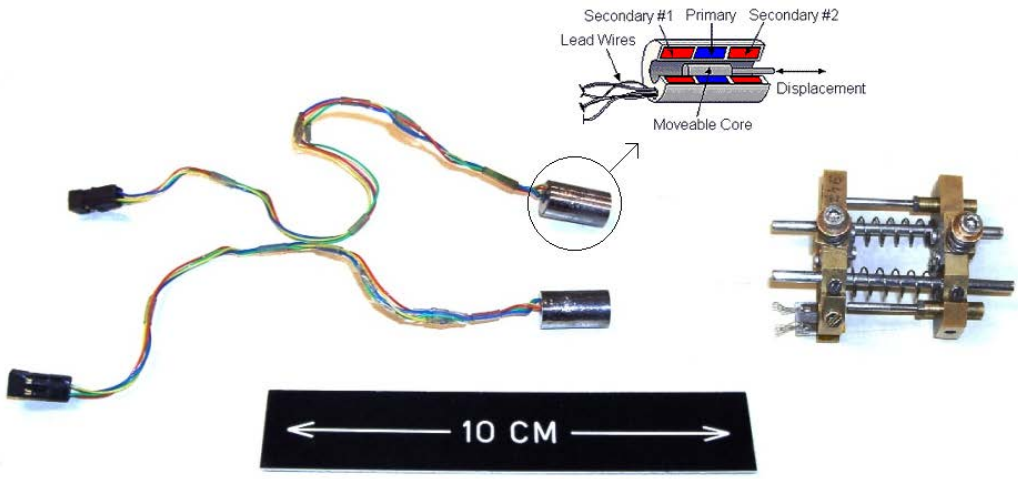

Figure 4.16.: Inductive LVDT sensors Sensorex SX 9W3 [81] (left) and special fixing support tailor made at CERN (right).

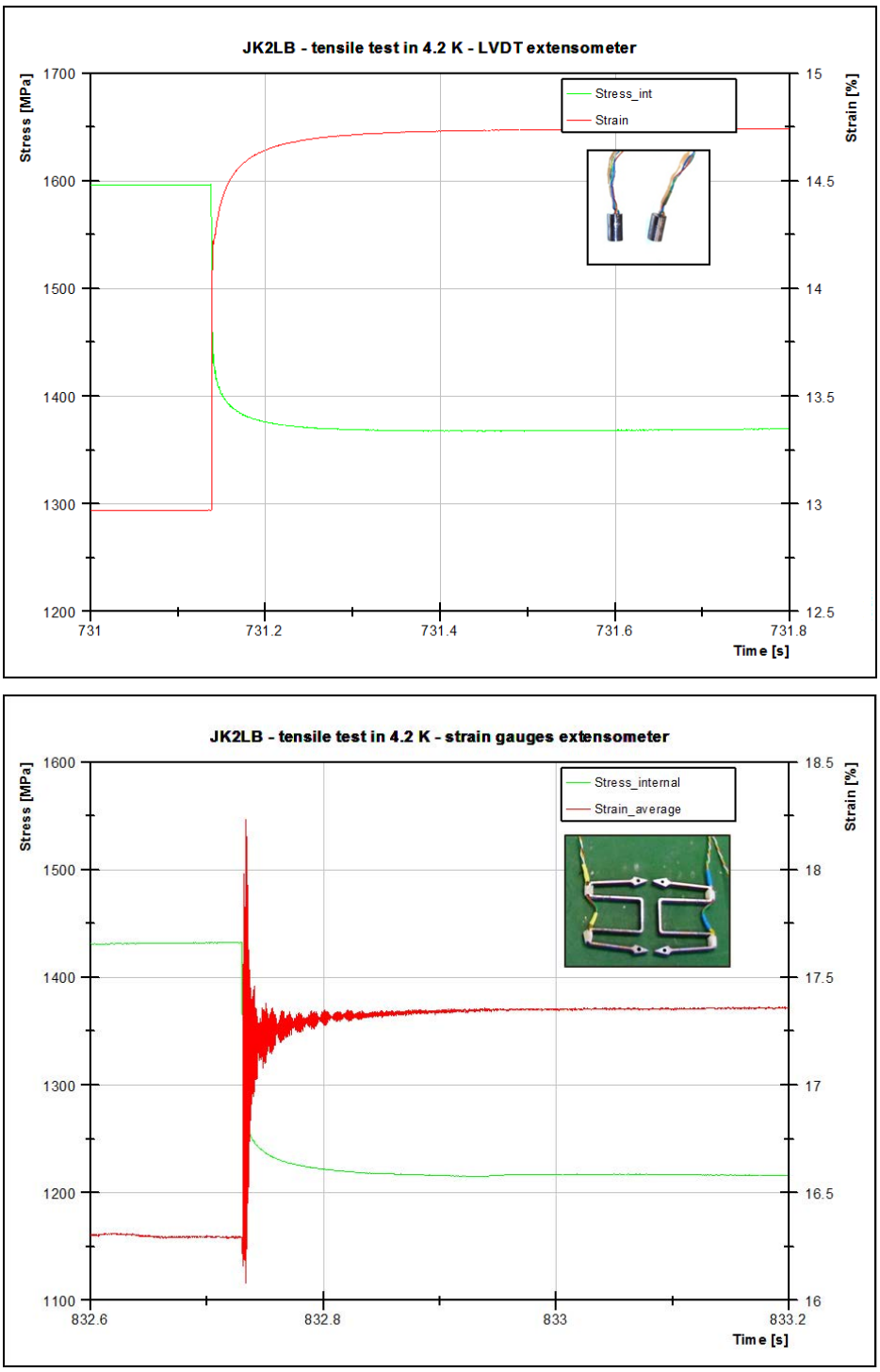

Figure 4.17.: Graphs representing stress as a function of time and strain as a function of time recorded for DPF phenomenon during tests carried out with LVDT sensors (top) and tests carried out with type Nyilas extensometer (bottom).

signal is equal to the difference between these voltages. In this configuration, the output voltage is null when the core is in the centre. When it moves out from the centre, the differential voltage changes. The output voltage is then rectified in order to get a DC signal proportional to the displacement of the core.

Temperature

The temperature sensor used for the measurements is the resistive probe Cernox CX-1050-SD-30 of Lake Shore Cryotronics [82].

This sophisticated sensor had a resolution of 5 mK and a response time of 15 ms at 4.2 K. Its small dimensions (3.2 mm x 1.9 mm x 1 mm) and its weight of 30 mg are well adapted to the tests carried out in the cryostat (Fig. 4.18). The chip was mounted on sapphire base with alumina body. Hermetic lid seal was performed by gold-tin solder. Two gold-plated copper leads were attached for connection purpose. The interior of the case was vacuum tight. A hermetic but - titanium joint guaranteed the sealing.

The sensor was powered by 1/10/100 mV (dependent on operating temperature) through a signal conditioner adapted by CERN for temperatures ranging from 1.6 K to 303 K. The nonlinear curve of resistance as a function of temperature

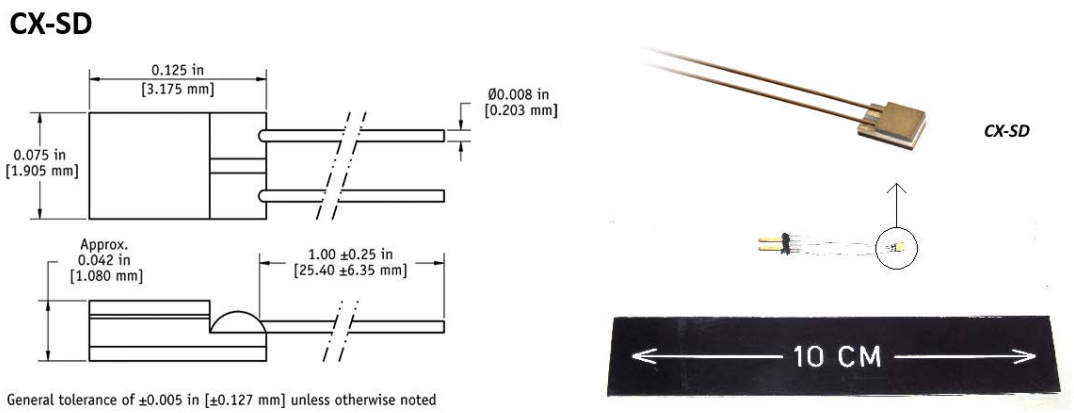

Figure 4.18.: The temperature sensor Cernox CX-1050-SD-30 of Lake Shore Cryotronics [82] with its dimentions (left) and overview (right).

was obtained by means of the Chebychev polynomial.

The sensor was stitched with a thermal grease and held by a spring in the middle of gauge length between the specimens heads.

4.3.4. Data Acquisition System (DAQ)

Optimization of DAQ hardware made it possible to use single amplifier for signal conditioning of all available sensors. The HBM QuantumX MX840A amplifier [83] (Fig. 4.19), selected for this purpose, had 8 universal inputs and supported more than 10 transducer technologies (including half bridges and ohmic resistors). The module had the low voltage connection, the Ethernet interface for data communication with an operating PC, the status LEDs for displaying general system and channel states. Each measurement channel is characterized by the following features: electrical isolation, configurable supply voltage for active sensors, configurable sampling rate and active digital filter (Bessel, Butterworth). Maximum achievable data rate was of 19200 samples/s and operating bandwidth of 3200 Hz.

Figure 4.19.: The HBM QuantumX MX840A amplifier with 8 universal input channels.

The software, HBM Catman (Fig. 4.20), used for data recording and analysis was well adapted to work with the described amplifier. The Catman was optimally suited for the following tasks:

- configuring measurement channels as well as the computation tasks;

- individual graphical visualization in real time during test;
- graphical analysis of recorded data;
- exporting measurement data into commonly used data formats (Excel, ASCII, DIAdem, etc.).

Optimized DAQ system, with the QuantumX and the Catman, gave this advantage over the previous measurement setup that it held data record with stable frequency during full time of test as well as precise time read out recorded as a separate channel.

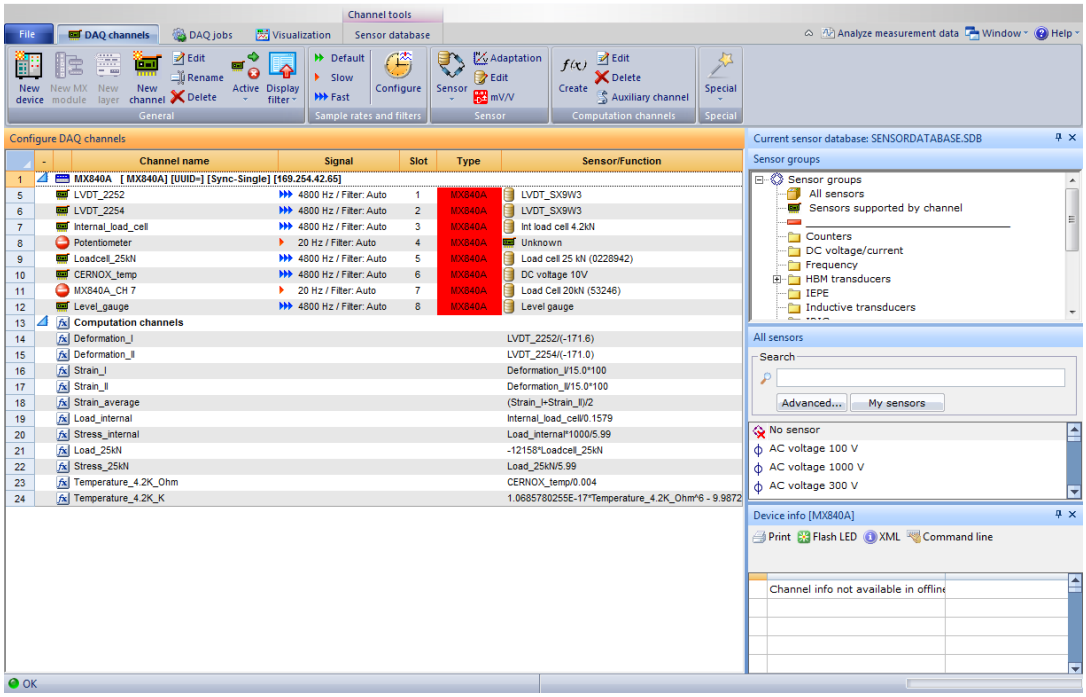

Figure 4.20.: Catman software main panel loaded with test project containing sensor and computation channels.

4.4. Fatigue Crack Growth Rate

This additional cryogenic measurement task dealt with fatigue crack growth rate (FCGR) and fracture toughness tests of 316LN and JK2LB grades [84]. Tests were carried out at a temperature of 7 K using the available cryogenic mechanical testing facility at the Karlsruhe Institute of Technology (KIT) [85].

4.4.1. FCGR Specimen

Compact tension specimens were machined according to ASTM E1820 standard [86], as shown in Fig. 4.21 (right). The minimum wall thickness of material samples (approximately 8 mm) allowed machining two compact tension specimens of about 4 mm thickness for standard FCGR and fracture toughness tests. The machined notch length (designated as "a") to specimen width (designated as "w") ratio was in the case of FCGR specimens 12/36 or 0.33 (technical drawing shown in Fig. 4.21, left). Immediately after the FCGR tests where the crack length to width ratio increased from 0.33 to around 0.6 the fracture toughness measurement started at the same temperature (7 K) using the single specimen J-Integral procedure. In case of specimens for direct J-test without a FCGR measurement process prior to J-test the starting a/w ratio was 0.5 mm. Two orientations of the jacket (see Sections 4.1.2 and 4.2.1) were tested where the crack propagation orientation was either longitudinal or transverse. In order to check reproducibility two specimens were machined for each orientation.

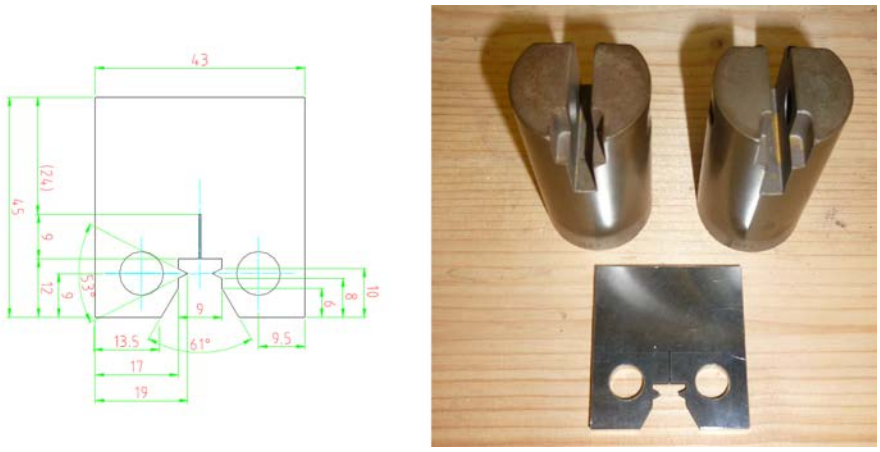

Figure 4.21.: The FCGR test specimens with accordance to ASTM E1820 standard: technical drawing (left) and machined specimen with special mounting grips (right).

4.4.2. Test Method

The FCGR measurements were conducted at a load ratio of 0.1 (F_{min}/F_{max}). The cryogenic facility is described by Nishimura et al. [87] (Fig. 4.22, left). To follow the crack position, specially designed extensometer was used which was

fixed at the load line of the compact tension specimen (Fig. 4.22, right). The crack length resolution using the extensometer was better than 1 μm. After cool down to around 20 K the cycling has been started at 30 Hz frequency. After each 10 000 cycles the frequency was reduced to 0.03 Hz. During this ramp up and down action the slope load versus displacement was acquired. All this procedure was computerized and the data were saved for post evaluation. After pre-cracking the temperature was adjusted to 7 K. Using the relation a/w one is able to follow the crack position remotely with a displacement transducer positioned at the load line of an ASTM proportional compact tension specimen.

Following this procedure, the crack propagation started from the electro-discharged notch position could be determined. Once the crack reached the length of around 0.5 mm, the machine was stopped and the post-evaluation of data was carried out. The range of the stress intensity factor ΔK has been adjusted to the level of 20 MPa$\sqrt{m}$ and kept constant throughout the test sequence. The crack propagation was monitored at each ramp up and down at reduced frequencies to save the evaluated data in the form of a table.

Figure 4.22.: Cryogenic mechanical testing facility at KIT [85] (left) and specimen mouted by means of special grips and with on purpose designed extensometer (right).

4.4.3. Data Processing

The FCGR given as da/dN with respect to stress intensity factor range ΔK has been studied. To evaluate da/dN as function of ΔK, the recorded plot of crack length (a) versus cycle number (N) has been smoothed using computerized software. The inverse value of the derivatives of these plots at distinct crack length positions gave the value of da/dN. The crack length position along with the specimen geometrical details and the constant load range gave the ΔK values at this specific position. Finally, the plot da/dN versus ΔK could be constructed, using the above determined data for the specific specimen, in a double logarithmic scale. Considering the stable crack growth propagation, region II shown in Fig. 4.23, the experimental results were plotted according to the following expression of Paris' (power) law [88, 89]:

$$\frac{da}{dN} = C_1 \Delta K^{m_1} \tag{4.2}$$

where C_1 and m_1 are constants obtained from the fitting curve.

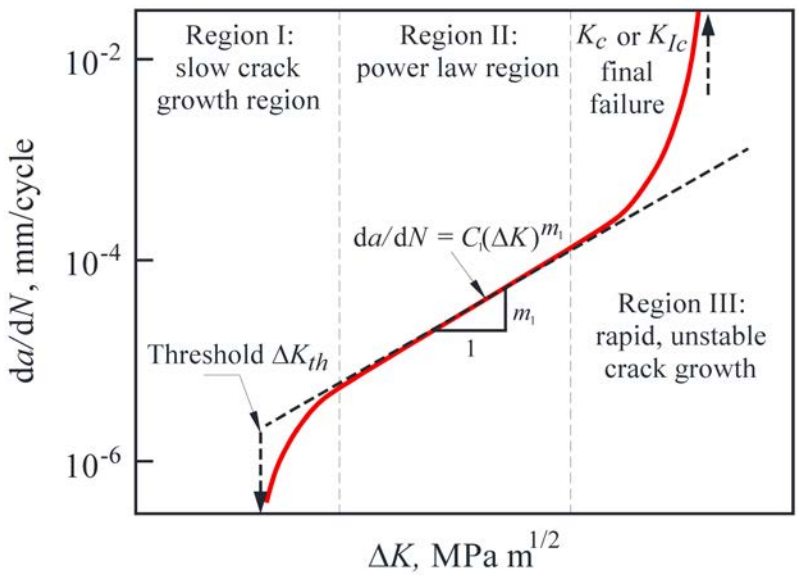

Figure 4.23.: Schematic plot of the FCGR and the range of the stress intensity factor. The Paris (power) law is calibrated to model the linear interval at about the middle range of the power law region [90].

5. Experimental Results

This chapter introduces experimental results obtained during metallurgical observations, tensile tests and FCGR measurements for 316LN and JK2LB grades at successive steps of production process.

First, the metallurgical results are shown divided into four groups, starting with inclusion content measurement and comparison between the grades and states. Second, a cross check of the microstructure is carried out in order to confirm that the grades are fully austenitic, followed by description and comparison of grain sizes of the products. Last, the effect of heat treatment is shown as appearance of carbide precipitation on grain boundaries.

Next section is dedicated to the results of tensile tests performed at RT and in liquid helium (4.2 K). The emphasis is put on details of discontinuous plastic flow phenomenon and comparison of its appearance in 316LN and JK2LB, tested in the same state.

Finally, an outlook of FCGR results is provided, performed on both grades in various metallurgical states. The FCGR results are put in correlation with results of grain size and tensile tests to identify the effect on the mechanical properties of the microstructure, as resulting from the history of the thermomechanical process of the material.

5.1. Surface Analysis

The metallurgical qualifications presented in this section were performed as a part of systematic study, carried out at CERN [91, 92, 93, 94, 95, 96, 97, 98, 99, 100], of materials supplied by IO.

The following points were checked with respect to the requirements of ITER technical specification (ITER_D_2LTKVM [101]):

- Inclusion: when examined in accordance with ASTM E45, Method D, the micro-inclusion content shall not exceed Field Number 2 for inclusion types A, B, C and D. The worst area of the specimen shall be selected to determine the rating. The tolerance for acceptance may be a half-class above the set limit to the extent of 2% of the fields counted. Macro-inclusions (exogenous inclusions from entrapped slag or refractories) are strictly forbidden and are cause of rejection.

- Ferrite content: any trace of δ-ferrite visible on micrographs, following suitable etching, at a magnification of 500x and in particular alignment of this phase shall be cause for rejection.

- Grain size: the equivalent grain size number according to ASTM E112-96(2004) shall be, on average, within the range from 2 to 4. The grain size shall be homogeneous within the range of ± 1 equivalent grain size number around the true average value.

5.1.1. Inclusions Content

Inclusion content measurements were performed by optical microscopy, according to ASTM E45 method D [67]. Results for 316LN grade in as cold worked state (CW, includes compaction and stretch forming) and as CW + heat treatment (HT) state, as well as JK2LB grade in as extruded (standard annealing) state and as CW state are presented in Table 5.1.

Analyses have been made, for each of the listed materials and states, on over 320 fields and allowed rating of A type inclusions (sulfide), B type inclusions (aluminates), C type inclusions (silicate) and D type inclusions (oxides), respectively. The worst severity observed, for each sample separately, was:
- level 2 for 316LN CW (example measurement field in Fig. 5.1a),
- level 1 for 316LN CW HT (example measurement field in Fig. 5.1b),
- level 2 for JK2LB extruded (example measurement field in Fig. 5.2a),
- level 1.5 for JK2LB CW (example measurement field in Fig. 5.2a).

Inclusion content (maximum class 2) of all the provided shapes met the

Material	Inclusion classification over 320 fields measured								
	Severity	Type A		Type B		Type C		Type D	
		Thin	Heavy	Thin	Heavy	Thin	Heavy	Thin	Heavy
316LN CW	0.5	0	0	81	0	15	8	80	29
	1	0	0	53	1	14	4	51	24
	1.5	0	0	0	0	2	0	1	0
	2	0	0	3	0	0	0	0	2
316LN CW HT	0.5	10	0	63	5	8	9	65	30
	1	1	0	6	0	1	0	3	5
	1.5	0	0	0	0	0	0	0	0
	2	0	0	0	0	0	0	0	0
JK2LB extruded	0.5	4	0	74	5	1	0	113	53
	1	0	0	23	0	1	0	13	9
	1.5	0	0	0	0	0	0	0	0
	2	0	0	1	0	0	0	0	0
JK2LB CW	0.5	4	2	95	18	15	23	98	81
	1	0	0	72	10	5	8	11	10
	1.5	0	0	2	0	0	0	0	1
	2	0	0	0	0	0	0	0	0

Table 5.1.: Results of the inclusion content measurements, following ASTM E45 method D.

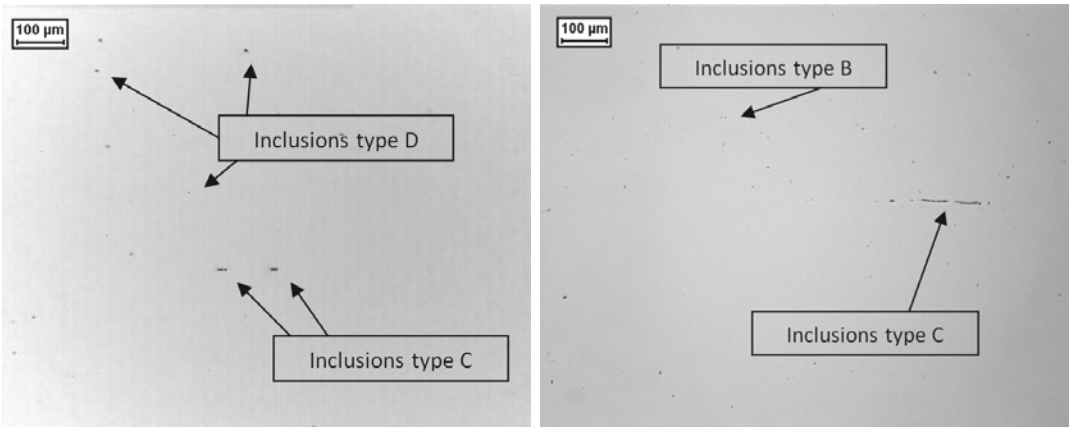

(a) 316LN CW (b) 316LN CW + HT

Figure 5.1.: Examples of optical observations on the longitudinal as polished sections of 316LN grade, original magnification 100x.

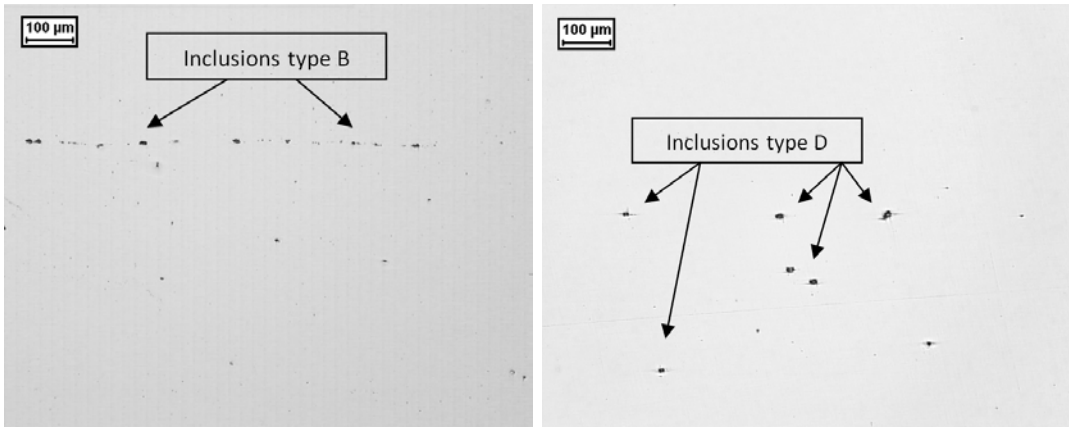

(a) JK2LB extruded (b) JK2LB CW

Figure 5.2.: Examples of optical observations on the longitudinal as polished sections of JK2LB grade, original magnification 100x.

specification requirements for the final product. As tensile straining or ageing are not likely to influence inclusion content, minor differences in measured severity level can be explained by measurements performed at random locations. The dispersion can be considered representative of the distribution of inclusions within the different products. Therefore, the above mentioned results can be considered valid for as compacted state as well. For the same reason, as not likely to be changed by ageing, inclusion content was not assessed again after heat treatment of JK2LB grade.

5.1.2. Austenitic Structure

Cross check of the austenitic structure was carried out by searching for the occurrence of ferrite within materials microstructure. Optical observations after Murakami etching (according to standard ASTM E407 N° 98 [68]), on transverse and longitudinal sections of both grades, were performed at an original magnification of 500x (see Fig. 5.3 and Fig. 5.4).

Absence of ferrite was checked on 316LN grade in CW state (Fig. 5.3a) and CW + HT state (Fig. 5.3b). The same procedure was carried out on JK2LB grade in extruded state (Fig. 5.4a), CW state (Fig. 5.4b) and CW + HT state (Fig. 5.4c). No ferrite was detected conform to specification. Following results, there is no significant influence of the heat treatment on the possible occurrence

of delta ferrite neither on 316LN grade nor on JK2LB grade.

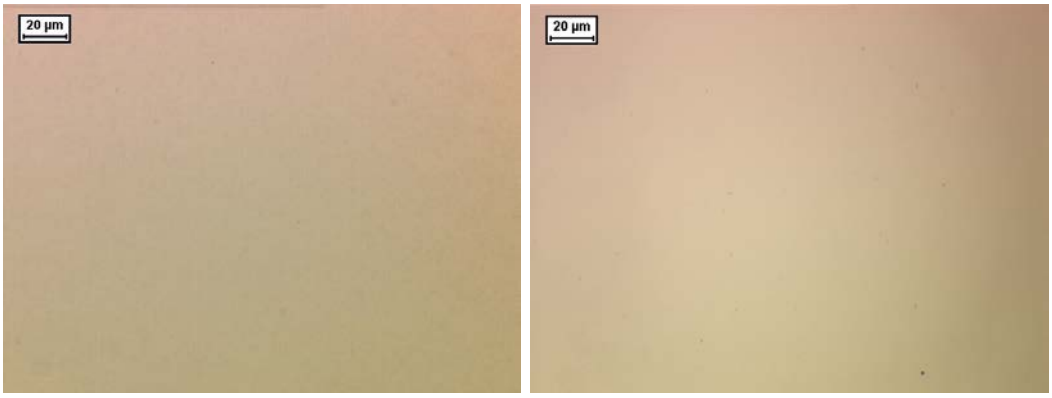

(a) 316LN CW (b) 316LN CW HT

Figure 5.3.: Optical observations on 316LN grade after Murakami etching, original magnification 500x.

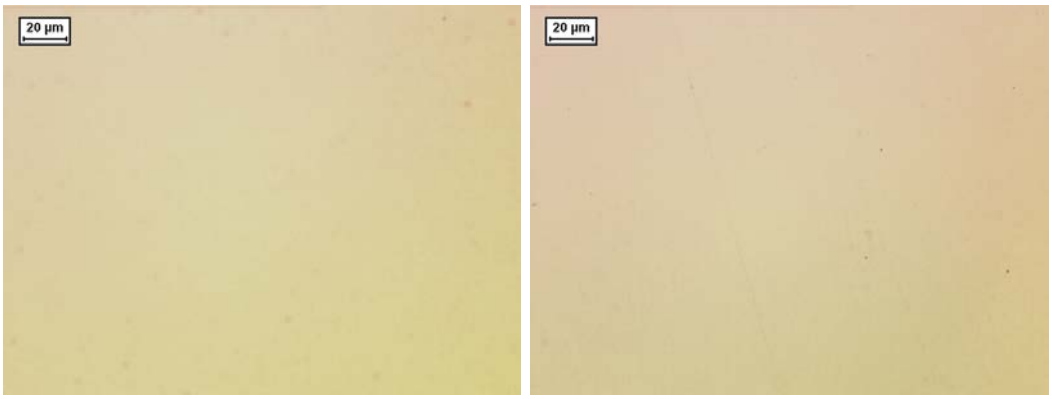

(a) JK2LB extruded (b) JK2LB CW

(c) JK2LB CW+HT

Figure 5.4.: Optical observations on JK2LB grade after Murakami etching, original magnification 500x.

Following the fact that ferrite in the compacted and strained products was not detected after Murakami etching, and that tensile straining is not likely to influence ferrite content, the results mentioned above can be considered valid for as compacted state as well.

5.1.3. Grain Size

Grain size measurement has been performed according to standard ASTM E112 [69]. To reveal grain boundaries under microscopic observation, electrolytic etching with oxalic acid was applied:

- for 316LN according to standard ASTM E407 [68], N° 13: 10 % KOH + H_2O under 6 V for 60 s;
- for JK2LB according to standard ASTM A262 [70]: 10 % KOH + H_2O under 1 A/cm^2 for 90 s.

Grain size number of 316LN grade in CW state, observed with magnification of 100x (Fig. 5.5a), is G $\approx$ 5 $\div$ 5.5. Within the limits of experimental dispersion, compaction and stretching did not significantly influence grain size (typical value is 5.5 after standard solution annealing). The results are identical for heat treated state observed with the same magnification of 100x (Fig. 5.5b). Therefore, the heat treatment did not influence grain size in this case.

The results obtained for extruded JK2LB grade (standard solution annealing) are similar to 316LN. Grain size G $\approx$ 5, is measured at a magnification of 100x (Fig. 5.6a). The results for CW state (Fig. 5.6b) and CW + HT state (Fig. 5.6c) of JK2LB grade, both observed with 200x magnification, showed grain size numbers G $\approx$ 6 $\div$ 6.5 and G $\approx$ 5 $\div$ 5.5, respectively. Grain growth due to ageing, corresponding to a lower grain size number in the ASTM scale, could be observed with comparison to not aged state.

Grain size number in all cases is higher than upper allowed limit (as per ITER technical specification [101]). Based on collected experimental data, it was stated and confirmed that higher toughness and lower FCGR at cryogenic temperature go consistently with the evidence that fine grain is favorable in terms of ductility and strength. Therefore, derogation was given following advantageous results for a finer grain size.

Significant difference in appearance of grain boundaries (see Fig. 5.6c) is

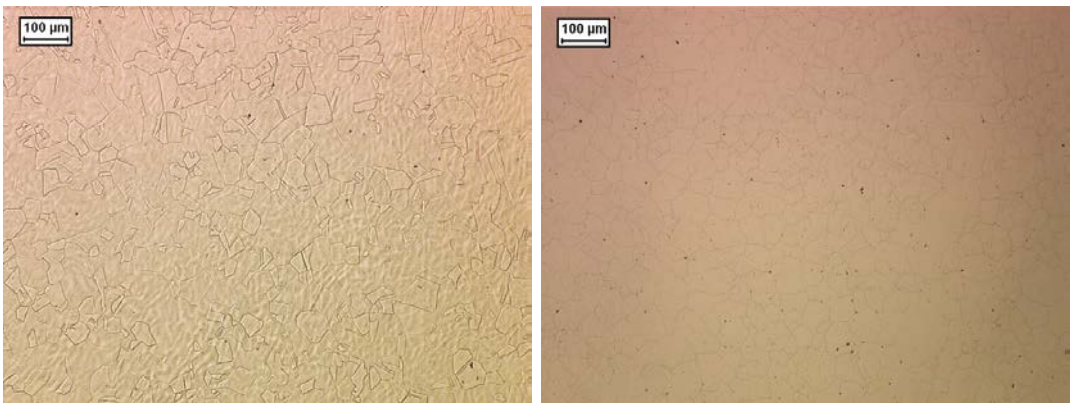

(a) 316LN CW, magn. 100x (b) 316LN CW HT, magn. 100x

Figure 5.5.: Grain size assessment in 316LN grade after electrolytic etching with oxalic acid, transverse direction.

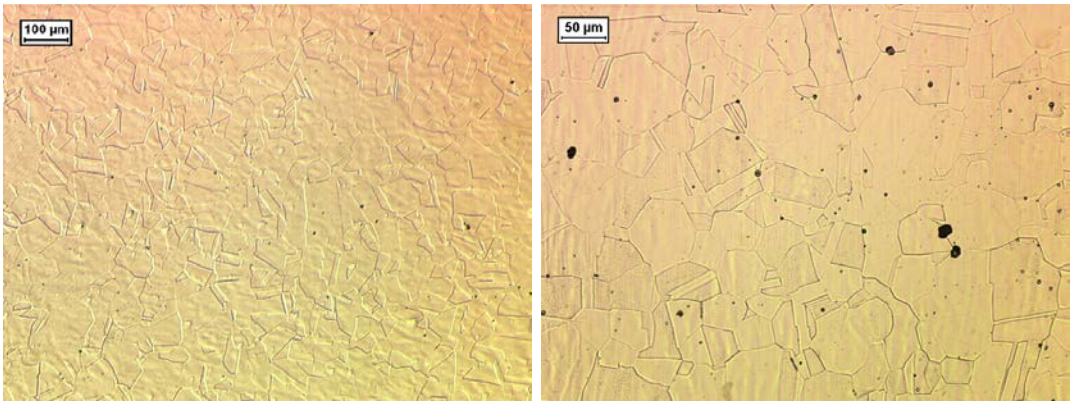

(a) JK2LB extruded, magn. 100x (b) JK2LB CW, magn. 200x

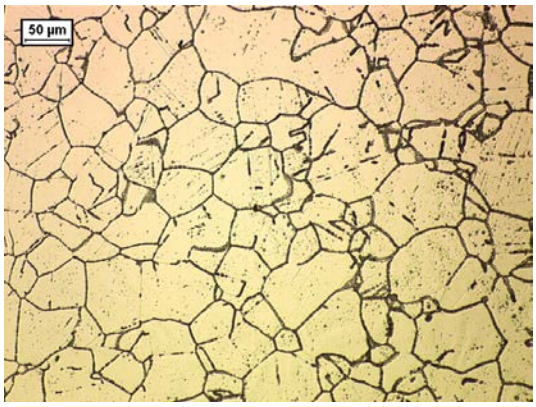

(c) JK2LB CW+HT, magn. 200x

Figure 5.6.: Grain size assessment in JK2LB grade after electrolytic etching with oxalic acid, transverse direction.

caused by the sensitization effect due to heat treatment. Carbide precipitation at grain boundaries reacted stronger with electrolytic eatching resulting in ditches surrounding grains.

5.1.4. Carbide Precipitation

The ageing heat treatment described in Section 4.1.3 was performed in both cases (316LN and JK2LB) with the following temperature steps:
-> 210 °C for 50 hrs
-> 340 °C for 25 hrs
-> 450 °C for 25 hrs
-> 575 °C for 100 hrs
-> 650 °C for 200 hrs
After heating steps, cooling phase followed with the temperature decreasing rate less than 20 °C/h (see Fig. 5.7).

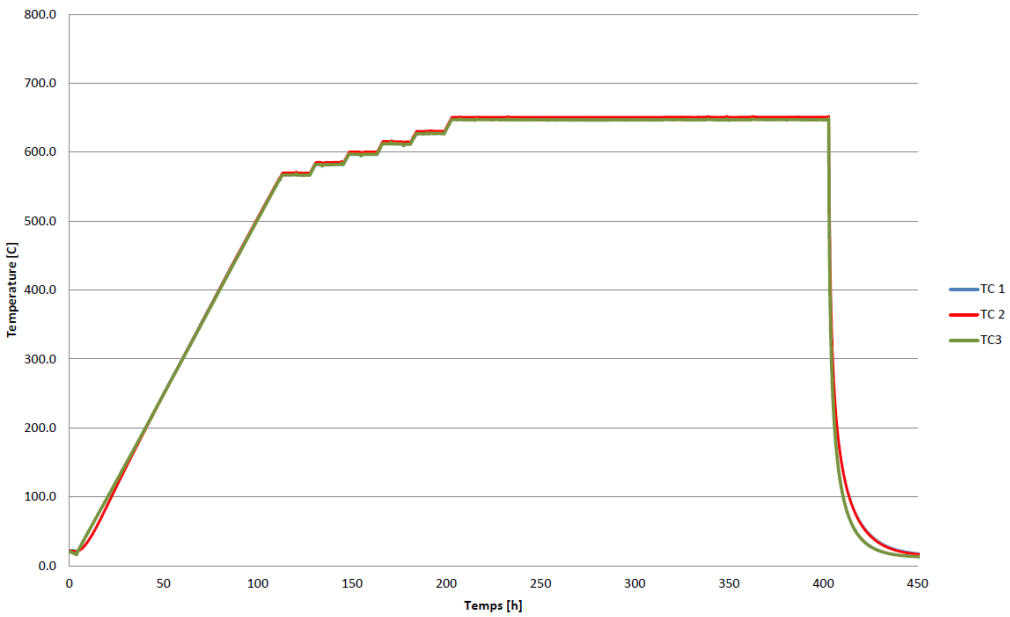

Figure 5.7.: Record, by 3 independent temperature sensors placed inside furnace, of heat treatment cycle performed on austenitic stainless steel samples for application to ITER magnets using Nb_3Sn superconductor.

To reveal structure, the same electrolytic etching with oxalic acid as for grain boundaries was applied on samples:

- for 316LN according to standard ASTM E407, N° 13 [68]: 10 % KOH + H_2O under 6 V for 60 s;
- for JK2LB according to standard ASTM A262, Practice A [70]: 10 % KOH + H_2O under 1 A/cm^2 for 90 s.

Optical observation of materials after ageing confirmed sensitization with precipitates visible at the grain boundaries (Fig. 5.8a and Fig. 5.9a). Sample without ageing submitted to the same etching, does not respond to the chemical attack (Figs 5.8b, 5.9b).

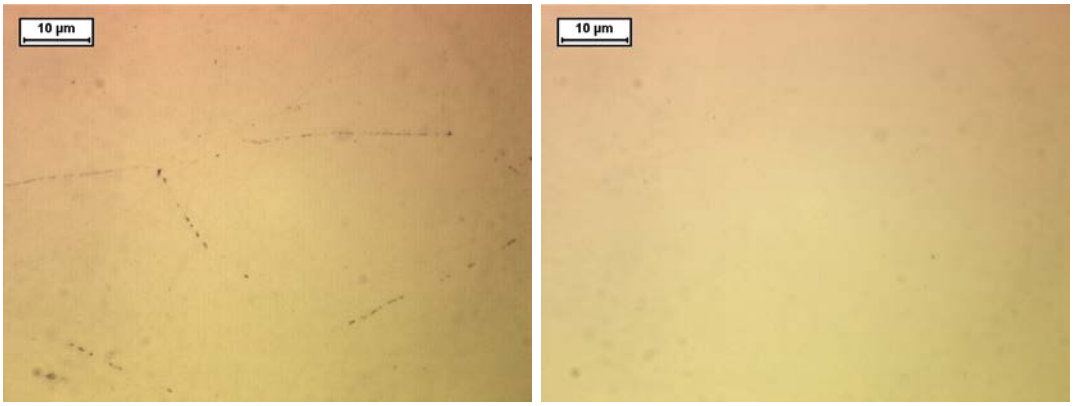

(a) 316LN CW+HT (b) 316LN CW

Figure 5.8.: Comparison between the aged sample (a) and the non-treated sample (b) of 316N grade, original magnification 1500x. The chemical attack, according to ASTM E407 (N° 13: 10 % KOH + H_2O, 6 V, 60 s), revealed carbides precipitation at the grain boundaries due to the heat treatment.

Pictures of 316LN grade with original magnification of 1500x (Fig. 5.8) showed presence of ditches at grain boundaries after ageing (dual structure following ASTM A262), contrary to non-treated piece which showed unsensitized step structure free of ditches.

In case of JK2LB, pictures made with original magnification of 500x (Fig. 5.9), severity can be classified as ditch structure (according to ASTM A262, most grains completely surrounded). For comparison, as expected, a step structure (only steps between grains, no ditches at grain boundaries) was observed for the non-aged sample issued from the same material.

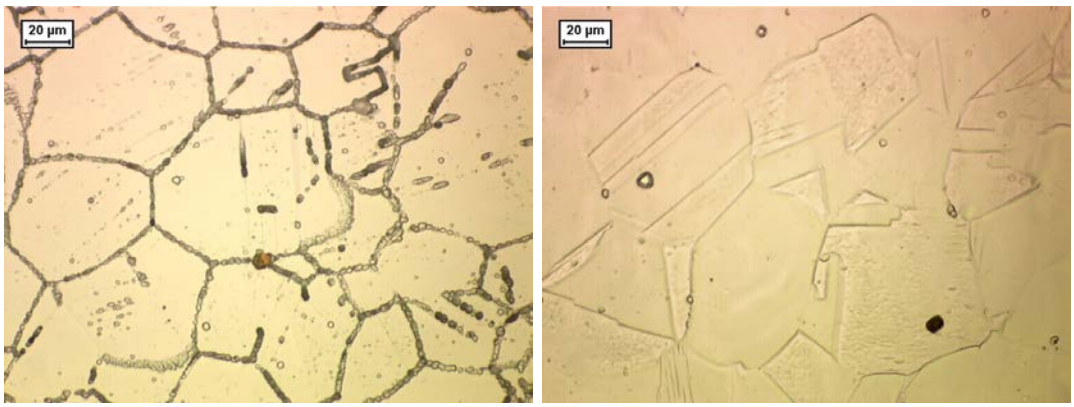

(a) JK2LB CW+HT (b) JK2LB CW

Figure 5.9.: Comparison between the aged sample (a) and the non-treated sample (b) of JK2LB grade, original magnification 500x. The chemical attack, according to ASTM A262 (Practice A: 10 % KOH + H_2O, 1 A/cm^2, 90 s) revealed carbides precipitation at the grain boundaries due to the heat treatment.

5.2. Tensile Tests

The tensile tests in liquid helium (4.2 K) and RT presented in this section were performed as part of systematic study on 316LN and JK2LB grades. All tests carried out at CERN [96, 97, 98, 102, 103, 104, 105], on materials supplied by IO, were focused on providing information about mechanical properties, like yield strength, ultimate tensile strength and ductility.

The parameters obtained during tensile tests as well as detailed high frequency records of stress, strain and temperature were used for calibration of the constitutive model (see Section 6).

5.2.1. Materials Strength and Ductility

Summary results of tensile properties (yield strength $Rp_{0.2}$, ultimate tensile strength Rm and ductility A) are presented in the following groups:
- extruded state (standard solution annealing) in Fig. 5.10,
- cold worked (CW) state (includes compaction and 2.5 % straining) in Fig. 5.11,
- CW after heat treatment (CW + HT) in Fig. 5.12.

Groups presented in dedicated charts reflect results for 316LN and JK2LB grades tested at room temperature (RT) and in liquid helium (4.2 K).

First plot (Fig. 5.10) with extruded JK2LB shows significant increase of strength of material at cryogenic temperature compared to RT. Yield strength and tensile strength at 4.2 K feature values ($Rp_{0.2}$ = 1128 MPa, Rm = 1455 MPa) more than twice higher to these obtained at RT ($Rp_{0.2}$ = 463 MPa, Rm = 633 MPa). As expected, higher strength resulted in lower ductility in liquid helium showing A = 32.2 % decreased from A = 46.1 % at RT.

Applied cold working process (see Section 4.1.3) influenced materials in a predictable way, which means obtaining higher strength and lower ductility compared to extruded state (standard solution annealing). It is worth mentioning that the CW process of JK2LB was heavier compared to the one applied to 316LN. Heavy CW was aimed to improve the surface roughness of JK2LB (by a skin pass drawing), that underwent heavy oxidation due to the high Mn content. Fig. 5.11 shows comparison between 316LN and JK2LB grades tested in the same conditions. JK2LB in CW state showed higher strength and lower ductility at RT ($Rp_{0.2}$ = 649 MPa, Rm = 704 MPa, A = 33.3 %) as well as in cryogenic

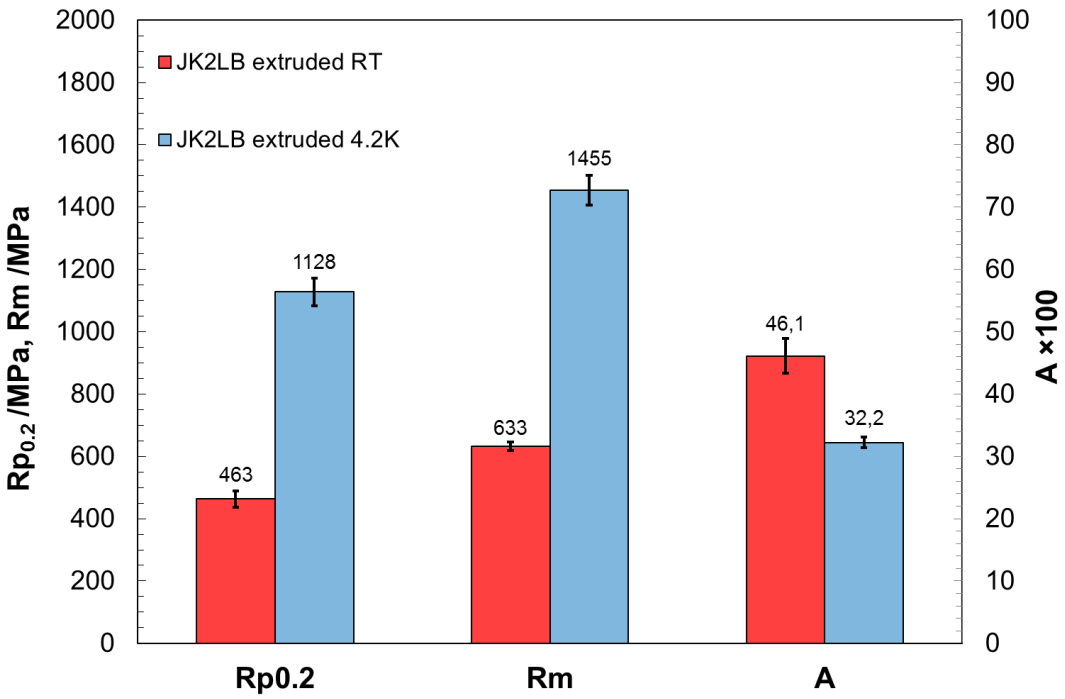

Figure 5.10.: Column chart presenting mechanical parameters obtained in tensile tests performed on extruded JK2LB at RT and in liquid helium (4.2 K).

environment ($Rp_{0.2}$ = 1367 MPa, Rm = 1627 MPa, A = 28.2 %) compared to 316LN in CW state tested at RT ($Rp_{0.2}$ = 492 MPa, Rm = 658 MPa, A = 50.9 %) and at 4.2 K ($Rp_{0.2}$ = 1021 MPa, Rm = 1529 MPa, A = 35.0 %).

The results of JK2LB extruded and CW samples show material hardening revealed by rising of ultimate tensile strength at RT by ΔRm = 71 MPa and at 4.2 K by ΔRm = 172 MPa. Taking into account that CW process includes tensile stretching, which can be seen equivalent to pre-straining operation on tested sample, obtained results for JK2LB grade reflect raised yield strength by $\Delta Rp_{0.2}$ = 186 MPa at RT and $\Delta Rp_{0.2}$ = 239 MPa at 4.2 K. Following this point of view, the measured elongation is lower due to pre-elongated sample after CW resulting in ductility reduced by ΔA = 12.8 % at RT and ΔA = 4.0 % at 4.2 K.

Last column chart presented in Fig. 5.12 provides comparison of tensile tests results between 316LN and JK2LB grades after heat treatment (CW + HT). For both grades one can observe partial annealing of material resulting in the decrease of yield strength at RT ($Rp_{0.2\ 316LN}$ = 413 MPa, $Rp_{0.2\ JK2LB}$ = 490 MPa) and

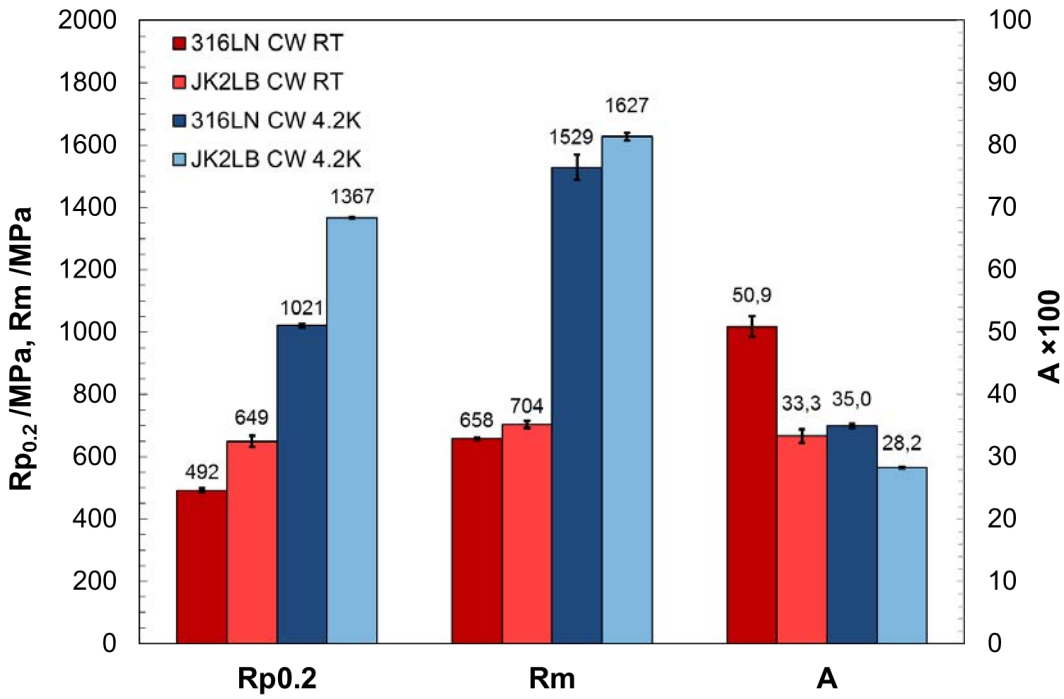

Figure 5.11.: Column chart presenting mechanical parameters obtained in tensile tests performed on cold worked 316LN and JK2LB at RT and in liquid helium (4.2 K).

at 4.2 K ($Rp_{0.2\ 316LN}$ = 938 MPa, $Rp_{0.2\ JK2LB}$ = 1222 MPa) with respect to the CW state. On the other hand ultimate tensile strength stayed at almost the same level for 316LN grade (Rm_{RT} = 658 MPa, $Rm_{4.2\ K}$ = 1553 MPa), but went down for JK2LB grade (Rm_{RT} = 675 MPa, $Rm_{4.2\ K}$ = 1478 MPa) resulting in value at 4.2 K lower than in the case of 316LN. Finally, ductility after CW + HT is slightly higher, with respect to CW state, in most cases ($A_{RT\ 316LN}$ = 51.9 %, $A_{4.2K\ 316LN}$ = 37.7 %, $A_{RT\ JK2LB}$ = 40.2 %) beside low temperature tests of JK2LB grade ($A_{4.2K\ JK2LB}$ = 23.2 %). Even though the sensitization phenomenon provokes fragility of grain boundaries in cryogenic environment, the lower ductility of JK2LB after HT is more likely due to the higher applied CW: the ductility could not be restored at the same high levels of 316LN, the latter having experienced a lower CW. From the present results it appears that the difference in ductility is not only a question of sensitization (JK2LB generally resists better than 316LN to the reaction HT).

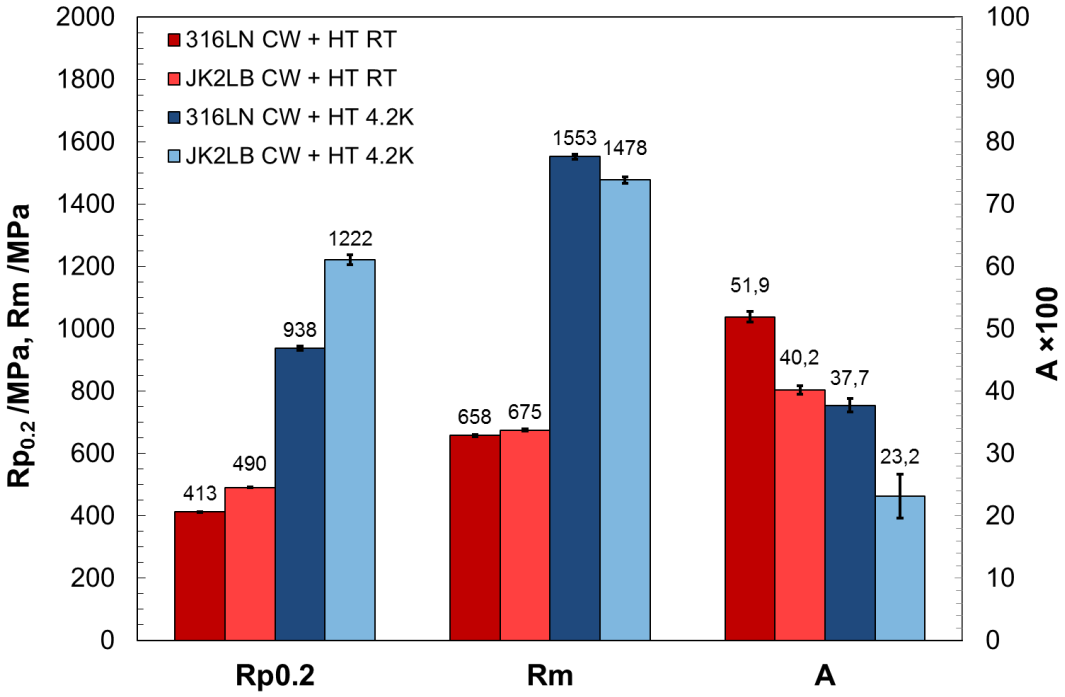

Figure 5.12.: Column chart presenting mechanical parameters obtained in tensile tests performed on cold worked and heat treated 316LN and JK2LB at RT and in liquid helium (4.2 K).

5.2.2. Analysis of Stress-Strain Curves

Representative stress-strain curves have been selected to describe materials behavior during tensile tests. The three graphs presented below are directly associated to three column charts shown in previous section. Each of them shows representative stress-strain curves related to certain material, sample state and test temperature. All graphs show stress σ in MPa on y-axis, and strain ϵ in % on x-axis. Due to extensometry limitations, and emphasizing most interesting part of the curve, all graphs presented below are limited to 25 % of strain. It neither means the end of the test, nor the fracture of the specimen. Final results of tensile tests have been reported in the previous section.

Fig. 5.13 presents a portion of the stress-strain curve of extruded JK2LB obtained with 300 Hz sampling frequency at RT (the lower smooth curve featuring as well an unloading loop for better Young's modulus measurement) and in

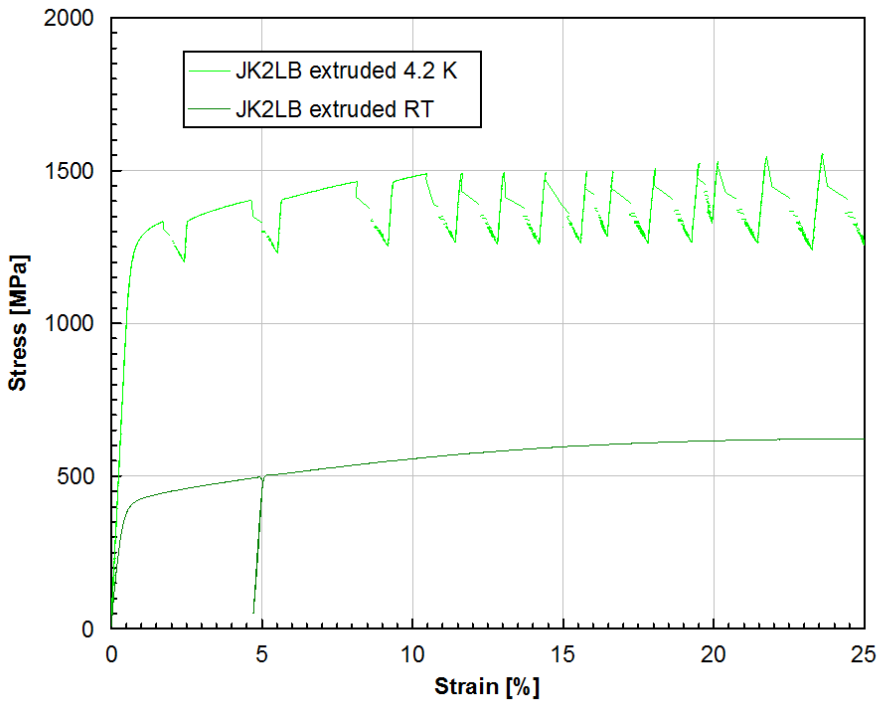

Figure 5.13.: Graph of stress as a function of tensile strain for extruded JK2LB grade at RT (300 Hz sampling frequency, unloading loop around 5 % of strain for better E modulus measurement), and at cryogenic temperature (4.2 K, 2400 Hz sampling frequency, resonance noise due to a spring based extensometer).

liquid helium with 2400 Hz sampling frequency (upper serrated curve with visible resonance noise due to a spring based extensometer), respectively. Clearly visible is not only material strengthening due to low temperature (already reported in Fig. 5.10), but most of all the discontinuous plastic flow phenomenon appearing in plastic deformation curve (contrary to smooth plastic deformation at RT). Additionally, the unloading-loading used for precise measurement of Young's modulus E was applied on RT curve around 5 % of strain.

Next graph (Fig. 5.14) reflects stress-strain curves of cold worked 316LN and JK2LB grades tested in the same conditions (RT and 4.2 K), respectively. Different appearance/shape of serrated yielding between curves of CW materials and the one of extruded JK2LB comes from the fact of using LVDT extensometer instead of previously used Nyilas-type extensometer (for details see Section 4.3.3). Avoiding resonance noise during low temperature data recording, made it possible to record with higher sampling frequency: 4800 Hz (for both 4.2 K tensile tests).

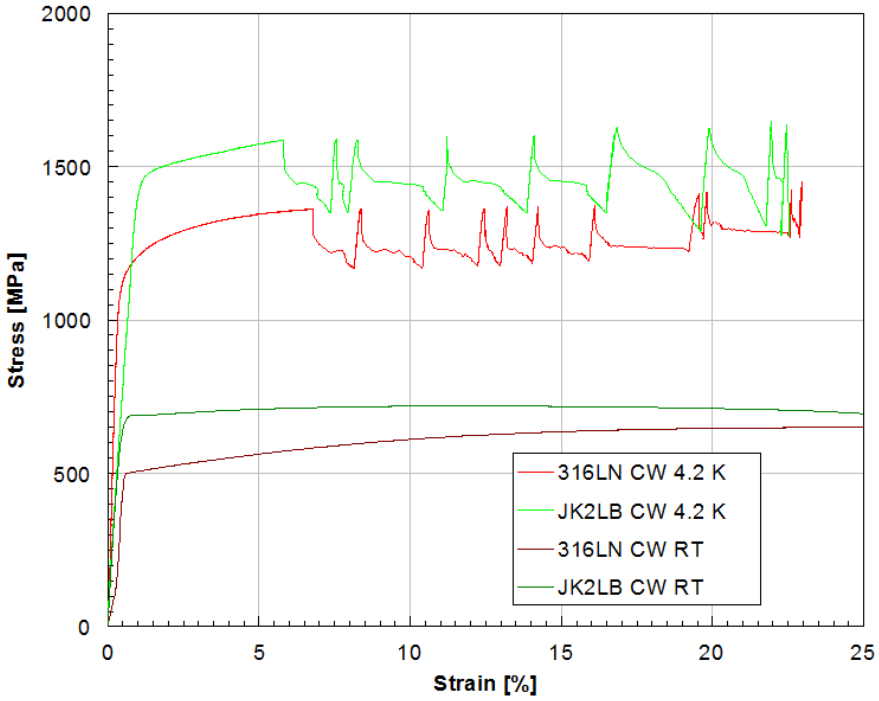

Figure 5.14.: Graph of stress as a function of strain showing tensile tests results for cold worked 316LN and JK2LB grades at RT (300 Hz sampling frequency), and at cryogenic temperature (4.2 K, 4800 Hz sampling frequency, LVDT extensometer).

JK2LB (green curve) features higher strength regardless the temperature of the test (as seen before in Fig. 5.11).

Finally, curves of cold worked and heat treated materials tested at RT and at cryogenic temperature are presented in Fig. 5.15. Significant loss of material strength is observed for JK2LB at 4.2 K. Plastic hardening influenced by phase transformation (more in the case of 316LN than JK2LB) results in higher tensile strength of 316LN (see Fig. 5.12). It seems that the influence of heat treatment on material inner stress relaxation is linked to the DPF phenomenon in the way of smaller serrations in single appearances, compared to preceding tests. Worth mentioning is also exceptionally dense occurrence of serrations at the beginning of plastic deformation line of JK2LB grade.

Once again, the unloading-loading line can be noticed in RT curve of JK2LB grade around 5 % of strain.

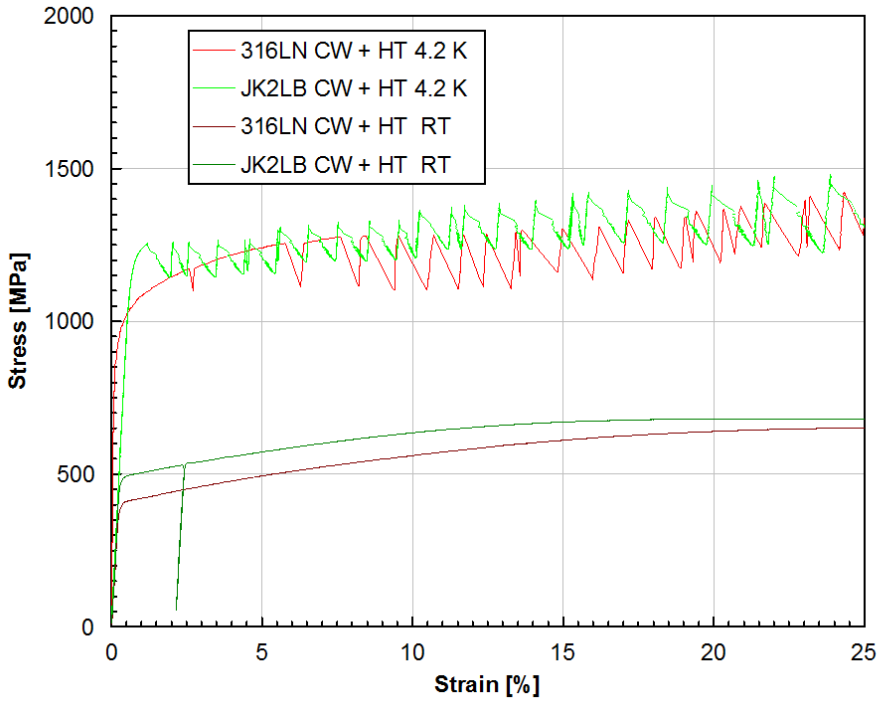

Figure 5.15.: Graph of stress as a function of strain showing tensile tests results for cold worked and heat treated: 316LN at RT (300 Hz sampling frequency) and at 4.2 K (600 Hz sampling frequency, Nyilas-type extensometer) and JK2LB at RT (300 Hz sampling frequency) and at 4.2 K (1200 Hz sampling frequency, Nyilas-type extensometer).

5.2.3. The DPF in Stress-Strain Curves

The DPF phenomenon, which was observed in the stress-strain curves for each material and sample state tested at cryogenic temperature, was measured in details by using cold worked 316LN and JK2LB stress-strain curves. Analyses were made on single occurrence of DPF, extracted from curves of both materials. Presented in Fig. 5.16 are serrations magnified from plastic deformation line of 316LN CW and JK2LB CW. In both cases, the elastic deformation can be easily identified on this part of curve where the stress is sharply climbing. Just after, when the material reaches the plastic deformation zone, sudden drop of load is observed with following deformation step. Finally, the relaxation part can be seen as mild drop of stress with accompanying rise of strain.

Additionally, the temperature measurement is provided corresponding with stress-strain lines of each material. The peak of temperature in each case of serration occurrence is located at the end of relaxation part, visible in stress-strain curve. Beside this area, the temperature remains relatively stable within duration of the tensile test.

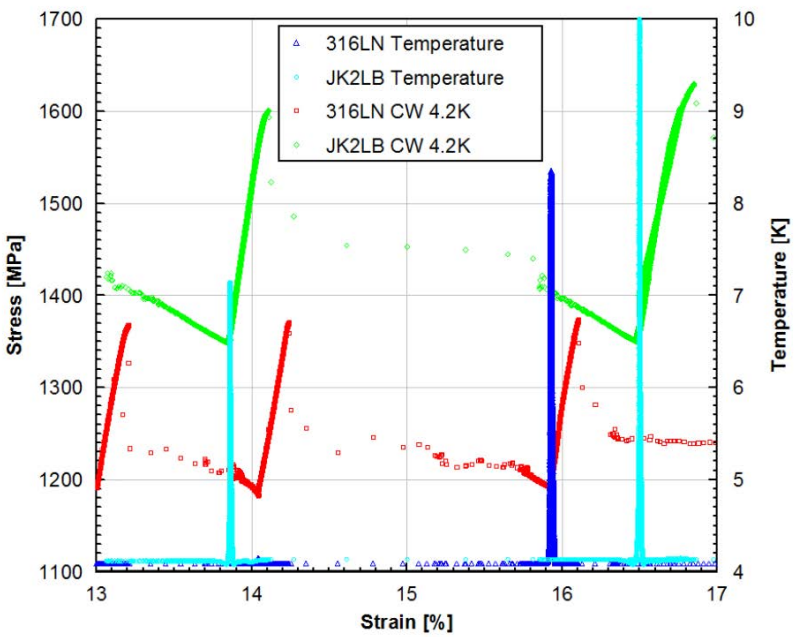

Figure 5.16.: Extracted part of the stress-strain curves of cold worked 316LN and JK2LB grades, showing detailed view of single DPF occurrence accompanied by temperature measurement.

Extracted serrations were analyzed closer by presenting stress, strain and temperature as a function of time. Graphs dedicated separately to 316LN grade (Fig. 5.17) and JK2LB grade (Fig. 5.18) are shown below. Due to high frequency record and precise time measurement, one can appreciate point representation of test data underlining speed of DPF process in selected areas. Taking into account amount of collected data during test, the points shown in these graphs had to be limited to provide better visualization (1 per 10 for stress and strain; 1 per 100 for temperature).

Taking advantage of stress and strain time representation, it is seen that the sudden load drop is taking place almost in the very same moment as the deformation step, in extremely short time slot. It is also visible that the temperature rise starts at the point of sudden drop of stress and jump of strain, but it seems to be more extended in time. This depends on the point were T probe is placed and on the thermal diffusivity of the material.

It is important to notice that the temperature peaks presented here together

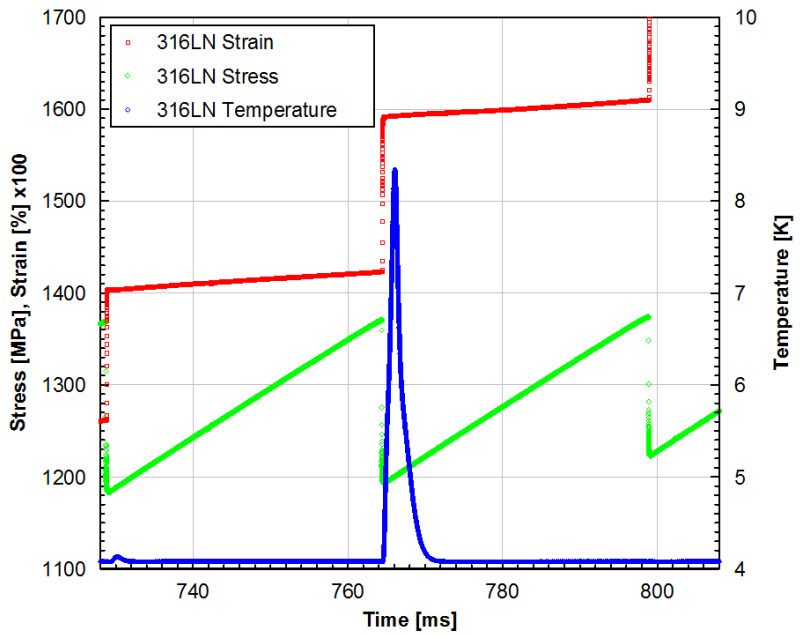

Figure 5.17.: Extracted single serration of cold worked 316LN grade presented in the form of graph of stress, strain and temperature as a function of time with selected representation of test data (1 per 10 for stress and strain; 1 per 100 for temperature).

with stress and strain lines are only qualitative representation. Due to the way of mounting the temperature sensor on the specimen surface and sensor size itself, the location of serration appearance within the specimen volume affects significantly quality of measurement (by heat diffusion process).

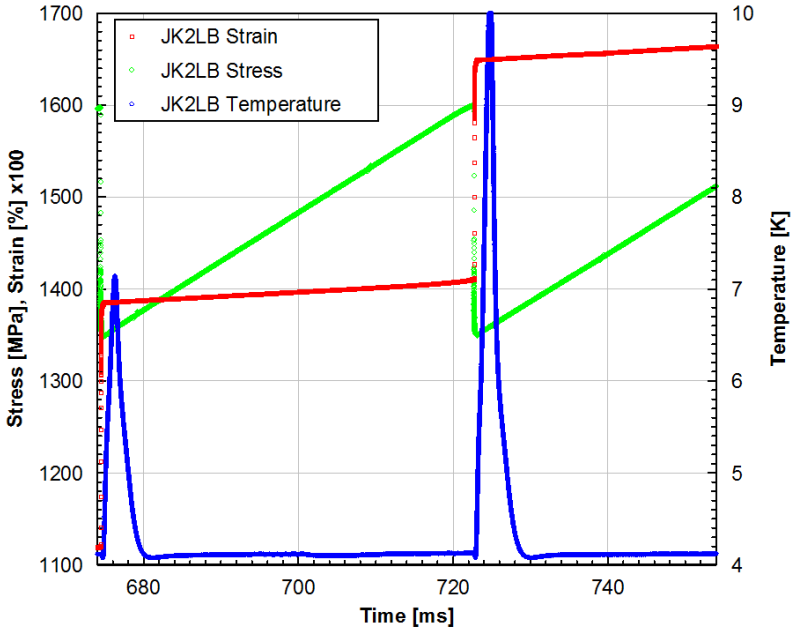

Figure 5.18.: Extracted single serration of cold worked JK2LB grade presented in graph of stress, strain and temperature as a function of time with point representation of test data (1 per 10 for stress and strain; 1 per 100 for temperature).

5.3. Supplementary mechanical tests

5.3.1. The FCGR

The 316LN grade

Fig. 5.19 shows results of FCGR measurements carried out at 7 K on 316LN material [23]. Compaction (CO), stretching 2.5 % (ST_2.5%) and aging (HT - heat treatment) applied to the samples having undergone standard annealing (SA) treatment do not significantly degrade FCGR properties. Limited sensitization (carbide precipitation at grain boundaries) maintains favorable fatigue

crack growth rates, in spite of cold working (CW) applied by compaction and stretching. The material shows excellent isotropy, with negligible difference between longitudinal (LD) and transverse direction (TD).

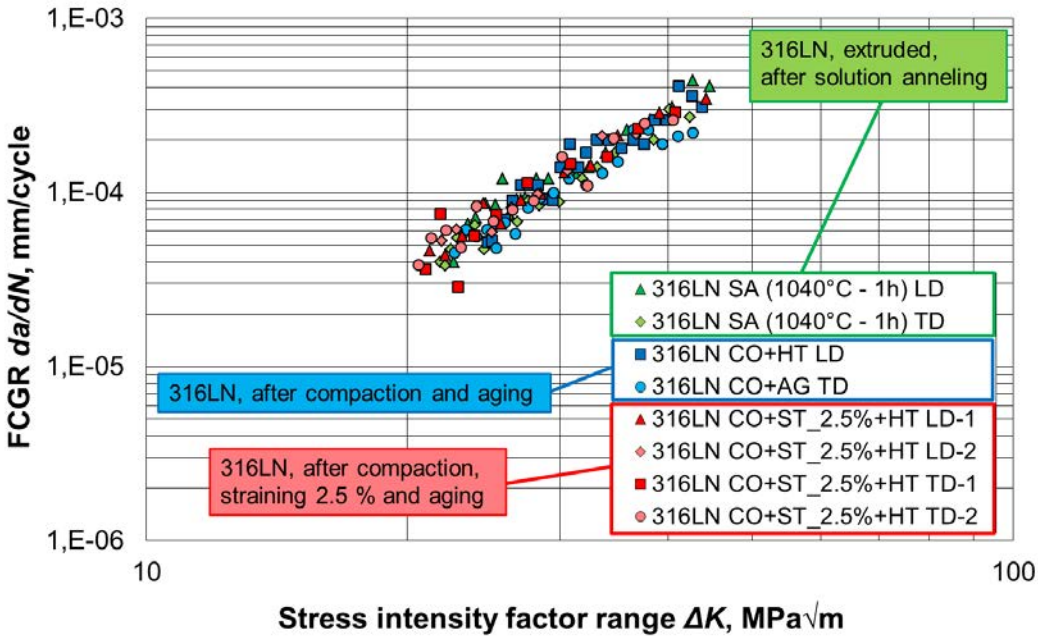

Figure 5.19.: FCGR measurements carried out at 7 K on 316LN material: solution annealed (SA); compacted (CO) and heat treated (HT); and compacted, stretched (ST) and heat treated. Each tested in longitudinal (LD) and transverse (TD) directions.

The JK2LB grade

Fig. 5.20 shows results of FCGR measurements carried out at 7 K on JK2LB material [61]. Compaction and aging (CO+HT), and compaction stretching 2.5 % and aging (CO+ST_2.5%+HT) result in very similar rates. For grain size in the same range, crack growth rates are generally lower or equivalent to those shown by 316LN having undergone the same processing steps. The material shows excellent isotropy, with negligible difference between LD and TD series. The tensile stretching has negligible effect on FCGR results.

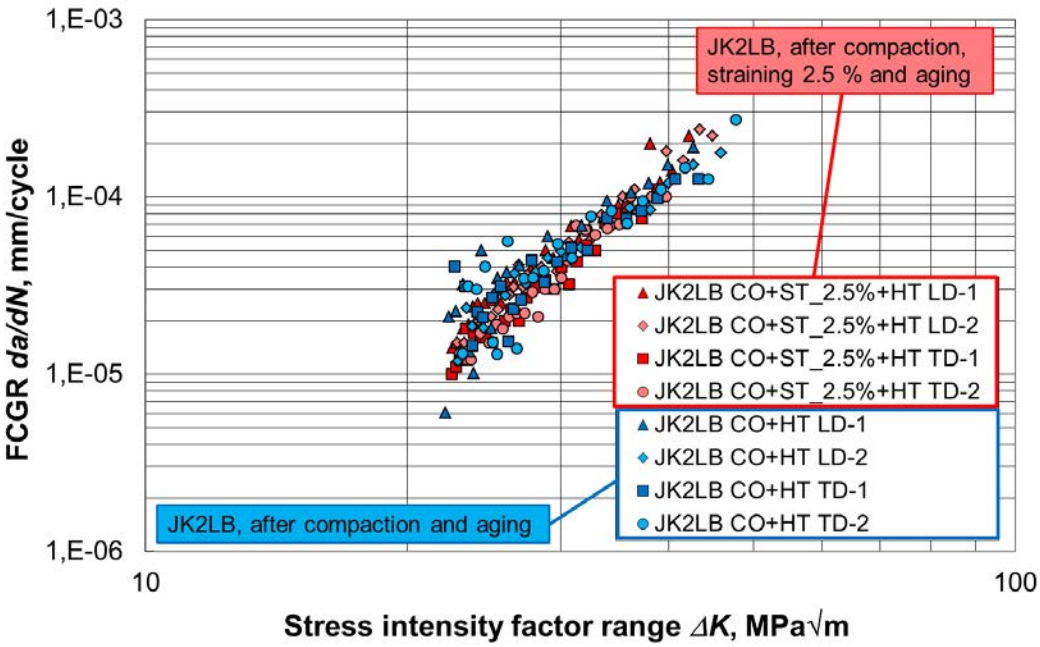

Figure 5.20.: FCGR measurements carried out at 7 K on JK2LB material: compacted and heat treated (CO+HT); and compacted, stretched and heat treated (CO+ST_2.5%+HT). Each tested in longitudinal (LD) and transverse (TD) directions.

Comparison

Comparing the FCGR series of compacted and aged 316LN and JK2LB material, focused on the lowest and the highest ΔK, JK2LB generally shows lower FCGR than 316LN series. Nevertheless, compacted and aged 316LN shows performance comparable to JK2LB.

5.3.2. Fracture Toughness

K_{IC}(J) values were also systematically evaluated for all the series for which FCGR was tested. In particular, for the series of compacted and aged 316LN shown in Fig. 5.19 K_{IC}(J) is on average 277 MPa$\sqrt{}$m, and for the series of compacted and aged JK2LB shown in Fig. 5.20 164 MPa$\sqrt{}$m, well above the ITER requirement of 130 MPa$\sqrt{}$m. Measured K_{IC} values do not significantly depend on the testing direction.

For compacted and aged JK2LB, K_{IC}(J) is on average 158 (167.5) MPa$\sqrt{}$m

for the LD (TD) of crack propagation, while for compacted, tensile stretched and aged JK2LB K_{IC}(J) is 104.5 (118.5) MPa$\sqrt{}$m. The latter values are below the minimum specified toughness of 130 MPa$\sqrt{}$m. Lower values are due to the application of skin pass drawing, inducing a considerable work-hardening in the SA temper.

Fig. 5.21 summarizes the results of low temperature K_{IC}(J) measurements, plotted as a function of $Rp_{0.2}$ for different series of 316LN and JK2LB grades. For both series, different states are compared: standard solution annealed (SA, 1040 °C during 1 h), compacted (CO) after heat treatment (HT) and CO + stretched 2.5% after HT.

Finer grain size of 5 to 5.5, as resulting from standard SA, is also retained after aging. Due to lower $Rp_{0.2}$, 316LN features in all states higher fracture toughness than JK2LB, well above 200 MPa$\sqrt{}$m. Despite the different chemical analysis and product origin, all fine grained JK2LB and 316LN series follow the same trend of dependence of K_{IC}(J) on $Rp_{0.2}$. It is worth to highlight here again the favorable role of fine GS on toughness and crack growth, which equally applies to the two grades.

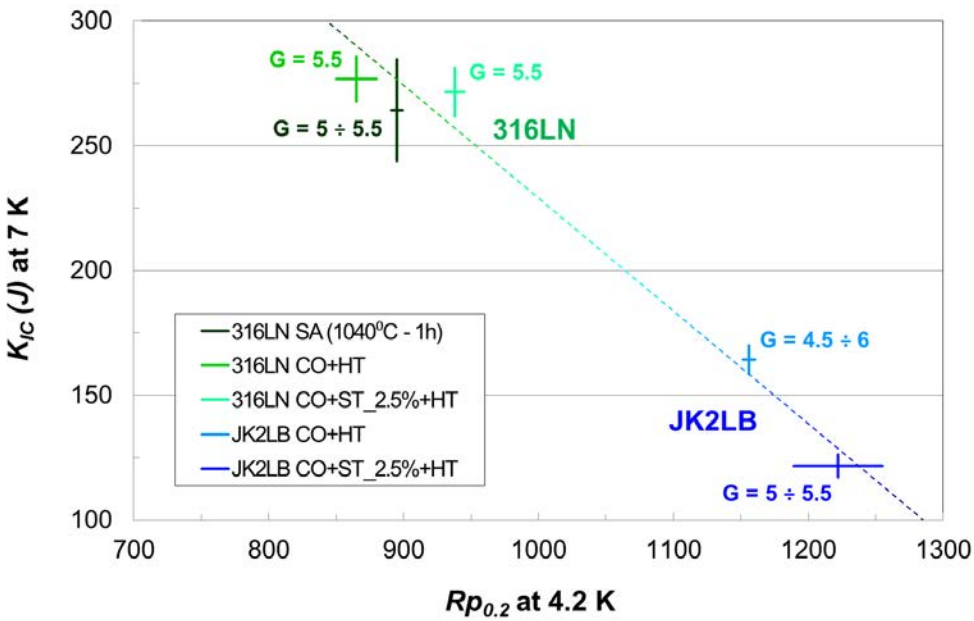

Figure 5.21.: Fracture Toughness as a function of yield strength for 316LN and JK2LB grades, with results trend line.

6. Constitutive Model

This chapter introduces description of the DPF multiscale model together with the numerical algorithm based on this model [8]. It also gives details of parameters used for evaluation of stress-strain curves of 316LN and JK2LB grades.

It starts with a walk-through the DPF kinetics, showing at first relation to the dynamic strain ageing effect. The mechanism of dislocation pile-ups formation at obstacles like Lomer-Cottrell locks is presented.

Following physics of the DPF model, the numerical algorithm is shown divided in the consecutive steps: initial state, elastic deformation, plastic deformation, serration and relaxation.

Finally, the parameters used in the above mentioned algorithm (for 316LN and JK2LB grades) are given based on literature and experimental data.

6.1. DPF Multiscale Model

The DPF reflects the effect of dynamic strain ageing occurs at very low temperatures. It is related to the mechanism of dislocation pile-ups formation at strong obstacles such as Lomer-Cottrell (LC) locks [30]. The number of dislocations in the group multiplies in a proportional way the shear stress at the head of dislocation pile-up. At the same time, the motion of new dislocations is blocked by the back stresses of dislocation groups. Following the critical level of stress concentration at the leading edge, a catastrophic failure of the LC locks occurs locally and spreads over a larger portion of the material as an avalanche process. Developing this way, it leads to massive motion of released dislocations and simultaneous generation of dislocations by new sources, which together influence the step-wise increase of the strain rate. The process which

initially seamed to be only microscopic, grows into macroscopic scale, and can be observed as load drops in the stress-strain curve.

In order to provide a mathematical description of this process, one has to compute local shear stress τ as a function of the amount of crystallographic slip γ. Assuming that the local dislocations density at a given temperature T is denoted by ρ, the evolution of dislocation density with deformation is described by the following equation:

$$\frac{d\rho}{d\gamma} = \left.\frac{d\rho}{d\gamma}\right|_{+} + \left.\frac{d\rho}{d\gamma}\right|_{-} \tag{6.1}$$

where the component denoted by "+" represents the dislocations production rate, and the component denoted by "-" stands for the dislocations annihilation rate [35]. The production part is given by the following relation:

$$\left.\frac{d\rho}{d\gamma}\right|_{+} = \frac{1}{\lambda b} \tag{6.2}$$

where λ is the mean free path of dislocation and b denotes length of the Burgers vector. The annihilation part is expressed by the formula:

$$\left.\frac{d\rho}{d\gamma}\right|_{-} = -k_a \rho \tag{6.3}$$

with k_a standing for the dislocation annihilation constant. The mean free path of dislocation obeys the following rule:

$$\lambda = \frac{1}{\sum_i \lambda_i^{-1}} \tag{6.4}$$

where λ_i represents the mean free path related to a specific type of obstacle. In the simplest case:

$$\frac{1}{\lambda} = \frac{1}{d} + k_1\sqrt{\rho} \tag{6.5}$$

with d denoting the average grain size and k_1 being a constant. Combining the above-shown equations one obtains:

$$\frac{d\rho}{d\gamma} = \frac{1}{db} + \frac{k_1}{b}\sqrt{\rho} - k_a\rho \tag{6.6}$$

Assuming the following relations for the macroscopic stress and strain:

$$\sigma = M\tau \tag{6.7}$$

$$\gamma = M\epsilon \tag{6.8}$$

where M is the Taylor factor, and accepting that:

$$\epsilon \approx \epsilon^p \tag{6.9}$$

the following formula can be derived:

$$\frac{d\rho}{d\epsilon^p} = M\left[\frac{1}{db} + \frac{k_1}{b}\sqrt{\rho} - k_a\rho\right] \tag{6.10}$$

Making reference to Eq. 2.2 and assuming that:

$$\epsilon^p \geq \epsilon^p_{LC} \tag{6.11}$$

where ϵ^p_{LC} represents a plastic strain threshold above which the LC barriers massively develop, the increment of density of the LC barriers gives:

$$\dot{B} = F^+_{LC}\dot{\epsilon^p} \tag{6.12}$$

Following description of the average shear stress in the lattice τ (Eq. 2.6), the shear stress at the head of dislocation pile-up τ_e (Eq. 2.7) and the mean free path of dislocation λ (Eq. 2.8), it is necessary to remind the postulated in Eq. 2.9 criterion of avalanche-like failure of LC locks:

$$\begin{cases} \tau \leq \tau_{min} & \Rightarrow \quad B = B_{cr} \\ B \leq B_{min} & \Rightarrow \quad \tau_e = \tau_{cr} \\ \tau > \tau_{min} \wedge B > B_{min} & \Rightarrow \quad \begin{array}{l} (1 - \frac{B_{min}}{B_{cr}})\frac{\tau_e}{\tau_{cr}} + (1 - \frac{\tau_{min}}{\tau_{cr}})\frac{B}{B_{cr}} - \\ -(1 - \frac{B_{min}}{B_{cr}}) - (1 - \frac{\tau_{min}}{\tau_{cr}})\frac{B_{min}}{B_{cr}} = 0 \end{array} \end{cases} \tag{6.13}$$

In general, one can assume that the interaction between B and τ_e plays a crucial role as a trigger of the serration, but when one of them reaches sufficient value, the other one is negligible for the phenomenon to occur. Practically for the time being, the available experimental data are scarce and do not allow to trace with a sufficient precision the $B - \tau_e$ interaction curve. Thus, the values B_{min},

τ_{min} are introduced in a somewhat arbitrary manner. Both values should be regarded only as auxiliary, as long as the precise profile of interaction curve for a given material is not known. Therefore, when the interaction curve is reached by the density of dislocation groups combined with the shear stress at the head of dislocation pile-up, theoretically, all the LC barriers are broken and the avalanche-like process is triggered. The process of massive failure of LC locks results in an instantaneous increase of plastic strain by the following increment:

$$\Delta\epsilon^p = \frac{B}{F_{LC}^-} \tag{6.14}$$

with F_{LC}^- denoting another function of density of dislocations ρ, temperature T and the level of stress σ, and $\Delta\epsilon^p$ being interpreted as the amount of slip during the catastrophic failure of dislocation barriers. Assuming that the process takes place at a constant value of a total strain and is kinematically controlled, the strain redistribution results in a proportional elastic drop of stress:

$$\Delta\sigma = E\Delta\epsilon^p \tag{6.15}$$

During fast motion of dislocations in the lattice due to the massive failure of LC locks, a substantial quantity of heat is produced. Heat quantity ΔQ is a function of the plastic work W^p and internal friction in the lattice W^f when abrupt slip occurs:

$$\Delta Q = \eta(\Delta W^p + \Delta W^f) \tag{6.16}$$

where η gives the relevant conversion factor. Following the curve of specific heat under constant volume (Fig. 2.6), and assuming that temperature remains above absolute zero, the following temperature increment occurs:

$$\Delta T = \frac{\Delta Q}{mC_V(T)} \tag{6.17}$$

This increase of temperature, illustrated in Fig. 2.4b, may even be of the order of $30K - 50K$. Temperature becomes a driving force in the process of stress relaxation down to a basic level determined by the equilibrium conditions [42].

The process of stress relaxation is described by the following set of equations:

$$\sigma = \sigma_r + \Delta\sigma_T \tag{6.18}$$

$$\frac{d}{dt}(\Delta\sigma_T) = \frac{1}{t_T}[(\sigma_\infty - \sigma_r) - \Delta\sigma_T] \tag{6.19}$$

with σ_r and σ_∞ denoting respectively: the stress level after the catastrophic slip and the asymptotic strain rate sensitivity (stress level after the transients have died out). The t_T denotes the characteristic time. Temperature relaxes towards a new steady state value inducing an additional evolution of stress $\Delta\sigma_T$. After the process of stress relaxation has been completed, another dynamic strain aging cycle begins.

The first two stages of the process reflect elastic-plastic loading under nearly isothermal conditions, corresponding to low excitation of the lattice. Under these circumstances (no thermal activation) the rate-independent plasticity can be applied, at least until the catastrophic failure of LC locks. Thus, the yield surface f_y has the form:

$$f_y(\underline{\underline{\sigma}}, \underline{\underline{X}}, R_H) = J_2(\underline{\underline{\sigma}} - \underline{\underline{X}}) - \sigma_p - R_H \tag{6.20}$$

$$J_2(\underline{\underline{\sigma}} - \underline{\underline{X}}) = \sqrt{\frac{3}{2}(\underline{\underline{s}} - \underline{\underline{X}}) : (\underline{\underline{s}} - \underline{\underline{X}})} \tag{6.21}$$

where J_2 is the second invariant of the stress tensor. Here, $\underline{\underline{s}}$, $\underline{\underline{X}}$ denote the deviatoric stress and the back stress tensors, respectively whereas σ_p, R_H are the yield stress and the isotropic hardening variable, respectively. Furthermore, it is assumed that the continuum containing LC locks obeys the associated flow rule:

$$\dot{\underline{\underline{\epsilon}}}^p = \dot{\Lambda}\frac{\delta f_y}{\delta \underline{\underline{\sigma}}} \tag{6.22}$$

with the yield function postulated as the potential of plasticity. The hardening model is represented by the following equations:

$$d\underline{\underline{X}} = \frac{2}{3}C_X d\underline{\underline{\epsilon}}^p \tag{6.23}$$

$$dR_H = C_R dp \tag{6.24}$$

where C_X, C_R denote the kinematic and the isotropic hardening moduli, respec-

tively. The evolution of parameter B can be computed from Eq. 2.2, in the following way (Eq. 2.10):

$$dB = F^{+}_{LC}(\rho, T, \underline{\sigma})dp \tag{6.25}$$

It is assumed that in every "cycle" of loading/unloading (seen as single tooth in the stress-strain curve), parameter B is accumulated from 0 as long as the condition expressed by Eq. 6.13 is fulfilled and the plastic flow instability (drop of stress) takes place.

6.2. Numerical Algorithm

Model calibration (i.e. identification of the parameters) and a quantitative analysis can be performed using the proposed incremental algorithm, which is tested for uniaxial stress state. The DPF phenomenon is followed step-by-step along the (serrated) stress-strain curve and, eventually, implemented in a FEM code.

Numerical algorithm consists of five basic blocks (A-E), with the exception of one split into two sub-blocks (D_I and D_{II}), which are activated according to recognized phase of the deformation process (Fig. 6.1). It is shown that a total deformation related to single phenomenon occurrence, denoted as ϵ^{slip}, consists of a part proportional to the serration drop of stress ϵ^{p} and a part which covers the material softening ϵ^{s}:

$$tg\alpha = \frac{\Delta\sigma}{\Delta\epsilon^{s}} = -H_s \tag{6.26}$$

$$\Delta\epsilon^{s} = -\frac{\Delta\sigma}{H_s} \tag{6.27}$$

$$\Delta\epsilon^{p} = \frac{B}{F^{-}_{LC}} \tag{6.28}$$

$$\Delta\epsilon^{slip} = \Delta\epsilon^{s} + \Delta\epsilon^{p} \tag{6.29}$$

Such approach is slightly different than the one recently published [106], also in terms of temperature modeling. Nevertheless, the process is strain-controlled, i.e. for a set of internal functions and state variables given at the step k, new values are determined at the step $k+1$ following predefined increment of the

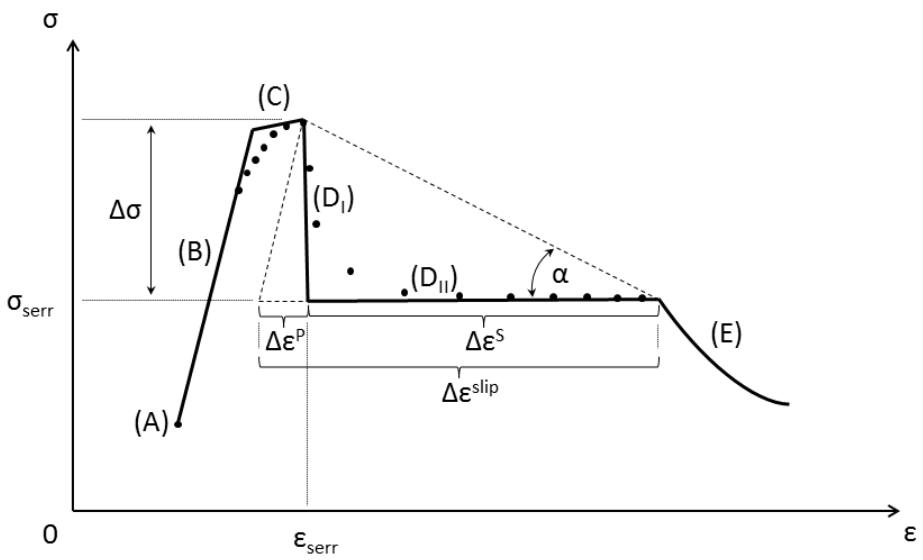

Figure 6.1.: Schematic illustration showing phases of the serration process: initial state (A), elastic deformation (B), plastic deformation (C), drop of stress (D_I), jump of strain (D_{II}) and relaxation (E).

total strain. Calculation of the stress increment and the temperature changes is fundamental for future implementation in a FEM code.

6.2.1. Initial State (A)

The algorithm begins with the initial values of the variables and state functions as well as the state of zero strain and stress in the sample. The density of the Lomer-Cottrell locks is set to zero, and the initial values are set for the density of

$k = 0$	$B_k = 0$
$\epsilon_k = 0$	$\sigma_k = 0$
$\epsilon^p = 0$	$\tau_k = \tau_{min}$
$\rho_k = \rho_0$	$T_k = T_0$
$\epsilon^p_{LC} = (\epsilon^p_{LC})_0$	$(\Delta\epsilon^p_{LC})_k = (\Delta\epsilon^p_{LC})_0$

Table 6.1.: Numerical model: initial state.

dislocations as well as for the yield stress and the shear stress. The accumulated plastic strain is equal to zero and the threshold of the plastic strain for the onset of the LC locks evolution is assumed. Temperature level corresponds to the temperature of surrounding environment (e.g. helium bath).

6.2.2. Elastic Deformation (B)

The first part of deformation process obeys the elastic regime and the increment is repeated until the yield point is reached by the stress value. Elastic deformation does not influence changes of temperature, density of dislocations or density of the LC locks.

IF	$\sigma_k < \sigma_p$	yield condition check
THEN	$\epsilon_{k+1} = \epsilon_k + \Delta\epsilon_0$	
	$\sigma_{k+1} = \sigma_k + E\Delta\epsilon_0$	
	$(\Delta\epsilon^p_{LC})_{k+1} = (\Delta\epsilon^p_{LC})_k$	
	$B_{k+1} = B_k$ $\quad$ $\tau_{k+1} = \tau_k$	
	$\rho_{k+1} = \rho_k$ $\quad$ $T_{k+1} = T_0$	
	$k \leftarrow k + 1$	and repeat **B**
ELSE	$\sigma_k = \sigma_p$	continue at **C**

Table 6.2.: Numerical model: elastic deformation.

6.2.3. Plastic Deformation (C)

The plastic deformation process starts beyond the elastic limit. At the beginning of this step the serration criterion is checked. If the interaction curve has not been reached, the continuous plastic deformation takes place.

Due to linear hardening assumed, the stress increment is governed by the hardening modulus. The plastic strain increment is determined via subtraction of the elastic strain from the total strain. Then the threshold for the LC locks evolution is tested and, if exceeded, a new value of their density is calculated. Moreover, an updated dislocation density and the corresponding shear stress in

the lattice are determined with the use of relations given above. This makes it possible to update the free path of dislocations as well as the shear stress at the head of dislocation pile-up. It is assumed, that this process does not cause any temperature rise. It is repeated until the interaction curve is reached, then the serration phase is triggered.

	$\tau_e = \tau_{min}$	
IF	$(1-\frac{B_{min}}{B_{cr}})\frac{\tau_e}{\tau_{cr}} + (1-\frac{\tau_{min}}{\tau_{cr}})\frac{B_k}{B_{cr}} - (1-\frac{B_{min}}{B_{cr}}) - (1-\frac{\tau_{min}}{\tau_{cr}})\frac{B_{min}}{B_{cr}} = 0$	serration criterion
THEN	$\epsilon_{k+1} = \epsilon_k + \Delta\epsilon \qquad \sigma_{k+1} = \sigma_k + E_p\Delta\epsilon$	linear hardening
	$\Delta\epsilon^p = \Delta\epsilon(1-\frac{E_p}{E}) \qquad \epsilon^p = \epsilon^p + \Delta\epsilon^p$	
	IF $\epsilon^p > \epsilon^p_{LC}$ THEN	the LC locks criterion
	$F^+_{LC} = k_4\sqrt{\rho_k}$	
	$B_{k+1} = B_k + F^+_{LC}(\epsilon^p - \epsilon^p_{LC})$	
	$\Delta\rho = \Delta\epsilon M(\frac{1}{db} + k_1\frac{\sqrt{\rho_k}}{b} - k_3\rho_k)$	
	$\rho_{k+1} = \rho_k + \Delta\rho$	
	$\tau = \tau_f + \alpha\mu b\sqrt{\rho_{k+1}}$	
	$\lambda = \frac{1}{\frac{1}{d}+k_1\sqrt{\rho_{k+1}}+k_2\sqrt{B_{k+1}}}$	
	$\tau_e = \frac{\pi(1-\nu)}{\mu b}\lambda\tau^2$	
	IF $B_{k+1} > B_{cr}$ THEN $B_{k+1} = B_{cr}$	
	$(\Delta\epsilon^p_{LC})_{k+1} = (\Delta\epsilon^p_{LC})_k \qquad T_{k+1} = T_k$	
	$k \leftarrow k+1$	and repeat **C**
ELSE	$B_{k+1} = B_k \qquad \tau_{k+1} = \tau_k \qquad \rho_{k+1} = \rho_k$	continue at **D'**

Table 6.3.: Numerical model: plastic deformation.

6.2.4. Serration - Drop of Stress (D_I)

Following the collapse of the LC locks, which triggers the serration phase of discontinuous plastic flow, sudden motion of dislocations causes the increment of permanent strain. Hence, from the macroscopic point of view the mechanism of strain "jump", different than in the classical continuous plastic flow, is reflected

by an increment of the irreversible plastic strain. Since the total value of strain remains constant in this phase, the increment of plastic part is equivalent to decrement of the elastic one and results in a drop of the stress value. The LC locks vanish after their collective collapse, so their density is set back to zero. The plastic strain threshold, representing the subsequent onset of LC locks evolution, is updated to stay above the present level of the accumulated plastic strain.

$F_{LC}^{-} = F_{LC}^{+} \cdot h$	$h = 800$	
$\Delta\epsilon^p = \frac{B_k}{F_{LC}^{-}}$	$B_{k+1} = 0$	the LC locks vanish
$\epsilon^p = \epsilon^p + \Delta\epsilon^p$	$\epsilon_{LC}^p = (\Delta\epsilon_{LC}^p)_{k+1} + \epsilon^p$	
$\rho_{k+1} = \rho_k$	$\epsilon_{k+1} = \epsilon_k$	
$\Delta\sigma = E\Delta\epsilon^p$	$\sigma_{k+1} = \sigma_k - \Delta\sigma$	
$\epsilon_{serr} = \epsilon_k$	$\sigma_{serr} = \sigma_k$	
$T_{k+1} = T_k$	$\tau_{k+1} = \tau_k$	
$k \leftarrow k + 1$		continue at **D”**

Table 6.4.: Numerical model: serration - drop of stress.

6.2.5. Serration - Jump of Strain (D_{II})

It is assumed that massive motion of dislocations, released during previous phase due to vanishing LC locks, results in fast plastic deformation (slip) within the affected area. Increase of strain stays in relation with the stress drop by means

$\Delta\epsilon^s = \frac{-\Delta\sigma}{H_s}$	$\epsilon_{k+1} = \epsilon_k + \Delta\epsilon^s$	effect of intermediate slip
$\rho_{k+1} = \rho_k$	$\sigma_{k+1} = \sigma_k$	
$B_{k+1} = B_k$	$\tau_{k+1} = \tau_k$	
$T_{k+1} = T_k + \eta\Delta\epsilon^p \frac{(\sigma_{k-1}+\sigma_k)}{2\rho_m c_V(T_k)}$		
$k \leftarrow k + 1$		continue at **E**

Table 6.5.: Numerical model: serration - jump of strain.

of a material softening parameter H_s. Moreover, dynamic plastic deformation generates such amount of heat, which cannot be easily dispersed, and results in local rise of temperature. The process may have thermally activated nature, associated with lattice excitation resulting from heat dissipation equivalent to dissipated plastic power.

6.2.6. Relaxation (E)

The stress relaxation phase takes place just after the serration steps were completed. The initial value of stress increment for integration of the hyperbolic function corresponds to the drop of stress computed at the serration step. Simultaneously, the shear stress and the temperature are systemically decreasing to reach the basic values. The iterations are repeated until the stress value reaches an asymptotic level. Thereafter, the yield point is updated and the process is repeated starting from the elastic deformation.

	$\sigma_\infty = (0.91 - 0.2\epsilon_{serr}) \cdot \sigma_{k+1}$	asymptotic level
IF	$\sigma_k > 1.05 \cdot \sigma_\infty$	reaching the asymptotic level
THEN	$\Delta\sigma = \frac{\sigma_\infty - \sigma_k - \Delta\sigma}{t_\phi}$	evolution of stress decrement
	$\epsilon_{k+1} = \epsilon_k + \Delta\epsilon \qquad \sigma_{k+1} = \sigma_k + \Delta\sigma$	
	$B_{k+1} = B_k \qquad \rho_{k+1} = \rho_k$	
	IF $\quad \tau_k > \tau_{min} \quad$ THEN	
	$\Delta\tau = \frac{\tau_k - \tau_{min}}{0.2 \cdot t_\phi} \qquad \tau_{k+1} = \tau_k - \Delta\tau$	
	IF $\quad T_k > T_0 \quad$ THEN	
	$T_{k+1} = T_k - \frac{x_{vc}\Delta\epsilon\lambda(T_k))}{\rho_m c_V(T_k)}(T_k - T_0)$	
	$(\Delta\epsilon^p_{LC})_{k+1} = (\Delta\epsilon^p_{LC})_k$	
	$k \leftarrow k + 1$	and repeat **E**
ELSE	$\sigma_p = \frac{E_p E}{E - E_p}(\epsilon_k - \epsilon_{serr}) - \sigma_k \frac{E_p}{E - E_p} + \sigma_{serr} \frac{E}{E - E_p}$	update yield point and continue at **B**

Table 6.6.: Numerical model: relaxation.

6.3. Parameters

For the numerical analysis a series of material constants as well as initial values of the parameters were adopted. Only some of them were identified by means of the experiment (e.g. elasticity modulus, yield point, initial plastic strain threshold for evolution of the LC locks, mean grain size). A number of parameters were obtained by means of data tables available in the literature [107] (e.g. initial density of dislocations as for SA state, length of the Burgers vector, coefficients k_i, etc.). Some free parameters were selected in order to tune the numerical model so as to stay as close to the measured stress-strain curve as possible (e.g. magnitude of the stress drop due to serration, increasing frequency of serrations, increasing yield point, coefficient of material softening). Concerning the functions used in the equations for temperature [108], the c_V and λ were calculated as follows ($x = c_V$ or $x = \lambda$):

$$\log(x) = a + b\log(T) + c(\log(T))^2 + d(\log(T))^3 + e(\log(T))^4 + \\ + f(\log(T))^5 + g(\log(T))^6 + h(\log(T))^7 + i(\log(T))^8 \tag{6.30}$$

where the coefficients $a - i$ are presented in Table 6.7.

Coefficient	c_V	λ
a	22.0061	-1.4087
b	-127.5528	1.3982
c	303.6470	0.2543
d	-381.0098	-0.6260
e	274.0328	0.2334
f	-112.9212	0.4256
g	24.7593	-0.4658
h	-2.239153	0.1650
i	0	-0.0199
Data range	3 K - 300 K	3 K - 300 K

Table 6.7.: Coefficients used in equation for the c_V and λ [108].

Parameter	Unit	Value	
		316LN	**JK2LB**
E	Pa	$2.0 \cdot 10^{11}$	$2.0 \cdot 10^{11}$
E_p	Pa	$6.4 \cdot 10^{8}$	$2.4 \cdot 10^{8}$
H_s	Pa	$-5 \cdot 10^{9}$	$-10 \cdot 10^{9}$
ν	-	0.3	
μ	Pa	$E/[2(1+\nu)]$	
σ_p	Pa	$12.8 \cdot 10^{8}$	$15.6 \cdot 10^{8}$
d	m	$5 \cdot 10^{-5}$	$6 \cdot 10^{-5}$
ρ_0	m^{-2}	$3.0 \cdot 10^{13}$	
ρ_m	kg/m^3	7860	
M	-	3.0	
h	-	800	
α	-	0.4	
b	m	$2.58 \cdot 10^{-10}$	
k_1	-	0.031	
k_2	-	0.02	
k_3	-	0.01	
τ_f	Pa	σ_p/M	
B_{min}	m^{-2}	0	
τ_{min}	Pa	$\tau_f + \mu\alpha b\sqrt{\rho_0}$	
B_{cr}	m^{-2}	$8 \cdot 10^{13}$	$11 \cdot 10^{13}$
τ_{cr}	Pa	$450\tau_f$	$750\tau_f$
t_ϕ	-	250	350
$(\epsilon^p_{LC})_0$	-	$8\sigma_p/E$	$6\sigma_p/E$
$\Delta\epsilon^p_{LC}$	-	$0.01(\epsilon^p_{LC})_0$	
a	m	0.003	
$\dot{\epsilon}$	-	$2.0 \cdot 10^{-3}$	
x_{vc}	m^{-2}	$4/(a^2)\dot{\epsilon}$	

Table 6.8.: Parameters of 316LN and JK2LB used in numerical algorithm.

Final calibration of the numerical model was based upon results of many experimental campaigns, filled with metallurgical observations and cryogenic tensile tests of materials [96, 97, 98, 102, 103, 104, 105]. The set of parameters adopted for the numerical analysis is presented in Table 6.8.

The threshold variation has been applied in order to model the experimentally observed increase of serrations density in the course of deformation. An update of the yield point has been performed in order to reflect the experimentally observed return on the 'uniform' hardening curve after the drop of stress, the relaxation phase and the elastic reloading.

In addition, two important serration parameters were assumed: F_{LC}^{+} and F_{LC}^{-}. At present, the influence of temperature and stress level on these functions is neglected. Hence, the results may be treated as for a given temperature value (stable temperature before the energy dissipation due to massive motion of dislocations in the lattice).

7. Numerical Results

This chapter introduces numerical results obtained through the constitutive model implemented in Maple[1] software. The simulations were carried out for 316LN and JK2LB grades, tested at 4.2 K in the form of cold worked products.

The chapter starts with simulation curves of tensile tests with the emphasis on DPF phenomenon details. Moreover, separate graphs for shear stress, density of dislocations and number of LC locks in the material lattice are presented. Also, detail views representing behavior during single serration are shown. Results are split in two groups, distinguished by grade type: 316LN and JK2LB.

Finally, a comparison of results between laboratory tests of cold worked grades and corresponding numerical simulations is provided as an introduction to the general discussion.

7.1. Simulation Curves

The curves presented below are obtained by applying algorithm of numerical model[2] developed in Maple software. These graphs present simulation of material behavior during tensile tests. The stress-strain representation is directly associated with the corresponding curves obtained in the course of experiments (Section 5.2). For both grades (316LN, JK2LB) the following data are provided:

- representative stress-strain curves,
- detailed view of single DPF occurrence,
- representation of parameters: τ, B and ρ as a function of ϵ,
- detailed view of above mentioned parameters for single DPF occurrence.

[1]Maple is a computer algebra system developed and sold commercially by Maplesoft, a software company based in Waterloo, Ontario, Canada

[2]Maple algorithm (execution group) is presented in Appendix A.1, the set of parameters for 316LN is given in Appendix A.2, and for JK2LB in Appendix A.3

Data recording has been resolved in steps of progressing strain, not in time sampling as was for laboratory tests. The sampling rate $\Delta\epsilon$ for all numerical analysis here-presented is set to $2.5 \cdot 10^{-5}$. The stress-strain graphs show stress σ in MPa on y-axis (left), strain ϵ in % on x-axis and temperature T in K on y-axis (right). The graphs show shear stress τ in MPa on y-axis (left) and number of LC locks B together with density of dislocations ρ both in m^{-2} on y-axis (right, values x10^{12}) as a function of strain ϵ in % (x-axis). Based on curves of experimental results limited in strain axes (due to extensometry limitations), only 25 % of strain as the most interesting part of the numerical curves is shown. It neither means the end of the test nor the fracture of the specimen. This limitation is also justified by the small strains theory applied in the constitutive modeling and numerical implementation.

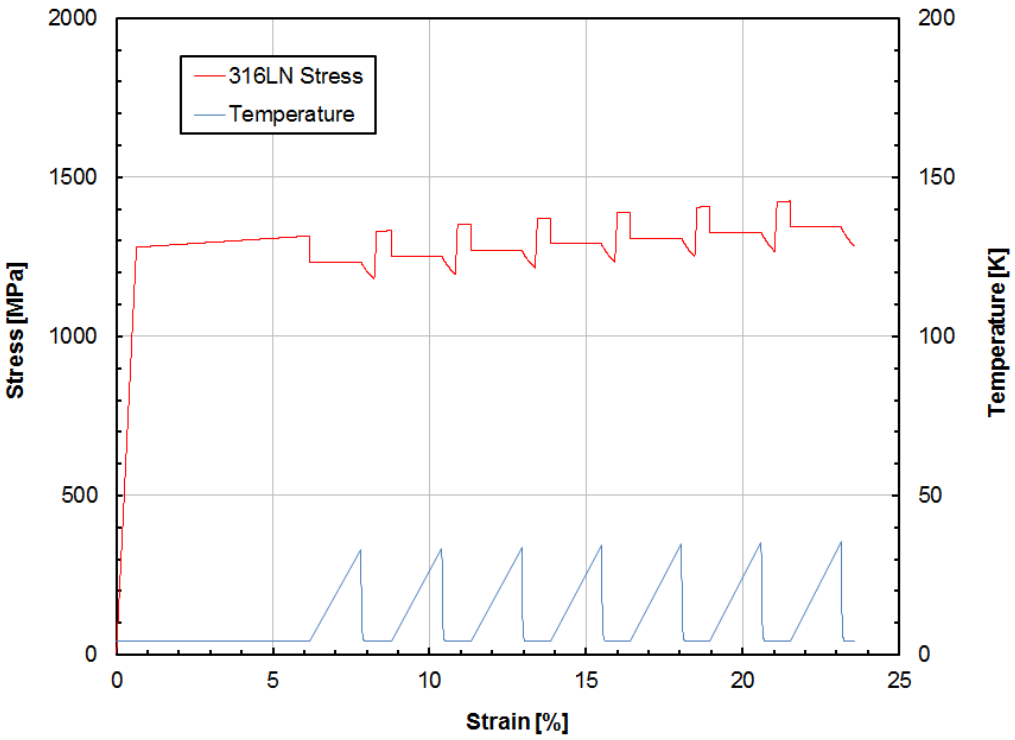

Figure 7.1.: Simulated stress-strain curve (red) with temperature (blue) for cold worked 316LN at 4.2 K: stress σ in MPa on y-axis (left), strain ϵ in % on x-axis and temperature T in K on y-axis (right).

7.1.1. Grade 316LN

The graph shown in Fig. 7.1 represents simulated stress-strain curves of cold worked 316LN grade at the temperature of 4.2 K. The most visible differences in the appearance/shape of curves between this result and the experimental one are mainly the sharp edges of transitions between the steps (e.g. from elastic phase to plastic phase). Numerical results show curves with an ideal elastic deformation step, followed by plastic deformation step - seen as a plateau. Experimental results, on the other hand, show that in reality the two steps are mixed, so one can see flattened elastic part just rounded in the horizontal direction at the end.

The DPF single cycle, which was previously shown in details of laboratory test for cold worked 316LN at 4.2 K (see Section 5.2.3), is presented in the same range of stress and strain (see Fig. 7.2). Analysis and comparison can be made on single occurrence of DPF, extracted from simulated curve. Similarly to

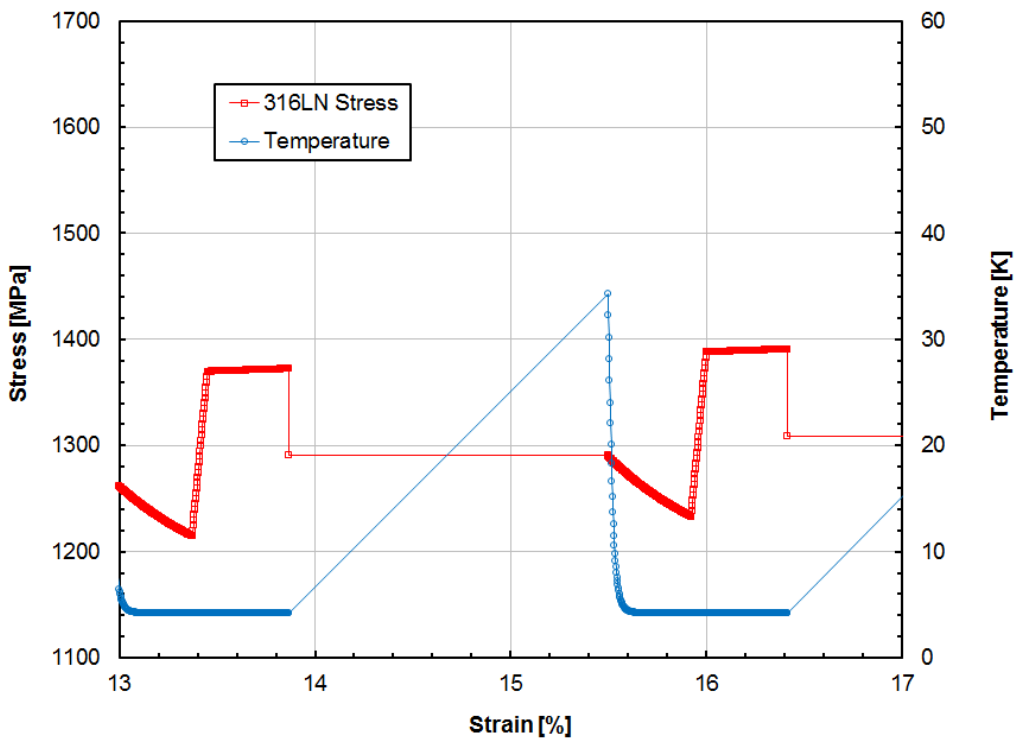

Figure 7.2.: Extracted part of simulated stress-strain curve (red) with temperature (blue) for cold worked 316LN at 4.2 K (shows detailed view of single DPF occurrence).

experiment, the elastic deformation part can be easily identified on the portion of the curve where the stress is sharply climbing up. Just after, when the material reaches the plastic deformation zone, sudden drop of load is observed with the following deformation step (plastic slip). These two steps of DPF phenomenon are shown with single point representation, regardless of strain sampling rate. This is due to the fact, that both processes are characterized by very high velocity and take place within micro-seconds. Thus, in order to numerically reflect these effects, special constraints were imposed on drop of stress and jump of strain (macroscopic slip). Both effects are justified by the physics of serrated yielding, consisting in avalanche-like crossing of lattice barriers by dislocations accumulated in pile-ups. Finally, the relaxation part can be seen as mild drop of stress with the accompanying rise of strain.

Additionally, the numerically calculated temperature is correlated with the

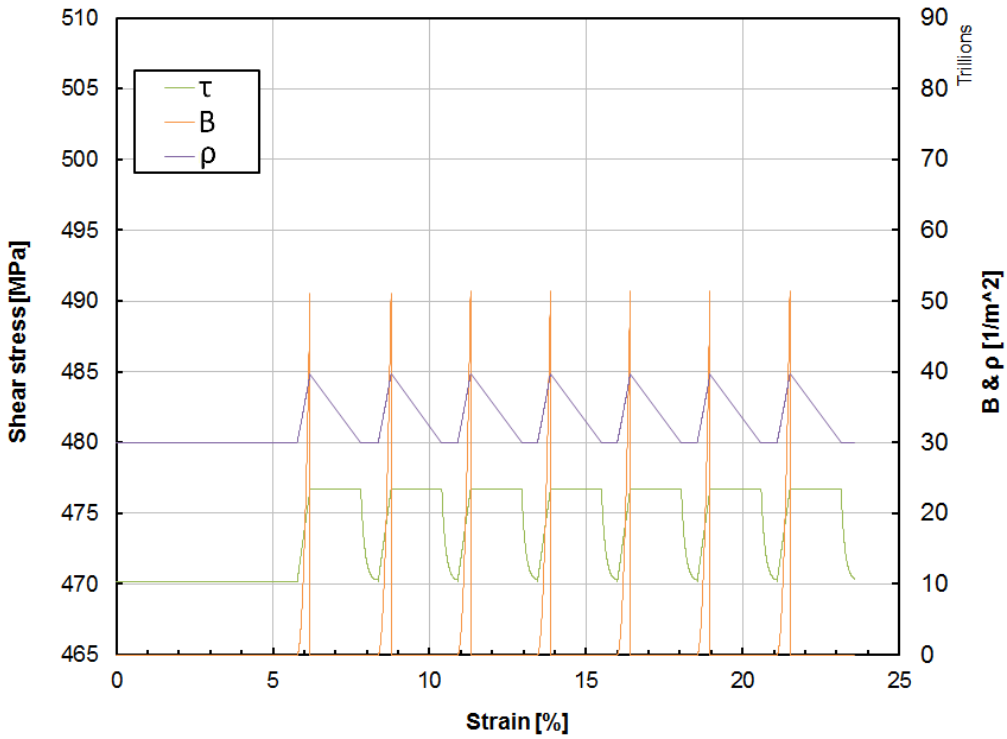

Figure 7.3.: Numerical solution for cold worked 316LN: shear stress τ (green line) in MPa on y-axis (left) and number of LC locks B (orange line) with density of dislocations ρ (purple line) both in m^{-2} on y-axis (right, values x10^{12}) as a function of strain ϵ in % (x-axis).

stress-strain line of the CW 316LN. Differently from experimental results, the peak of temperature rise is located at the end of serration step, just before the relaxation part. Beside this area, the temperature remains stable within the elastic and the plastic deformation.

It is important to notice that the temperature rise in the numerical approach starts at the point of sudden drop of stress and it is progressing during the so-called jump of strain (macroscopic slip). Contrary to dependance of the probe mounting point on the laboratory test, the simulation gives overall calculation based on the specific heat c_V and the thermal diffusivity λ of the material.

The stress-strain graph and the extracted single serration are analyzed closer by plotting shear stress τ, number of LC locks B, and density of dislocations ρ as a function of strain ϵ. Each parameter, represented by dedicated curve, is shown in Fig. 7.3 for complete numerical result, and in Fig. 7.4 for single serration.

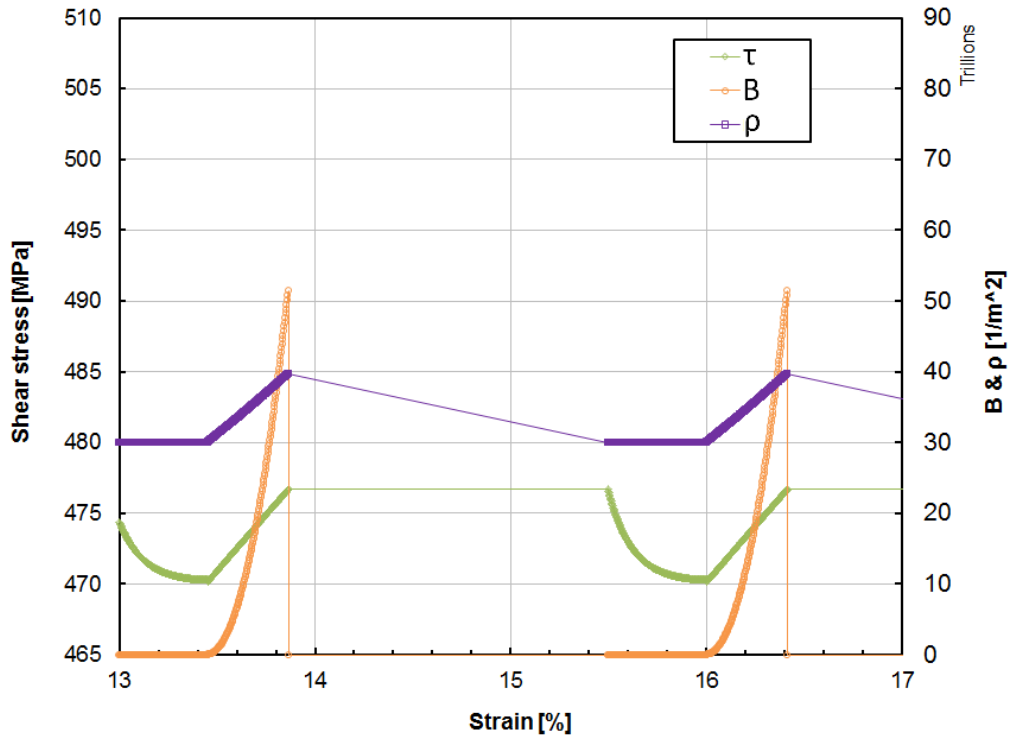

Figure 7.4.: Extracted part of parameters graph for cold worked 316LN grade showing detailed view of parameters behavior corresponding to single DPF occurrence. Color code: green line for shear stress, orange line for number of LC locks, and purple line for density of dislocations.

During the plastic deformation phase of 316LN, one can observe increase of all three parameters up to the limit dictated by starting serration. The phenomenon starts with vanishing LC locks which corresponds to drop of load. Following the release of dislocations, their number is systemically decreasing during dynamic deformation (jump of strain). Last changing is the shear stress, acting as a reaction of dispersed dislocations during the relaxation phase.

Due to high strain increment $\Delta\epsilon$, one can appreciate point representation of test data similar to that of experiment. Taking into account flexibility of numerical analysis, the simulation can be repetitively made with different $\Delta\epsilon$ to ensure best fit (obviously, not influencing the shape of curve).

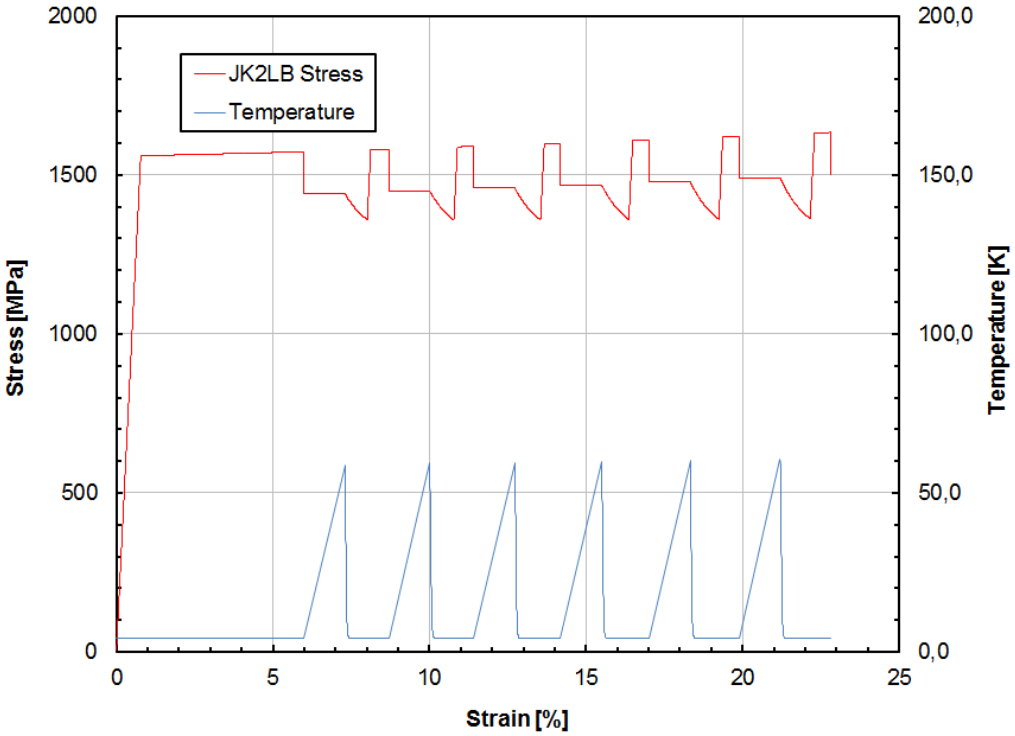

Figure 7.5.: Simulated stress-strain curve (red) with temperature (blue) for cold worked JK2LB at 4.2 K: stress σ in MPa on y-axis (left), strain ϵ in % on x-axis and temperature T in K on y-axis (right).

7.1.2. Grade JK2LB

The graph shown in Fig. 7.5 indicates simulated stress-strain curves of cold worked JK2LB grade at the temperature of 4.2 K. As before, for numerical results of the 316LN, one can see sharp edges of transitions between the steps with single point representation. Similarity comes from the fact of using the same numerical model, now calibrated for JK2LB.

Once again the DPF single serration curve, this time for cold worked JK2LB at 4.2 K, is shown in the same range of stress and strain (see Fig. 7.6) compared to experimental results (see Section 5.2.3). One can notice all the corresponding steps described before for the numerical results of 316LN. The difference between the two grades in representation of DPF is clearly the range of strain and the amplitude of stress, which is characteristic of certain materials and within the numerical model comes from proper calibration.

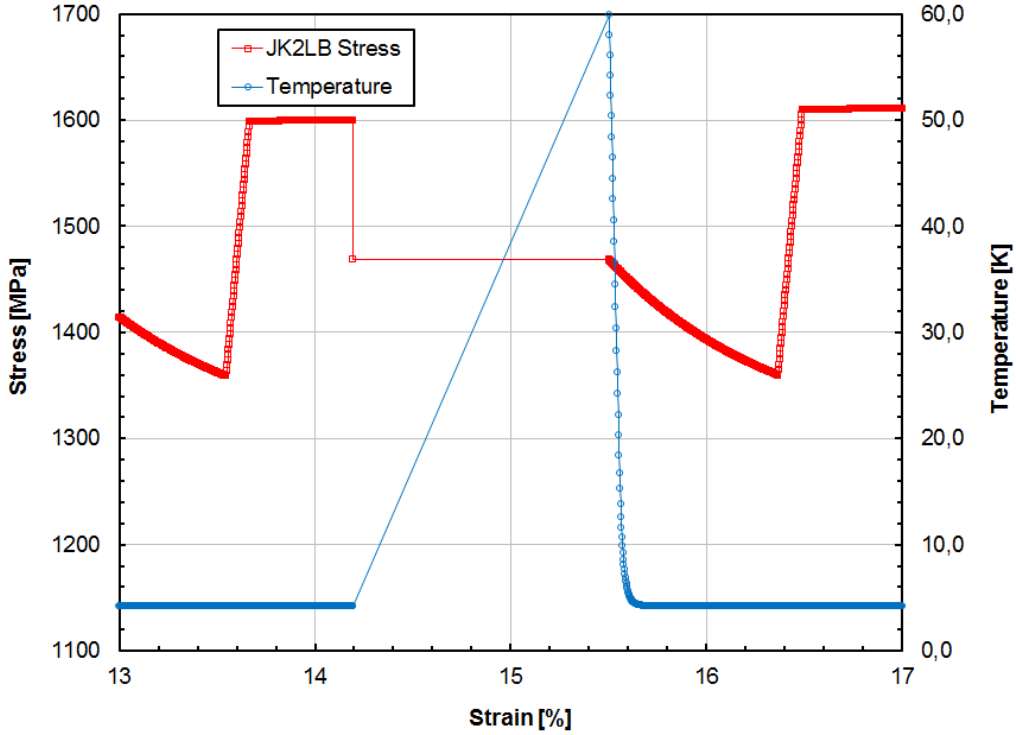

Figure 7.6.: Extracted part of simulated stress-strain curve (red) with temperature (blue) for cold worked JK2LB at 4.2 K (shows detailed view of single DPF occurrence).

The numerically calculated temperature is correlated, like it was for 316LN, with the stress-strain cure of JK2LB. Relation between the temperature plot and the stress-strain curve is similar to the one of 316LN. Taking into account that numerical calculations are not influenced by the probe mounting, one can see representative temperature rise which corresponds in its magnitude to the scale of the DPF occurrence (higher/larger for JK2LB than for 316LN).

The stress-strain graph and the extracted part of single serration, again for JK2LB as it was for 316LN, is analyzed by presenting shear stress τ, number of LC locks B, and density of dislocations ρ as a function of strain ϵ. Each parameter, represented by dedicated curve, is shown in Fig. 7.7 as for complete numerical result and in Fig. 7.8 as for single serration. The same color code, as for 316LN, has been preserved. General explanation of curves, which was given for the previous grade, applies here as well.

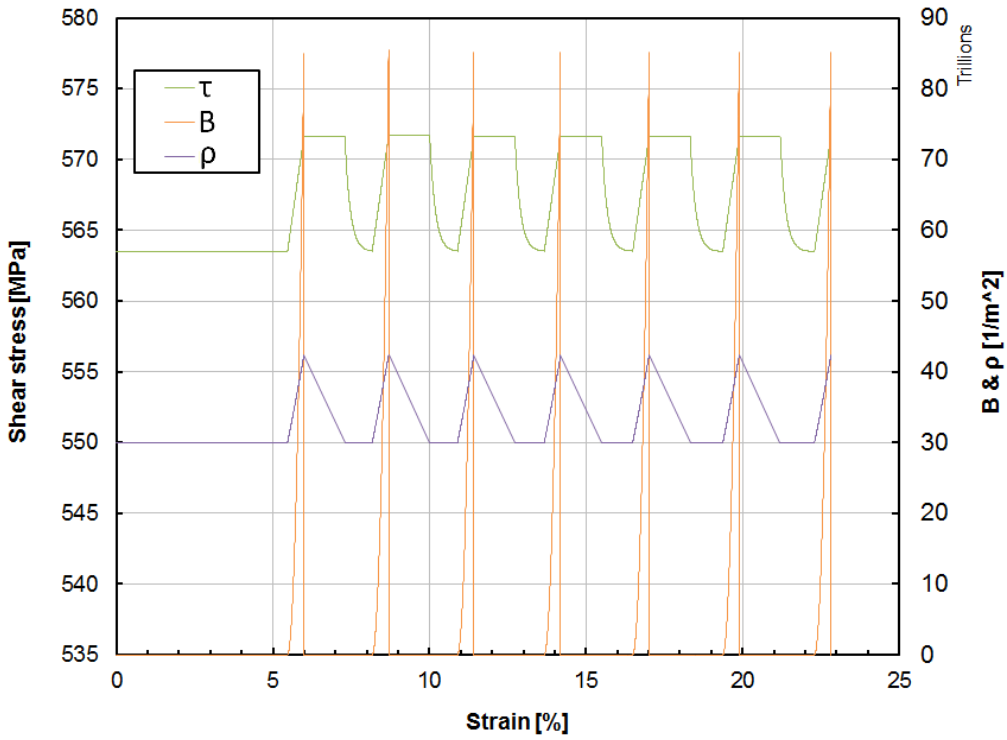

Figure 7.7.: Numerical solution for cold worked JK2LB: shear stress τ (green line) in MPa on y-axis (left) and number of LC locks B (orange line) with density of dislocations ρ (purple line) both in m^{-2} on y-axis (right, values $x10^{12}$) as a function of strain ϵ in % (x-axis).

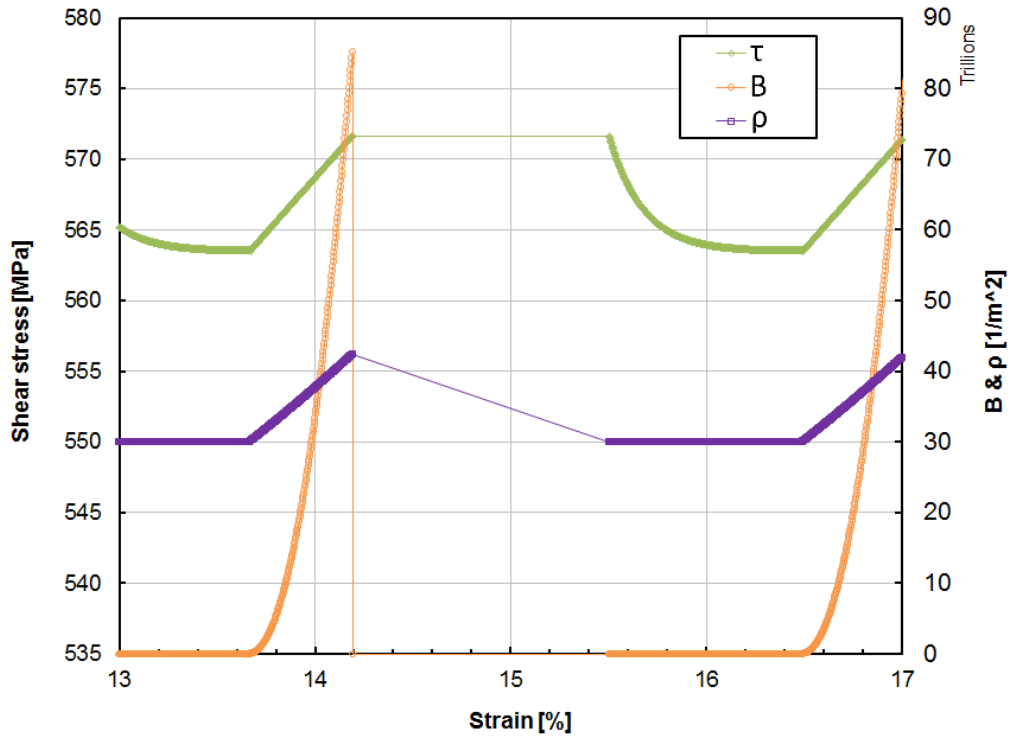

Figure 7.8.: Extracted part of parameters graph for cold worked JK2LB grade showing detailed view of parameters behavior corresponding to single DPF occurrence. Color code: green line for shear stress, orange line for number of LC locks, and purple line for density of dislocations.

7.2. Data Comparison

Numerical results and these obtained from the laboratory tests are compared with each other. The stress extracted from experiments is measured by means of the Piola-Kirchhoff measure (engineering stress). The same definition of stress is used in the numerical model. Similarly, the strains are measured by using the linear (Cauchy) approach, which is expressed as the ratio of elongation to the initial value of the specimen gauge length. The same measure is applied in the numerical study. The Cauchy strain measure is considered justified due to the investigated range of the strain which is focused around 0.15 (for all cases).

The experimental results used for comparison (both for 316LN and JK2LB stainless steels), to which this chapter refers, were obtained in helium bath at the temperature of 4.2 K. This temperature level was used as reference for all numerical calculations. The stress was measured by means of the internal and

the external load cells, as described in Section 4.3.3. As the internal load cell was located in direct proximity of the sample, the stress values measured by using this cell are much more precise when compared to the data obtained by means of the external load cell. Therefore, the ones arising from the signal of the internal load cell were presented and compared to numerical simulation. In some cases, the loading/unloading cycles have been performed in order to verify the elastic modulus.

Comparison of the serrated yielding process (stress-strain curves) and evolution of temperature is shown in Fig. 7.9a for experimental, and in Fig. 7.9c for numerical results. Numerical results show curves with an ideal elastic step, followed by plastic flow - in the form of a plateau. Experimental results, on the other hand, show rather nonlinear behavior, so one can see flattened part just rounded in horizontal direction at the end. The details of single serration are presented in Fig. 7.9b and Fig. 7.9d, where the drop of stress, the jump of strain, the stress relaxation phase and the reloading phases are identified together with sudden increase of temperature, followed by a thermal stabilization down to the temperature of He bath (4.2 K). All figures show similarity between experimental and numerical results. Many authors have interpreted the onset of serrated yielding as purely thermodynamic phenomenon, triggered by sudden increase of temperature, which is now proved to be a source of misunderstanding. The measurements carried out by using the internal load cell clearly show that the drop of stress precedes the increase of temperature, and the thermodynamic response is secondary with respect to the mechanical effect.

Despite the fact that the stress-strain curves of both grades slightly differ from each other, it can be easily observed that there is a significant difference between the scales of DPF phenomenon. Full curves and single details for 316LN and JK2LB are analyzed in Fig. 7.9e-h. Additional curves resulting from modeling (non-measured), with values such as dislocation density, density of the LC locks as well as average shear stress are indicated in Fig. 7.9e-h. Similar convention has been used as before where the complete curves are shown on the left, and the same functions are plotted for single serrations on right (with magnified scales). While maintaining similar scale, attention is brought to similarity of corresponding curves as well as to the fact, that algorithm describes various materials through calibration of parameters.

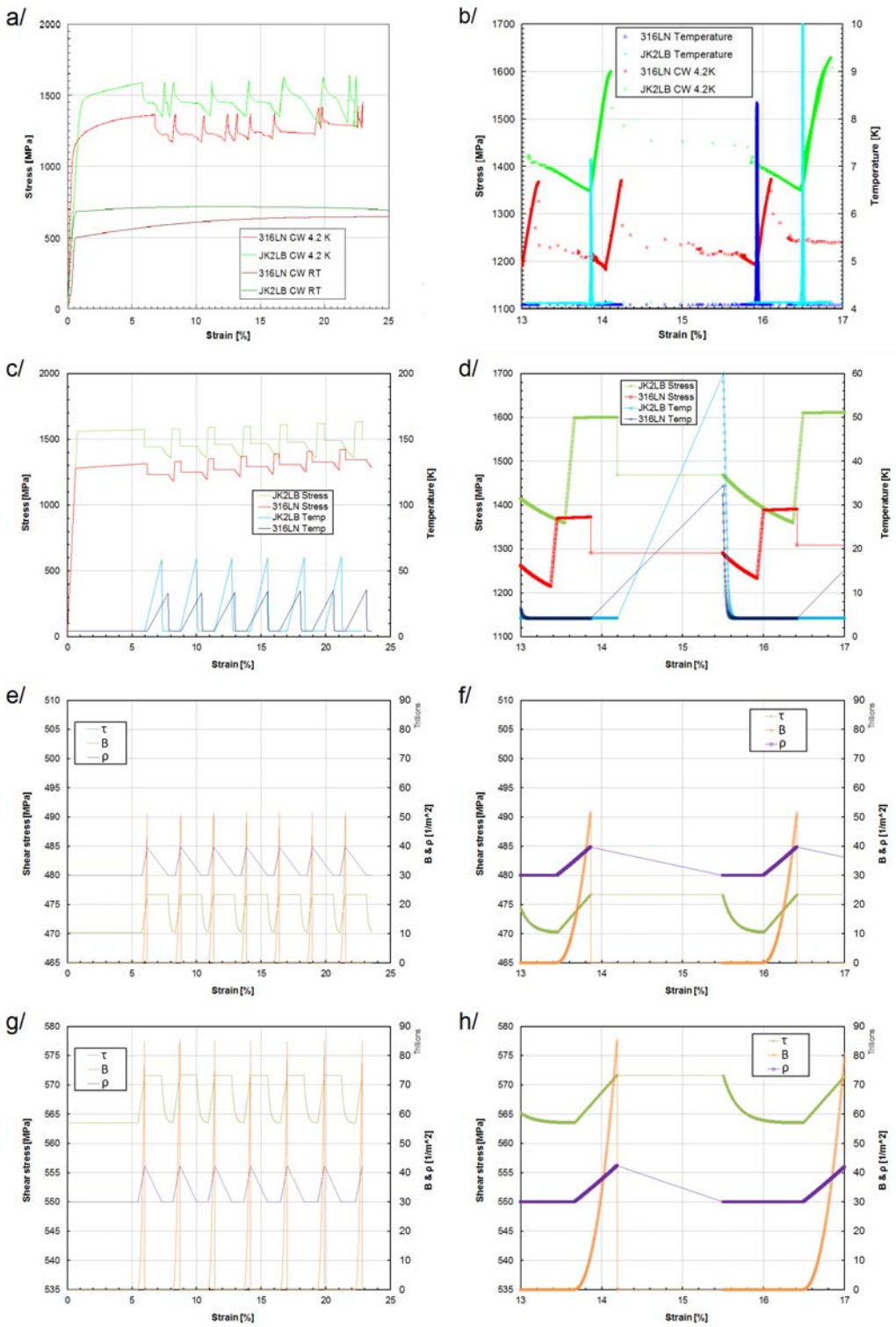

Figure 7.9.: Comparison of experimental and numerical results: a/ full experimental, b/ detailed experimental, c/ full numerical, d/ detailed numerical, e/ 316LN full parameters, f/ 316LN detailed parameters, g/ JK2LB full parameters, h/ JK2LB detailed parameters.

The calculated results prove that the model may be refined in order to correctly interpret the experimental observations. It seems, that number of collected experimental data is already sufficient to provide necessary knowledge for calibration of the numerical model. The model, consequently, generates results which are consistent with the reality. Already at this stage it is possible to extend the application of this model on wider base of steels, if only basic set of parameters is available.

However, more experiments are needed to build more precise description with the internal functions dependent on stress and temperature, and not only on the dislocations density. Also, a confirmation of the assumed material constants is required. To make the calculated results still closer to the experimental trends in the stress-strain curve, a non-linear hardening model should be applied. Moreover, an extension of the formulation to the complex stress states and non-proportional loading paths requires additional, rather sophisticated, experiments to tune the model.

Similar conclusion is drawn in Benallal et al. [109], that the numerical results are usually able to reproduce most of the experimentally observed phenomena with a reasonable accuracy. However, if the model is used to study the microscopic mechanisms that control the macroscopic behavior of the materials exhibiting the PLC effect, a more advanced constitutive relation may be required.

8. Discussion

In this chapter, the overall results of experimental and numerical study are discussed with particular focus on Discontinuous Plastic Flow phenomenon. The discussion is organized in three consecutive steps.

First, the thermo-mechanical aspects are discussed from various points of view: since discovery of DPF phenomenon to the present work.

Second, an insight into the nature of microstructural evolution that occurs during DPF phenomenon is made.

Last, the concept of numerical model is discussed.

8.1. Thermo-Mechanical Coupling

The problem of plastic flow instability at extremely low temperatures [106] was investigated already in the 50-ties of last century and two competitive explanations were formulated: thermally or mechanically activated plastic flow discontinuities. Basiński [38] developed the thermal activation theory by attributing the load drops to the thermodynamic properties of materials at very low temperatures (thermodynamic instability). His adiabatic heating hypothesis was based on the assumption that any sufficiently fast dissipative process at very low temperatures (where the plastic work is converted to heat) leads to local increase of temperature and - as a result - to drastic decrease of flow stress. This effect is reflected by negative slope of flow stress against temperature.

On the other hand, the mechanical origin of discontinuous yielding was promoted by Obst and Nyilas [30]. In their attempt to explain this phenomenon the authors pointed out that the pile-ups of dislocations on the internal barriers in the lattice gave rise to stress concentrations of the order of magnitude of theoretical shear strength. The load drops observed in the stress-strain curves were attributed to a catastrophic process consisting in the spontaneous generation of

dislocations as soon as the internal barriers were broken. In view of this fact, the plastic flow instability was identified to be of mechanical origin, and all the associated thermodynamic phenomena were secondary.

Zaiser and Hähner [41], proposed another explanation of DPF. They explained discontinuous nature of plastic flow at extremely low temperatures by the strain rate softening instabilities. According to the authors, the mechanism of strain rate sensitivity consists of (a) positive instantaneous response of the flow stress to a sudden increase of strain rate and (b) subsequent relaxation of the flow stress to a quasi steady state asymptotic value. Such "oscillatory" mode of plastic flow is interpreted by the authors in terms of dynamic strain aging (DSA). The asymptotic behavior of flow stress in low temperature plasticity is governed by the temperature.

An important progress in explaining the nature of DPF has been obtained by Skoczeń et al. [8]. The measurements carried out with high precision, achieved by mounting internal load cell in direct proximity of the sample and by using the sampling frequency of 20 kHz, indicated the correct sequence of events within single serration: initial state (A), elastic loading (B), plastic flow (C), drop of stress (D), stress relaxation accompanied by simultaneous jump of temperature (E). It is worth pointing out, that the stress relaxation does not always take place. It is characteristic of such alloys like stainless steels. On the other hand, OFE Cu does not exhibit stress relaxation and drop of stress is instantaneously followed by elastic reloading. Nevertheless, in either case the increase of temperature occurs as a direct consequence of thermodynamic instability (specific heat tends to 0). Thus, DPF is a coupled thermo-mechanical phenomenon and needs both mechanical and thermodynamic insight.

Further tests and study of stainless steels, being subject of the present work, provided more detailed information on the DPF phenomenon in terms of different phases and correlation between stress, strain and temperature. What was previously described as a single step of stress drop, is now shown to be more complex, and therefore, split in two stages. Observed during low temperature tensile tests, the dynamic part of DPF appearance (phase D above) is presented as drop of stress (D') and immediately succeeding jump of strain (D"). This fast deformation is recognized as a direct cause of temperature rise, and as so, implemented into the numerical model. The temperature reaches its peak when

the dynamic process ends and then, during the relaxation phase, the heat is dissipated into the cooling bath.

8.2. Microstructural Evolution

For what concerns the mechanism of DPF [106], the interaction of dislocations with the barriers at extremely low temperatures can be qualified as analogical response with respect to the PLC effect. Indeed, both in the case of PLC and DPF dislocations meet obstacles and are temporarily arrested/locked. In the course of PLC, solutes diffuse around the dislocations and further strengthening of the obstacles is observed. In the case of DPF the obstacles remain stable because of weakly excited lattice at extremely low temperatures and evident lack of thermal energy. Eventually, these dislocations will in both cases overcome the obstacles reaching sufficient level of local resolved shear stress and will move to the next obstacle where they are again stopped. The difference between both mechanisms consists in the fact that in the case of PLC the obstacles are created by diffusion, whereas in the case of DPF the obstacles are "diffusionless". The idea that the breakdown of L-C locks is the principal mechanism of DPF is backed by a number of papers, including quite recent (when compared to the roots) works by Obst and Nyilas [30, 43].

Moreover, the same mechanism is strongly advocated in the topical review of most of the works dedicated to DPF, by Pustovalov [39]. Also, the experiments carried out in liquid helium indicate clearly that correct interpretation of the phenomenon is based on breakdown of barriers/locks (the Lomer-Cottrell locks are sessile and immobile) as soon as the local resolved shear stress reaches the level of the cohesive strength. It is followed by massive motion of dislocations, accompanied by fast temporary increase of strain and temperature as a result of thermodynamic instability. Small amount of heat liberated locally in the lattice contributes to stress relaxation at the end of the process. Moreover, during tensile test at low temperatures the avalanche-like barrier crossing by dislocation pile-ups is manifested by acoustic effects of "dry sounds" emitted by the specimen, which is recorded in the course of experiment.

It is worth pointing out, that the upper bound for strain rate is not an intrinsic feature of DPF. It is a consequence of thermodynamic equilibrium between the sample and the helium and as such does not constitute an integral part of the model. On the other hand, thermodynamic conditions of transition to smooth plastic flow can be easily established based on the present model.

8.3. Numerical Model

For the above raised reasons [106], it is difficult to explain serrated yielding as a self-organized process, emerging naturally from the nonlinear dynamics of the dislocation system, because of its physical complexity and the fact that it is a multi-stage, coupled, thermo-mechanical process. Thus, each serration has been finally decomposed into 4 stages, each of them of different nature: elastic, plastic, drop of stress and relaxation. These components are observed in vast majority of experiments, with the exception of relaxation that takes place in the materials where sufficient amount of thermal energy is stored during single serration (for instance stainless steels where the temperature may rise even by some 30-40 K). In the materials like copper the relaxation is rather negligible because of very small amount of heat stored during single serration (due to higher thermal conductivity, temperature rises usually by a fraction of K). One of the principal features of the model consists in the fact that a criterion of drop of stress based on physical parameters (surface density of barriers and shear stress at the head of dislocation pile-up) is postulated. The criterion is simple, linear and contains a minimum number of parameters to be identified (4). As long as identification of these parameters is feasible the model proves efficient. In a sense, it is an additional limit surface (beyond the yield surface) that is based on physical parameters and triggers the drop of stress.

The concept of the model forms an extension of the classical model known in the theory of plasticity as multi-surface representation. Such a formulation reflects well the physics of DPF. A thorough comparison of single serrations allows us to draw the conclusion that the drop of stress occurs usually at constant value of total strain. This fundamental assumption leads to the conclusion that the amount of slip is strictly related to the corresponding elastic unloading (Fig. 8.1) and results in a proportional drop of stress. Thus, it is the amount of

slip that is determined as a function of parameter B because of the fact, that with increasing B potential for larger slip occurs due to possible catastrophic failure of barriers/locks that spreads over a larger portion of the material. This assumption appears to be fully physical and corresponds to experiments. Finally, the drop of stress is computed from the condition of constant total strain, whereas the jump of strain follows, interpreted as dynamic dissipation caused by released dislocations.

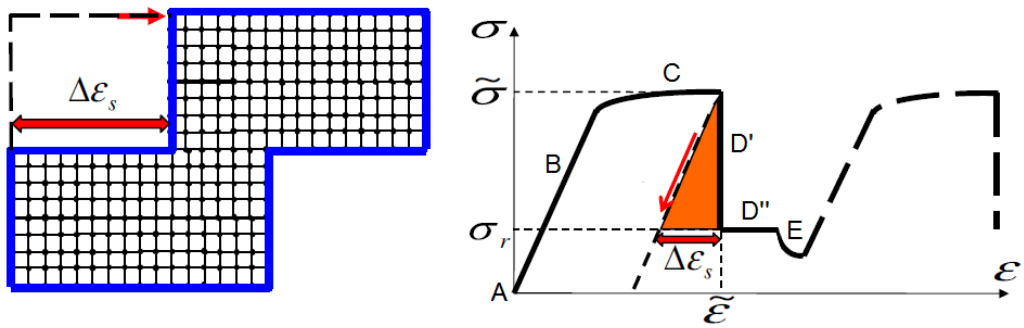

Figure 8.1.: The amount of slip ($\Delta\epsilon_s$) during the process of catastrophic failure of LC locks [106].

Even if the before mentioned classical papers related to DPF at extremely low temperatures refer mainly to the Lomer-Cottrell locks, the class of barriers observed in the lattice is broader. Therefore, creation of a generic model of DPF might be envisaged to account for other possible barriers for the motion of dislocations (for instance collinear reactions). The main problem consists, however, in gathering sufficient statistics for various types of barriers in order to find probabilistic representation of their occurrence in the lattice at extremely low temperatures. Each population of barriers should be described by the relevant probability density function, allowing to compute its predicted volume fraction under given condition (stress, inelastic strain, temperature etc.). Moreover, the kinetics of evolution of each type of barriers should be derived and experimentally confirmed. With this knowledge an attempt to build a unified generic model of discontinuous plastic flow for extremely low temperatures might be envisaged. On the other hand, as long as the present model reflects all the basic important features of DPF, and allows to reproduce the observed serrations, its applicability

is beyond question.

In summary, the model is physically based and reflects all the important features of DPF. Moreover, the model allows to reproduce the observed serrations, which is crucial for its application in the design of components for extremely low temperatures.

9. Conclusions

The constitutive model discussed in the present work addresses one of three fundamental phenomena that occur at very low temperatures in the materials characterized by the low stacking fault energy (LSFE): discontinuous plastic flow (DPF), often called serrated yielding. The other two dissipative phenomena: plastic strain induced fcc-bcc phase transformation (characteristic of metastable alloys) and evolution of ductile micro-damage (micro-voids and micro-cracks) may accompany DPF, contributing to fast evolution of microstructure and to irreversible degradation of lattice resulting in premature material failure.

In the present study cryogenic tensile tests performed on different materials were used. The discontinuous plastic flow phenomenon was analyzed, in order to develop a constitutive model of serrated yielding as a support for analysis of structural materials at low temperatures. Devices and structures, cooled be means of liquid helium, operate at the temperatures equal or lower than 4.2 K, which for the examined materials is below the transition threshold between screw and edge dislocations. It is considered a threshold for the appearance of DPF consisting in cyclic drop of load followed by deformation jumps and generation of heat. Temperature oscillations resulting from the thermodynamic instability in stainless steel can be of the order of $\Delta T = 40K$, which is exceptionally dangerous for superconducting cables.

In the present work three fundamental questions have been raised:

- Given the extensive metallurgical examinations performed, is the effect of mechanical and microstructural properties on the DPF phenomenon sufficiently recognized?

- Following materials tests at cryogenic temperatures, can all the experimental data be systematized to advance understanding of the mechanism of

DPF and the thermodynamic background related to heat transport at low temperatures?

- Concerning the DPF constitutive model and identification of parameters, is the provided solution representative and universal for stainless steels at cryogenic temperatures?

The answer to all these questions seems to be yes. These conclusions have rather fundamental meaning for thin-walled structures operating at extremely low temperatures like heat exchangers, corrugated expansion bellows or vacuum chambers. They mean, that the plastic flow in the proximity of absolute zero may lead to strong degradation of material cohesion due to its discontinuous nature. Frequently repeated macroscopic slips may lead to evolution of micro-damage fields and to initiation of macro-cracks, spoiling integrity of the structure. On the other hand, the oscillations of temperature may strongly affect conditions of heat exchange and - in the case of superconductors - may lead to premature resistive transition from superconducting to normal state.

Suitably calibrated numerical algorithm allows prediction of the behavior of the material subjected to deformation at low temperatures. The issues presented in the present study are currently of particular interest for accelerator centers, which operate structures at cryogenic temperatures such as superconducting magnets and liquid helium transfer lines [29]. The use of constitutive modeling in the design of structural elements, including physical processes at low temperatures, allows us to obtain structures with desired properties and reliability. There is a good prospect that in the future the cryogenic technologies will be widely used in the industry, and consequently, the correct mathematical models of materials used at extremely low temperatures will become essential tools for the engineers.

Bibliography

[1] H. K. Onnes, "Investigations into the properties of substances at low temperatures, which have led, amongst other things, to the preparation of liquid helium," *Nobel Lecture*, 1913.

[2] D. van Delft, "Heike Kamerlingh Onnes and the road to liquid helium," *IEEE/CSC & ESAS European Superconductivity News Forum (ESNF)*, vol. 16, 2011.

[3] D. van Delft and P. Kes, "The discovery of superconductivity," *Physics Today*, vol. 63, no. 9, pp. 38–43, 2010.

[4] D. van Delft and P. Kes, "The discovery of superconductivity," *Europhysics News*, vol. 42, no. 1, pp. 21–25, 2011.

[5] "http://lhc.web.cern.ch/." The Large Hadron Collider at the European Organization for Nuclear Research (LHC, CERN).

[6] "http://www.ipp.mpg.de/." Max Planck Institute for Plasma Physics.

[7] "http://www.iter.org/." The International Thermonuclear Experimental Reactor (ITER Organization).

[8] B. Skoczen, J. Bielski, S. Sgobba, and D. Marcinek, "Constitutive model of discontinuous plastic flow at cryogenic temperatures," *International Journal of Plasticity*, vol. 26, pp. 1659–1679, December 2010.

[9] A. Jha, *Cryogenic Technology and Applications.* No. 9780750678872 in ISBN, Elsevier Inc., 2006.

[10] B. D. Bondarenko, "Role played by O A Lavrent'ev in the formulation of the problem and the initiation of research into controlled nuclear fusion in the USSR," *Physics-Uspekhi*, vol. 44 (8), p. 844, 2001.

[11] "http://www.world-nuclear.org/." The World Nuclear Association.

[12] "http://www.ccfe.ac.uk/." The Culham Centre for Fusion Energy.

[13] "http://www.lhd.nifs.ac.jp/." The Large Helical Device at the National Institute for Fusion Science (LHD, NIFS).

[14] "https://lasers.llnl.gov/." The National Ignition Facility at the Lawrence Livermore National Laboratory.

[15] "First successful integrated experiment at National Ignition Facility announced," 2010.

[16] "http://www.efda.org/." The European Fusion Development Agreement.

[17] C. Barth, *High Temperature Superconductor Cable Concepts for Fusion Magnets*. PhD thesis, Karlsruhe Institute of Technology (KIT), 2013.

[18] S. Konishi, S. Nishio, K. Tobita, and D. design team, "DEMO plant design beyond ITER," *Fusion Engineering and Design*, vol. 63-64, pp. 11–17, 2002.

[19] Y. Wan, "Overview of the fusion roadmaps in the world," *27th Symposium on Fusion Technology (SOFT)*, 2012.

[20] F. Romanelli, P. Barabaschi, D. Borba, G. Federici, L. Horton, R. Neu, D. Stork, and H. Zohm, *Fusion Electricity - A roadmap to the realisation of fusion energy*. European Fusion Development Agreement (EFDA), 2012.

[21] F. I. Petrescu, *Cold Nuclear Fusion*. No. 978-3-8482-2852-2 in ISBN, Books on Demand GmbH, 2012.

[22] "http://www.ifmif.org/." The International Fusion Materials Irradiation Facility.

[23] S. Sgobba, J.-M. Dalin, P. Libeyre, D. J. Marcinek, and A. Nyilas, "Progress in production and qualification of stainless steel jacket material for the conductor of the ITER central solenoid," *IEEE Transactions on Applied Superconductivity*, vol. 22, p. 7800104, June 2012.

[24] N. Koizumi, H. Nakajima, K. Matsui, T. Hemmi, K. Takano, K. Okuno, M. Hasegawa, H. Kakui, and I. Senda, "Development of the ITER Toroidal Field coil winding pack in Japan," *IEEE Transactions on Applied Superconductivity*, vol. 20, no. 3, pp. 385–388, 2010.

[25] Y. Ilyin, D. Bessette, E. Zapretilina, C. Luongo, F. Simon, B. S. Lim, and N. Mitchell, "Performance analysis of the ITER Poloidal Field coil conductors," *IEEE Transactions on Applied Superconductivity*, vol. 20, no. 3, pp. 415–418, 2010.

[26] A. Foussat, P. Libeyre, N. Mitchell, Y. Gribov, C. T. J. Jong, D. Bessette, R. Gallix, P. Bauer, and A. Sahu, "Overview of the ITER Correction Coils design," *IEEE Transactions on Applied Superconductivity*, vol. 20, no. 3, pp. 402–406, 2010.

[27] D. J. Marcinek, "Experimental study of discontinuous plastic flow, phase transformation and micro-damage evolution in ductile materials at cryogenic temperatures," Master's thesis, Cracow University of Technology, 2009. CERN-THESIS-2009-192.

[28] C. Garion, *Material and structural mechanical modelling and reliability of thin-walled bellows at cryogenic temperatures. Application to LHC compensation system.* PhD thesis, University of Clermont-Ferrand, 2003.

[29] M. Sitko, *Constitutive modelling of functionally graded materials for low temperature structural applications.* PhD thesis, Cracow University of Technology, 2011.

[30] B. Obst and A. Nyilas, "Experimental evidence on the dislocation mechanism of serrated yielding in fcc metals and alloys at low temperatures," *Materials Science and Engineering*, vol. A137, pp. 141–150, 1991.

[31] A. Seeger, "Dislocations and mechanical properties of crystals," *Wiley, New York*, 1957.

[32] S. N. Komnik and V. V. Demirski, "Study of the instability boundaries of plastic flow in Cu + 14 at.% Al single crystals at low temperatures," *Crystal Research and Technology*, vol. 19, no. 6, pp. 863–872, 1984.

[33] R. P. Reed and R. P. Walsh, "Tensile strain rate effect in liquid helium," *Advances in Cryogenic Engineering Materials*, vol. 34, pp. 199–208, 1988.

[34] R. P. Reed and N. J. Simon, "Discontinuous yielding in austenitic steels at low temperatures," *International Cryogenic Material Conference, Boulder*, vol. 2, pp. 851–863, 1988.

[35] J. Bouquerel, K. Verbeken, and B. C. D. Cooman, "Microstructure-based model for the static mechanical behaviour of multiphase steels," *Acta Materialia*, vol. 54, pp. 1443–1456, 2006.

[36] R. Madec, B. Devincre, and L. P. Kubin, "From dislocation junctions to forest hardening," *Physical Review Letters*, vol. 89 (25), pp. 255508–1 – 255508–4, 2002.

[37] B. Skoczen, "Compensation systems for low temperature applications," *Springer, Berlin*, 2004.

[38] Z. S. Basinski, "The instability of plastic flow of metals at very low temperatures," *Proceeding of the Royal Society of London*, vol. A 240, pp. 229–242, 1957.

[39] V. Pustovalov, "Serrated deformation of metals and alloys at low temperatures (review)," *Low Temperature Physics*, vol. 34, pp. 683–723, 2008.

[40] R. B. Schwarz and J. W. Mitchell, "Dynamic dislocation phenomena in single crystals of Cu-10.5-at.%-Al alloys at 4.2 k," *Physical Reviews*, vol. B 9, pp. 3292–3299, 1974.

[41] P. Hahner and M. Zaiser, "From mesoscopic heterogeneity of slip to macroscopic fluctuations of stress and strain," *Acta Materialia*, vol. 45 (3), pp. 1067–1075, 1997.

[42] M. Zaiser and P. Hahner, "Oscillatory modes of plastic deformation: theoretical concepts," *Physica Status Solidi*, vol. B 199, pp. 267–330, 1997.

[43] B. Obst and A. Nyilas, "Time-resolved flow stress behavior of structural materials at low temperatures," *Advances in Cryogenic Engineering (Materials), Plenum Press, New York*, vol. 44, pp. 331–338, 1998.

[44] E. T. Wessel *Transactions of ASM*, vol. 49, p. 149, 1956.

[45] E. D. Tabachnikova, A. M. Dolgin, V. Z. Bengus, and Y. V. Yefimov, "Plastic deformation of niobium monocrystals at low temperatures," *Fizika Metallov i Metallovedenie*, vol. 58, pp. 573–579, September 1984.

[46] S.-H. Cho, Y.-C. Yoo, and J. J. Jonas, "Static and dynamic strain aging in 304 austenitic stainless steel at elevated temperatures," *Journal of Materials Science*, vol. 19, p. 2019 Ű 2022, 2000.

[47] J. Robinson and M. Shaw, "Microstructural and mechanical influences on dynamic strain aging phenomena," *International Materials Reviews*, vol. 39, no. 3, pp. 113–122, 1994.

[48] S. Lou and D. Northwood, "Elevated temperature properties and dynamic strain aging in a construction grade steel," *Materials Science Forum*, vol. 17, no. 2, pp. 153–158, 1993.

[49] A. Benallal, T. Borvik, A. Clausen, and O. Hopperstad, "Dynamic strain aging, negative strain-rate sensitivity and related instabilities," *Technische Mechanik*, vol. 23 (2-4), p. 160Ű 166, 2003.

[50] A. Benallal, T. Berstad, T. Borvik, A. H. Clausen, and O. S. Hopperstad, "Dynamic strain aging and related instabilities: experimental, theoretical and numerical aspects," *European Journal of Mechanics - A/Solids*, vol. 25 (3), pp. 397–424, 2006.

[51] R. Reed and R. Mikesell, *Low temperature mechanical properties of copper and selected copper alloys: a compilation from the literature.* NBS monograph, U.S. Dept. of Commerce, National Bureau of Standards; for sale by the Supt. of Docs., U.S. Govt. Print. Off., 1967.

[52] R. L. Tobler, A. Nishimura, and J. Yamamoto, "Design-relevant mechanical properties of 316-type steels for superconducting magnets," *Cryogenics*, vol. 37, pp. 533–550, 1997.

[53] S. Sgobba, "Materials of high vacuum technology, an overview," *CERN Accelerator School "Vacuum in Accelerators"*, 2006.

[54] H. Nakajima, K. Yoshida, and S. Shimamoto, "Development of the fusion of new cryogenic steels experimental reactor for the superconducting magnets," *Iron and Steel Institute of Japan*, vol. 30, no. 8, pp. 567–578, 1990.

[55] H. Nakajima, K. Hamada, K. Takano, K. Okuno, and N. Fujitsuna, "Development of low carbon and boron added 22MnŰ13CrŰ9NiŰ1MoŰ0.24N steel (JK2LB) for jacket which undergoes Nb3Sn heat treatment," *IEEE Transactions on Applied Superconductivity*, vol. 14, no. 2, pp. 1145–1148, 2004.

[56] J. Lu, R. Walsh, and K. Han, "Low temperature physical properties of a high mn austenitic steel JK2LB," *Cryogenics*, vol. 49, pp. 133–137, 2009.

[57] P. Libeyre, N. Mitchell, D. Bessette, Y. Gribov, C. Jong, and C. Lyraud, "Detailed design of the ITER central solenoid," *Fusion Engineering and Design*, vol. 84, pp. 1188–1191, 2009.

[58] P. Libeyre, D. Bessette, A. Devred, C. Jong, N. Mitchell, and S. Sgobba, "Conductor jacket development to meet the mechanical requirements of the ITER central solenoid coils," *Fusion Engineering and Design*, to be published.

[59] K. Hamada, H. Nakajima, K. Kawano, K. Takano, F. Tsutsumi, K. Okuno, T. Suzuki, , and N. Fujitsuna, "Optimization of JK2LB chemical composition for ITER Central Solenoid conduit material," *Cryogenics*, vol. 47, pp. 174–182, 2007.

[60] "Procurement specification for CS conductor conduit development length using JK2LB or 316LN(LC) Technical specification ITER-D-2LTKVM."

[61] S. Sgobba, P. Libeyre, D. J. Marcinek, and A. Nyilas, "A comparative assessment of metallurgical and mechanical properties of two austenitic stainless steels for the conductor jacket of the ITER central solenoid," *Fusion Engineering and Design*, vol. In Press, p. Corrected Proof, Available online: May 2013.

[62] A. Devred, I. Backbier, D. Bessette, G. Bevillard, M. Gardner, C. Jong, F. Lillaz, N. Mitchell, G. Romano, and A. Vostner, "Challenges and status

of ITER conductor production," *Superconductor Science and Technology*, vol. 27, no. 4, p. 044001, 2014.

[63] V. Samain, "Characterization of structural materials and welds for high field superconductive magnets for fusion," Master's thesis, HELMo Gramme, 2012.

[64] F. C. Hull, "Delta ferrite and martensite formation in stainless steels," *Welding Journal*, vol. 52, pp. 193s–203s, May 1973.

[65] "http://www.bgh.de/." BGH Edelstahlwerke GmbH.

[66] "Four de traitements sous vide I 200 °C FV 004," tech. rep., Centre de Physique Électronique et Corpusculaire, 1965.

[67] ASTM-E45, "Standard test methods for determining the inclusion content of steel," 2011.

[68] ASTM-E407, "Standard practice for microetching metals and alloys," 2007.

[69] ASTM-E112, "Standard test methods for determining average grain size," 2012.

[70] ASTM-A262, "Standard practices for detecting susceptibility to intergranular attack in austenitic stainless steels," 2002.

[71] ASTM-E8M, "Standard test methods for tension testing of metallic materials," 2011.

[72] ASTM-E1450, "Standard test method for tension testing of structural alloys in liquid helium," 2009.

[73] S. Bonhomme, "Modernisation des essais de traction a basse temperature et mesure de l'effet de serration," report de stage, CERN, 2003.

[74] N. Portier, "Essais mecaniques a basse temperature: optimisation de la chaine d'acquisition pour permettre un echantillonnage a tres haute frequence," report de stage, CERN, 2004.

[75] S. Moulis, "Optimisation de la ligne d'essais mecaniques a temperature cryogenique (4.2 k) par introduction d'un capteur a jauges de contrainte," report de stage, CERN, 2005.

[76] L. Gharios, "Caracterisation de materiaux pour la physique des hautes energies," report de stage, CERN, 2006.

[77] A.-L. Grout, "Test de traction a 4.2 k," report de stage, CERN, 2007.

[78] "http://www.thames-side.com/." Thames Side Sensors Limited.

[79] "http://www.nyilas-arman.de/." Dr Arman Nyilas: Freelance Engineering Consultant CEME, Cryogenic Engineering & Materials Expertise Mechanical & Physical data, Displacement Instrumentation Data Acquisition & Evaluation.

[80] J. Tabin, "Cryogenic stand for investigations of material properties in ultra low temperature. quality optimization of measurement chain." Cryostat design meeting at CERN Engineering Department, January 2012.

[81] "http://www.sensorex.fr/meggitt/." Meggitt (Sensorex).

[82] "http://www.lakeshore.com/." Lake Shore Cryotronics Inc.

[83] HBM Messtechnik, *QuantumX - Operating Manual*.

[84] A. Nyilas, "Fracture toughness & fatigue crack growth rate report on compacted, strained, aged, and non-strained JK2LB pipes at 7 k," tech. rep., Cryogenic Engineering & Materials Expertise (CEME), KIT, Germany, 2012.

[85] "http://www.kit.edu/." Karlsruher Institut für Technologie.

[86] ASTM-E1820, "Standard test method for measurement of fracture toughness," 2013.

[87] A. Nishimura, J. Yamamoto, and A. Nyilas, "Fatigue crack growth of SUS 316 and weld joint with natural crack at 7 k," *Advances in Cryogenic Engineering (Materials)*, vol. 44A, pp. 81–88, 1998.

[88] P. C. Paris, M. P. Gomez, and W. E. Anderson, "A rational analytic theory of fatigue," *The Trend in Engineering*, vol. 13, pp. 9–14, 1961.

[89] L. Dong, R. Haynes, and S. N. Atluri, "On improving the celebrated parisŠ power law for fatigue, by using moving least squares," *Computers, Materials & Continua*, vol. 45, no. 1, pp. 1–15, 2015.

[90] R. R. Ambriz and D. Jaramillo, "Mechanical behavior of precipitation hardened aluminum alloys welds," *Light Metal Alloys Applications*, pp. 35–59, 2014. ISBN: 978-953-51-1588-5.

[91] F. de Jaegere, "Metallurgical qualification of a 316LN stainless steel extruded shape, shape IQE 46 2.5 % untreated (_NT) produced by CEFIVAL /FR, compacted by CRIOTEC /IT and tensile stretched 2.5 % by CEFIVAL," tech. rep., CERN EDMS No 1103517, 2010.

[92] F. de Jaegere, "Metallurgical qualification of a 316LN stainless steel extruded shape, shape IQE 46 2.5 % untreated (_NT) produced by CEFIVAL /FR, compacted by CRIOTEC /IT and tensile stretched 2.5 % by CEFIVAL and aged at CERN," tech. rep., CERN EDMS No 1111408, 2011.

[93] D. J. Marcinek, "MQ on ITER TF, fushun/ASIPP 316LN," tech. rep., CERN EDMS No 1140946, 2011.

[94] D. J. Marcinek, "MQ on ITER TF, fushun/ASIPP 316LN, (better-controlled solution anneal)," tech. rep., CERN EDMS No 1149222, 2011.

[95] D. J. Marcinek, "MQ of a 316LN sample plates, ITER CC base material from Tisco," tech. rep., CERN EDMS No 1175462, 2011.

[96] D. J. Marcinek, "MQ and TT of ITER CS jacket, cefival JK2LB N7 tube," tech. rep., CERN EDMS No 1137108, 2011.

[97] D. J. Marcinek, "MQ and TT of ITER CS jacket, cefival JK2LB N2 tube," tech. rep., CERN EDMS No 1141707, 2011.

[98] D. J. Marcinek, "MQ and TT of ITER CS jacket, cefival JK2LB N5 tube -2-," tech. rep., CERN EDMS No 1156113, 2011.

[99] D. J. Marcinek, "MQ of ITER CS jacket, cefival JK2LB tube N1," tech. rep., CERN EDMS No 1157698, 2011.

[100] D. J. Marcinek, "MQ of ITER CS jacket, cefival JK2LB tube N1 aged," tech. rep., CERN EDMS No 1170536, 2011.

[101] N. Mitchell, D. Bessette, A. Devred, and K. Hamada, "Procurement specification for CS conductor conduit development length using JK2LB or 316LN(LC)," technical specifications ITER_D_2LTKVM, ITER, 2009.

[102] D. J. Marcinek, "TT of ITER CS conductor jacket, cefival JK2LB tube N1," tech. rep., CERN EDMS No 1167419, 2011.

[103] D. J. Marcinek, "TT of ITER CS conductor jacket, samples cefival IQE 46 2.5%," tech. rep., CERN EDMS No 1136458, 2011.

[104] D. J. Marcinek, "TT of ITER CS conductor jacket, samples 316LN ASIPP/china," tech. rep., CERN EDMS No 1137181, 2011.

[105] D. J. Marcinek, "TT of ITER CC welds and BM 316LN; delivered from ASIPP/CN," tech. rep., CERN EDMS No 1189434, 2012.

[106] B. Skoczen, J. Bielski, and J. Tabin, "Multiaxial constitutive model of discontinuous plastic flow at cryogenic temperatures," *International Journal of Plasticity*, vol. 55, pp. 198–218, April 2014.

[107] T. Shintani and Y. Murata, "Evaluation of the dislocation density and dislocation character in cold rolled type 304 steel determined by profile analysis of X-ray diffraction," *Acta Materialia*, vol. 59, pp. 4314–4322, 2011.

[108] E. D. Marquardt, J. P. Le, and R. Radebaugh, "Cryogenic material properties database," *11th International Cryocooler Conference*, June 2000.

[109] A. Benallal, T. Berstad, T. Borvik, O. S. Hopperstad, I. Koutiri, and R. N. de Codesa, "An experimental and numerical investigation of the behaviour of AA5083 aluminium alloy in presence of the Portevin-Le Chatelier effect," *International Journal of Plasticity*, vol. 24, pp. 1916–1945, October 2008.

List of Figures

List of Tables

A. Appendix

A.1. Maple: Execution Group

> *restart*;

Parameters:

Execution group:

> # *A. ---------- Initial state ----------*

$k := 0;$ $T_k := T_0;$
$\varepsilon_k := 0;$ $\sigma_k := 0;$
$B_k := 0;$ $\rho_k := \rho_0;$
$\varepsilon_p := 0;$ $\varepsilon_{pLC} := \varepsilon_{pLC0};$
$(\Delta\varepsilon_{pLC})_k := \Delta\varepsilon_{pLC0};$ $\tau_k := \tau_{\min};$

> **while** $\varepsilon_k < \varepsilon_{\max}$ **do**

B. ---------- Elastic deformation ----------

for k **from** k **by** 1 **to** $step_{\max}$ **while** $\sigma_k < \sigma_p$ **do** # *yield condition*

$\varepsilon_{k+1} := \varepsilon_k + \Delta\varepsilon_0;$ $\sigma_{k+1} := \sigma_k + E_0 \cdot \Delta\varepsilon_0;$

$T_{k+1} := T_0;$

$(\Delta\varepsilon_{pLC})_{k+1} := (\Delta\varepsilon_{pLC})_k;$
$B_{k+1} := B_k;$
$\rho_{k+1} := \rho_k;$
$\tau_{k+1} := \tau_k;$

$A_{k+1,1} := \varepsilon_{k+1};$ $A_{k+1,2} := \sigma_{k+1};$ $A_{k+1,3} := T_{k+1};$
$A_{k+1,4} := B_{k+1};$ $A_{k+1,5} := \rho_{k+1};$ $A_{k+1,6} := \tau_{k+1};$

end do:

C. ---------- Plastic deformation ----------

$\tau_e := \tau_{\min};$

for k **from** k **by** 1 **to** $step_{\max}$ **while** # *serration criterion*

$$\left(1 - \frac{B_{\min}}{B_{cr}}\right) \cdot \left(\frac{\tau_e}{\tau_{cr}}\right) + \left(1 - \frac{\tau_{\min}}{\tau_{cr}}\right) \cdot \left(\frac{B_k}{B_{cr}}\right) - \left(1 - \frac{B_{\min}}{B_{cr}}\right) - \left(1 - \frac{\tau_{\min}}{\tau_{cr}}\right) \cdot \left(\frac{B_{\min}}{B_{cr}}\right) < 0$$

do

$\varepsilon_{k+1} := \varepsilon_k + \Delta\varepsilon_0;$ $\sigma_{k+1} := \sigma_k + E_p \cdot \Delta\varepsilon_0;$ *# linear hardening*

$\Delta\varepsilon_p := \Delta\varepsilon_0 \cdot \left(1 - \frac{E_p}{E_0}\right);$ $\varepsilon_p := \varepsilon_p + \Delta\varepsilon_p;$

$T_{k+1} := T_k;$

$\left(\Delta\varepsilon_{pLC}\right)_{k+1} := \left(\Delta\varepsilon_{pLC}\right)_k;$

if $\varepsilon_p > \varepsilon_{pLC}$ **then**

 # LC locks criterion and evolution

$F_{plusLC} := k4 \cdot \sqrt{\rho_k};$

$B_{k+1} := B_k + F_{plusLC} \cdot \left(\varepsilon_p - \varepsilon_{pLC}\right);$

$\Delta\rho := \Delta\varepsilon_0 \cdot M \cdot \left(\frac{1}{d \cdot b} + k1 \cdot \frac{\sqrt{\rho_k}}{b} - k3 \cdot \rho_k\right);$ *# dislocation density evolution*

$\rho_{k+1} := \rho_k + \Delta\rho;$

$\tau_{k+1} := \tau_f + \alpha \cdot \mu \cdot b \cdot \sqrt{\rho_{k+1}};$ *# shear stress in the lattice*

$\lambda_s := \frac{1}{\frac{1}{d} + k1 \cdot \sqrt{\rho_{k+1}} + k2 \cdot \sqrt{B_{k+1}}};$ *# mean slip distance*

$\tau_e := \frac{evalf(\pi) \cdot (1 - \nu)}{\mu \cdot b} \cdot \lambda_s \cdot \tau_{k+1}^2;$ *# shear stress at the head of dislocation pile-up*

else $B_{k+1} := B_k;$ $\rho_{k+1} := \rho_k;$ $\tau_{k+1} := \tau_k;$

end if;

if $B_{k+1} > B_{cr}$ **then** $B_{k+1} := B_{cr}$ **end if**;

$A_{k+1,1} := \varepsilon_{k+1};$ $A_{k+1,2} := \sigma_{k+1};$ $A_{k+1,3} := T_{k+1};$

$A_{k+1,4} := B_{k+1};$ $A_{k+1,5} := \rho_{k+1};$ $A_{k+1,6} := \tau_{k+1};$

end do:

 # D. ---------- Serration - drop of stress ----------

$F_{minusLC} := F_{plusLC} \cdot 800;$

$\Delta\varepsilon_p := \frac{B_k}{F_{minusLC}};$ *# the LC locks vanish*

$B_{k+1} := 0;$ $\rho_{k+1} := \rho_k;$

$\varepsilon_p := \varepsilon_p + \Delta\varepsilon_p;$ $\varepsilon_{pLC} := \left(\Delta\varepsilon_{pLC}\right)_k + \varepsilon_p;$

$\Delta\sigma := E_0 \cdot \Delta\varepsilon_p;$

$\varepsilon_{k+1} := \varepsilon_k;$ $\sigma_{k+1} := \sigma_k - \Delta\sigma;$ *# drop of stress at constant strain value*

$T_{k+1} := T_k;$

$\tau_{k+1} := \tau_k;$

$A_{k+1,1} := \varepsilon_{k+1};$ $A_{k+1,2} := \sigma_{k+1};$ $A_{k+1,3} := T_{k+1};$

$A_{k+1,4} := \mathrm{B}_{k+1};$ $A_{k+1,5} := \rho_{k+1};$ $A_{k+1,6} := \tau_{k+1};$

$\left(\Delta\varepsilon_{pLC}\right)_{k+1} := \left(\Delta\varepsilon_{pLC}\right)_k;$

$\varepsilon_{serr} := \varepsilon_k;$ $\sigma_{serr} := \sigma_k;$

$\sigma_\infty := \left(0.91 - 0.2 \cdot \varepsilon_{serr}\right) \cdot \sigma_{k+1};$ *# (accepted) asymptotic level,*

 # for JK2LB deacresed in function of ε

$k := k + 1;$

 # D'. ---------- Serration - jump of strain ----------

$Tk := T_k;$

$$T_{k+1} := T_k + \eta \cdot \frac{\sigma_{k-1} + \sigma_k}{2} \cdot \frac{\Delta\varepsilon_p}{\rho_m \cdot evalf\left(cv_{pro}(Tk)\right)};$$

$$\Delta\varepsilon_s := \frac{-\Delta\sigma}{\mathrm{H}_s};$$

 # material softening

$\varepsilon_{k+1} := \varepsilon_k + \Delta\varepsilon_s;$ $\sigma_{k+1} := \sigma_k;$

$\rho_{k+1} := \rho_0;$

$\tau_{k+1} := \tau_k;$

$B_{k+1} := B_k;$

$A_{k+1,1} := \varepsilon_{k+1};$ $A_{k+1,2} := \sigma_{k+1};$ $A_{k+1,3} := T_{k+1};$

$A_{k+1,4} := \mathrm{B}_{k+1};$ $A_{k+1,5} := \rho_{k+1};$ $A_{k+1,6} := \tau_{k+1};$

$\left(\Delta\varepsilon_{pLC}\right)_{k+1} := \left(\Delta\varepsilon_{pLC}\right)_k;$

$k := k + 1;$

 # E. ---------- Relaxation ----------

for k **from** k **by** 1 **to** $step_{\max}$ **while** $\sigma_k > 1.05 \cdot \sigma_\infty$ **do** *# reaching the asymptotic level*

D

$$\Delta\sigma := \frac{\left(\sigma_\infty - \sigma_k - \Delta\sigma\right)}{t_\Phi};$$ # evolution of stress decrement

$\varepsilon_{k+1} := \varepsilon_k + \Delta\varepsilon_0;$ $\sigma_{k+1} := \sigma_k + \Delta\sigma;$

if $T_k > T_0$ **then**

$Tk := T_k;$

$$T_{k+1} := T_k - \frac{xvc \cdot \Delta\varepsilon_0 \cdot evalf\left(\lambda_{pro}(Tk)\right)}{\rho_m \cdot evalf\left(cv_{pro}(Tk)\right)} \cdot \left(T_k - T_0\right)$$

else $T_{k+1} := T_0$

end if;

if $T_{k+1} < T_0$ **then** $T_{k+1} := T_0$ **end if**;

$B_{k+1} := B_k;$

$\rho_{k+1} := \rho_k;$

if $\tau_k > \tau_{\min}$ **then**

$$\Delta\tau := \frac{\left(\tau_k - \tau_{\min}\right)}{0.2 \cdot t_\Phi};$$

$\tau_{k+1} := \tau_k - \Delta\tau;$

else $\tau_{k+1} := \tau_{\min}$

end if;

$A_{k+1,1} := \varepsilon_{k+1};$ $A_{k+1,2} := \sigma_{k+1};$ $A_{k+1,3} := T_{k+1};$

$A_{k+1,4} := B_{k+1};$ $A_{k+1,5} := \rho_{k+1};$ $A_{k+1,6} := \tau_{k+1};$

$$\left(\Delta\varepsilon_{pLC}\right)_{k+1} := 0.95 \cdot \left(\Delta\varepsilon_{pLC}\right)_k;$$

end do:

$$\sigma_p := \left(\frac{E_p \cdot E_0}{\left(E_0 - E_p\right)} \cdot \left(\varepsilon_k - \varepsilon_{serr}\right) - \sigma_k \cdot \frac{E_p}{E_0 - E_p} + \sigma_{serr} \cdot \frac{E_0}{E_0 - E_p}\right);$$

update the yield point (back on the linear hardening line)

end do;

▶ Results / graphs

A.2. Maple: Parameters of 316LN

> *restart*;

Parameters:

> $\rho_0 := 3.0 \cdot 10^{13}$; # *initial density of dislocations: m^{-2}*

$\sigma_p := 12.8 \cdot 10^8$; # *initial yield point stress value: Pa*

$E_0 := 2.0 \cdot 10^{11}$; # *elasticity modulus: Pa*

$E_p := 6.4 \cdot 10^8$; # *modulus of linear isotropic plastic hardening: Pa*

$H_s := -5.0 \cdot 10^9$; # *modulus of linear isotropic plastic softening: Pa*

$\varepsilon_{pLC0} := \frac{8 \cdot \sigma_p}{E_0}$; # *initial plastic strain threshold of LC locks evolution*

$\Delta\varepsilon_{pLC0} := 0.01 \cdot \varepsilon_{pLC0}$; # *initial variable increment of the threshold*

$\varepsilon_{\max} := 0.23$;

$step_{\max} := 9200$;

$\Delta\varepsilon_0 := \frac{\varepsilon_{\max}}{step_{\max}}$;

$M := 3.0$; # *Taylor's constant*

$d := 5 \cdot 10^{-5}$; # *mean grain size: m*

$b := 2.58 \cdot 10^{-10}$; # *length of the Burgers vector: m*

$k1 := 0.031$;

$k2 := 0.02$;

$k3 := 0.01$;

$k4 := 2.5 \cdot 10^7$; # m^{-1}

$\tau_f := \frac{\sigma_p}{M}$; # *shear stress due to internal friction*

$\alpha := 0.4$; # *coefficient of dislocations stress interaction*

$\nu := 0.3$; # *Poisson's ratio*

$\mu := \frac{E_0}{2 \cdot (1 + \nu)}$; # *shear modulus (Kirchhoff)*

$B_{cr} := 8 \cdot 10^{13}$; # m^{-2}

$B_{\min} := 0$;

$\tau_{cr} := 450 \cdot \tau_f$;

$\tau_{\min} := \tau_f + \mu \cdot \alpha \cdot b \cdot \sqrt{\rho_0}$; # *shear stress in the lattice*

$t_\Phi := 250$; # *dimentionless time constant in relaxation relations*

> $T_0 := 4.2$; # *test temperature: K*

$\epsilon := 2 \cdot 10^{-3}$; # *strain speed*

$a := 0.003$; # *sample thickness: m*

F

$xvc := \frac{4.0}{a^2 \cdot \epsilon};$

$\rho_m := 7860;$ # density of the tested material: $\frac{kg}{m^3}$

$\eta := 0.9;$ # efficiency: 1.0 = 100 %

$cv_{pro} :=$ **proc**(Tk)
local x;
$x := \frac{\ln(Tk)}{ln10};$
$x := ((((((-2.239153 \cdot x + 24.7593) \cdot x - 112.9212) \cdot x + 274.0328) \cdot x - 381.0098) \cdot x + 303.6470) \cdot x - 127.5528) \cdot x + 22.0061;$
$\exp(x \cdot ln10)$
end proc;

$\lambda_{pro} :=$ **proc**(Tk)
local x;
$x := \frac{\ln(Tk)}{ln10};$
$x := (((((((-0.0199 \cdot x + 0.1650) \cdot x - 0.4658) \cdot x + 0.4256) \cdot x + 0.2334) \cdot x - 0.6260) \cdot x + 0.2543) \cdot x + 1.3982) \cdot x - 1.4087;$
$\exp(x \cdot ln10)$
end proc;

> $A := Array(1..step_{max}, 1..6);$

▶ Execution group:

▶ Results / graphs

A.3. Maple: Parameters of JK2LB

> *restart*;

Parameters:

> $\rho_0 := 3.0 \cdot 10^{13}$; # *initial density of dislocations: m*$^{-2}$

$\sigma_p := 15.6 \cdot 10^8$; # *initial yield point stress value: Pa*

$E_0 := 2.0 \cdot 10^{11}$; # *elasticity modulus: Pa*

$E_p := 2.4 \cdot 10^8$; # *modulus of linear isotropic plastic hardening: Pa*

$H_s := -10 \cdot 10^9$; # *modulus of linear isotropic plastic softening: Pa*

$\varepsilon_{pLC0} := \frac{6 \cdot \sigma_p}{E_0}$; # *initial plastic strain threshold of LC locks evolution*

$\Delta\varepsilon_{pLC0} := 0.01 \cdot \varepsilon_{pLC0}$; # *initial variable increment of the threshold*

$\varepsilon_{\max} := 0.25$;

$step_{\max} := 10000$;

$\Delta\varepsilon_0 := \frac{\varepsilon_{\max}}{step_{\max}}$;

$M := 3.0$; # *Taylor's constant*

$d := 6 \cdot 10^{-5}$; # *mean grain size: m*

$b := 2.58 \cdot 10^{-10}$; # *length of the Burgers vector: m*

$k1 := 0.031$;

$k2 := 0.02$;

$k3 := 0.01$;

$k4 := 2.5 \cdot 10^7$; # m^{-1}

$\tau_f := \frac{\sigma_p}{M}$; # *shear stress due to internal friction*

$\alpha := 0.4$; # *coefficient of dislocations stress interaction*

$\nu := 0.3$; # *Poisson's ratio*

$\mu := \frac{E_0}{2 \cdot (1 + \nu)}$; # *shear modulus (Kirchhoff)*

$B_{cr} := 11 \cdot 10^{13}$; # m^{-2}

$B_{\min} := 0$;

$\tau_{cr} := 750 \cdot \tau_f$;

$\tau_{\min} := \tau_f + \mu \cdot \alpha \cdot b \cdot \sqrt{\rho_0}$; # *shear stress in the lattice*

$t_\Phi := 350$; # *dimentionless time constant in relaxation relations*

> $T_0 := 4.2$; # *test temperature: K*

$\epsilon := 2 \cdot 10^{-3}$; # *strain speed*

$a := 0.003$; # *sample thickness: m*

H

$xvc := \frac{4.0}{a^2 \cdot \epsilon};$

$\rho_m := 7860;$ # density of the tested material: $\frac{kg}{m^3}$

$\eta := 0.9;$ # efficiency: 1.0 = 100 %

$cv_{pro} :=$ **proc**(Tk)
local x;
$x := \frac{\ln(Tk)}{ln10};$
$x := ((((((-2.239153 \cdot x + 24.7593) \cdot x - 112.9212) \cdot x + 274.0328) \cdot x - 381.0098) \cdot x + 303.6470) \cdot x - 127.5528) \cdot x + 22.0061;$
$\exp(x \cdot ln10)$
end proc;

$\lambda_{pro} :=$ **proc**(Tk)
local x;
$x := \frac{\ln(Tk)}{ln10};$
$x := (((((((-0.0199 \cdot x + 0.1650) \cdot x - 0.4658) \cdot x + 0.4256) \cdot x + 0.2334) \cdot x - 0.6260) \cdot x + 0.2543) \cdot x + 1.3982) \cdot x - 1.4087;$
$\exp(x \cdot ln10)$
end proc;

> $A := Array(1..step_{\max}, 1..6);$

▶ Execution group:

▶ Results / graphs